APPLICATION OF ORDINAL-ARRAY-BASED INDICATORS TO STRANGE NONCHAOTIC ATTRACTORS

By

Jean Sire Armand Eyebe Fouda

SUBMITTED IN PARTIAL FULFILLMENT OF THE

REQUIREMENTS FOR THE DEGREE OF

HABILITATION

AT

UNIVERSITY OF KASSEL

HEINRICH-PLETT-STR. 40, 34132 KASSEL

JUNE 2017

Minyene Pauline Christelle.

Table of Contents

List of abbreviations

LE: Lyapunov exponent

LLE: Largest Lyapunov exponent

MLE: maximal Lyapunov exponent

3ST: Three-state test

PE: Permutation entropy

CPE: Conditional permutation entropy of ordinal patterns

PLSE: Permutation largest slope entropy

OA: Ordinal array

OAE: Ordinal array entropy

OAC: Ordinal array complexity

SNA: Strange nonchaotic attractors

KS: Kolmogorov-Sinai

ME: Matching energy

H-H: Heagy-Hammel

DDQ: Differential dynamical quantization

NLE: Nonlinear element

CSV: Comma separated values

Abstract

Time series are useful for modeling systems behavior, for predicting some events (catastrophes, epidemics, weather, ...) or for classification purposes (pattern recognition, pattern analysis). Among the existing data analysis algorithms, ordinal pattern based algorithms have been shown effective when dealing with simulation data. However, when applied to quasi-periodically forced systems, they fail to detect SNA and tori as regular dynamics. In this work we address this concern by defining ordinal array (OA) based indicators, namely the OA complexity (OAC) and three OA asymptotic growth indices: the periodicity, the quasi-periodicity and the non-regularity index. OA growth indices allow to clearly distinguish between periodic and quasi-periodic dynamics, which is not possible with the existing ordinal pattern-based entropy and complexity measures. They clearly output integer values for periodic dynamics and non-integer values for SNA and quasi-periodic dynamics. SNA and quasi-periodic dynamics are distinguished from weakly chaotic dynamics by the sign of the non-regularity index: it is positive for chaotic data and negative for regular dynamics. A further test based on the dependence of the OA growth indices on the time series length allows us to distinguish between tori and SNA. Moreover, by defining the upper limits of the OA growth indices for purely random data, a classification between deterministic and stochastic data is achieved. The non-regularity index may also be used as a complexity measure for non-regular dynamics by considering large time series length, but the OAC still provides a better estimate of the complexity for moderate data length. So, OA growth indices are useful for determining the nature of the data series (periodic, quasi-periodic, chaotic or stochastic), while the OAC allows us to estimate the corresponding complexity. The four indicators thus defined constitute a complete tool for nonlinear data analysis applicable to any type of time series.

Acknowledgements

I sincerely thank the Alexander von Humboldt foundation which was supporting this work.

I would like to thank Prof. Dr. Wolfram Koepf, my supervisor, for his many suggestions and constant support during this research. I am also thankful to all my colleagues from Cameroon and Germany, India and Romania for their collaboration during the early years of chaos and confusion in this research area.

Many thanks to Dr. Bertrand Bodo, my official substituting colleague in the University of Yaoundé I during my research stay in Germany.

Thank you to Professors Mama Foupouagnigni and Blaise Romeo Nana Nbenjo for their assistance.

I thank Dr. John Abbott for the careful proofreading of this manuscript.

I would like to thank also my home University (the University of Yaoundé I) colleagues and the administration staff who gave me the opportunity to come in Germany for achieving this work.

Of course, I am grateful to my wife, Pauline Christelle Minyene, for her patience and *love*, and my son Jean-Daniel Edou who accepted to stay far away from his parents during this long period. Without them this work would have never come into existence.

I am also grateful to my family for all his support.

Finally, I wish to thank the following: Daniel Tcheutia; Raymond Toka, Etienne Nana Chiadjeu; Merlin Mouafo; Emmanuel Touko; Theophile Ofodo and all other brothers and friends who helped me solving any other life problems when I was concerned by this work.

Kassel, Germany J. S. Armand EYEBE FOUDA

June 30, 2017

Introduction

Natural systems obey physical laws which can be better understood by means of mathematical modeling. As recent progress in laboratory experiments and data analysis methods have revealed fundamental properties of nonlinear dynamical systems [16, 29], the challenge nowadays is to exploit ideas from chaos theory in real-life phenomena wherever more structures are observed from data than with traditional methods [44]. For this purpose, many complex phenomena are being modeled using the concept of nonlinear dynamical systems or simply chaos theory.

System modeling depends prior on observations made from the real-world system and is useful for prediction, classification, fault detection, ... Time series therefore constitute the starting point for system modeling or analysis. However, if so far modeling has been shown efficient, it is nevertheless important to note that it is based on approximations that sometimes can diverge from reality. Indeed, modeled systems do not exactly approximate the behavior of the real-world systems, as it remains difficult to model the adaptive properties of the real-world system parameters, or to make the control parameters of the model fit exactly those of the real-world system. In more complex systems, the number of control parameters is too large and cannot be managed [70]. In order to discard all these hard approximations, a direct processing of the time series is surely needed.

The nonlinear analysis of time series from real-world systems has been shown to be the most direct link between chaos theory and the real world [44]. Nonlinear time series analysis is then considered as a reliable tool for the study of complex dynamics and the concept of low-dimensional chaos is becoming more and more effective for the understanding of many complex phenomena [47, 50], although discriminating between chaos and stochastic data remains an open problem [31, 64]. In this work, we shall deal with deterministic systems.

Much as nonlinear time series analysis is the most direct link between chaos and the

real world, complexity is the effective method for comparing time series. It applies to diverse areas of applied science and engineering, including physics, chemistry, biology, finance and industrial applied mathematics [5, 12, 13, 32]. The main complexity parameters are entropies, fractal or correlation dimension and the Lyapunov exponent. As these definitions are not made for arbitrary series of observations or require an infinite observation time, they appear to be less suitable for real-time applications and less accurate for decision making. For example, the existing methods for the estimation of the largest Lyapunov exponent do not provide stable estimates since the scaling of the exponential growth of the initial perturbation requires large and noise-free time series [7].

Developing techniques to understand the internal behavior of a dynamical system given only its observed outputs has been so far crucial for various fields of research. In addition to the above listed complexity measures, there are various basic methods for time series analysis such as the Fourier transform, wavelet transforms, and many others [42, 52, 69]. Unfortunately, the Fourier transform as well as other conventional methods have been shown to be inappropriate for the classification of stochastic or chaotic data [70]. For example, the Fourier transforms of Gaussian noise and uniform noise are similar, although the two types of noise have two different probability distributions. Therefore, statistical methods based on the probability distributions appear to be more suitable for such a classification. In chaos theory, a deterministic dynamical system generating non-regular dynamics is said to be chaotic and the ability to quantify chaos (or the degree of randomness) is an important question with applications ranging from physiological data analysis (electroencephalogram, electrocardiogram ...), robotics (stability analysis of robotic control systems) to the stability of the solar system. Detecting chaos from an arbitrary series of observations remains a challenging task [1, 4, 19, 20, 38, 55], as it is difficult to make a clear difference between chaotic and stochastic dynamics. Some investigations have been carried out in this area and are giving promising results [11, 31, 64]. If the system is assumed to be deterministic, measuring its complexity is useful for determining whether its behavior is predictable or not. Progress has been made in developing tests for chaos [7, 22, 28] and various complexity measures have been developed, which let us to compare time series and distinguish between regular and non-regular behaviors. Some examples of application can be found in meteorology where the time prediction is of crucial importance.

As we have just said, existing theoretical complexity measures such as Lyapunov exponents, Kolmogorov-Sinai (KS) entropy, correlation dimension and many others are difficult to estimate from a finite data set, while empirical measures of complexity like the renormalized entropy or the approximate entropy often lack a theoretical foundation or are not easy to interpret [2, 58, 62]. Moreover, most of these complexity measures do not perform well in the presence of noise and require large computation times so that they cannot be used for real-time applications. Considering all these difficulties of applying theoretical complexity measures to experimental data, new algorithms have been developed. Among them, one can quote the 0-1 test and the ordinal pattern based algorithms, as they can be directly applied to the series of observations [4, 8, 30, 40, 57, 59]. The 0-1 test for chaos detection from time series was proposed in 2004 by Gottwald and Melbourne. The test has the advantage of being binary as it outputs 0 for regular dynamics and 1 for non-regular dynamics. The 0-1 test has exhibited competitive results and has been successfully applied to many types of dynamical systems and experimental data [35, 36, 37]. It is still being improved and has recently been slightly modified for an efficient application to strange non-chaotic attractors (SNA) [34]. The 0-1 test is sensitive to the sampling frequency. Gottwald and Melbourne showed that in the case of continuous time systems, it can fail to detect chaos in oversampled time series and requires the sampling frequency to be reduced to the Nyquist frequency. However, such a condition is not consistent with the digital signal processing requirement that the sampling frequency needs to be greater than the Shannon limit. In order to overcome such a limiting property, we proposed the modified 0-1 test in which the 0-1 test is applied to the local maxima and minima of the observations, instead of directly being applied to the entire observation [25]. This modified 0-1 test thus allows us to easily detect chaos from oversampled time series. However, despite this improvement, the 0-1 test remains computationally costly and cannot be used for real-time analysis of time series. Moreover, the calibration of the test sometimes depends on the system under study, and the 0-1 test by itself does not distinguish between quasi-periodic and periodic orbits, or quasi-periodic and weakly chaotic orbits.

We dedicate particular attention to ordinal pattern-based algorithms as they are fast and robust against noise, therefore can be used for real-time applications. We define an ordinal pattern to be any pattern obtained by considering the order relation between values in a time series. In 2001, Bandt and Pompe proposed the basic algorithm, namely the permutation

entropy (PE) [4], which is actually widely used in many fields due to its conceptual and computational simplicity. The PE is based on the ordinal pattern analysis and is easily calculated for any type of time series, be it regular, chaotic, noisy, or reality based. It has been successfully applied to the study of structural changes in time series and the underlying system dynamics [9, 10, 45, 46, 48]. In addition to its robustness against noise, it has been verified that the PE behaves similarly to the largest Lyapunov exponent (LLE) and can therefore be used for the detection of chaos in dynamical systems [3].

However, although regular dynamics exhibit vanishing or negligible complexities, there is no particular value or property of the PE for detecting this as it is the case for the LLE, which makes the PE less suitable for chaos detection. Indeed, in some examples of chaos detection, PE tracks the LLE with a uniform bias that depends on the underlying system and the parameter setting of the PE algorithm: even perfectly predictable dynamics are measured as having nonzero entropy. The dependence on the uniform bias can sometimes be difficult to determine when dealing with an unknown single time series. Despite the modification proposed by the weighted PE [3] and the modified PE [6] algorithms to overcome some shortcomings of the PE, no solution has been proposed to address this concern. According to its implementation description, a technique based on the use of lookup tables was presented in [68]. However, defining lookup tables for large permutation orders n is problematic as the number of permutations is equal to $n!$. In the case of the modified PE for example, the number of permutations is given by the corresponding *ordered Bell number*, which is greater than $n!$ [68]. Thus approximating the Kolmogorov-Sinai (KS) entropy from the PE is quite difficult as it requires large n. Moreover, defining a lookup table may not be practicable if the algorithm is implemented for embedded systems. Recently the conditional entropy of ordinal patterns was proposed that provides more reliable estimation of the KS entropy [67] than the PE.

Without prior knowledge of the PE, we proposed another approach for time series analysis, namely the three-state test (3ST) for chaos detection in discrete maps, which has also been shown to belong to the group of ordinal pattern analysis methods [26]. The 3ST presents the advantages of both detecting the regularity or non-regularity and estimating the period of the time series. The difference between the PE and the 3ST comes from the statistical exploitation of the permutations. Indeed, instead of constructing ordinal patterns (permutations) of fixed order n like in the PE, in the 3ST data sequences are ordered using

different values of n and the corresponding permutations are studied. In this approach, no probability is computed as the permutations do not have the same length. Moreover, the permutation list may be very large, depending on the length of the time series, hence it may be memory and computationally costly. For this purpose, each permutation was replaced by its largest slope S. The 3ST can easily detect the period-doubling bifurcation and output the corresponding periods as discrete numbers (periods of stable limit-cycles) [26]. In addition, like other ordinal methods for time series analysis, the 3ST is also computationally low cost and was designed for possible real-time applications. Recently, we proposed an improvement of the 3ST which clearly discriminates between periodic, quasi-periodic and chaotic dynamics [27]. We thus defined λ_P as the sensitivity of the 3ST chaos indicator, namely λ, to the initial phase. We also showed that λ_P is equivalent to computing λ using permutations with fixed order [27]. With this definition, the 3ST and the PE appear closer, even if only the largest slopes of permutations and no probabilistic approach are used in the 3ST algorithm. Taking into account the complex nature of the algorithm used for computing λ_P, we introduced the entropy measure related to the largest slopes, namely the permutation largest slopes entropy (PLSE) [28].

However, despite the proven efficiency of ordinal pattern based algorithms, to the best of our knowledge, their application to quasi-periodically driven systems has never been reported. Indeed, when applied to such systems, ordinal pattern-based algorithms fail to detect SNA and tori as regular dynamics, i.e with zero complexity. The objective of this thesis is to address this concern. We revisit ordinal pattern based algorithms for improving complexity measures from time series. New chaos indicators based on the ordinal arrays (OA) are proposed, namely the OA complexity (OAC) and three OA asymptotic growth indices: the periodicity, the quasi-periodicity and the non-regularity index. The OA growth indices should distinguish between periodic and quasi-periodic dynamics, while the OAC should improve their complexity measure by outputting a nearby zero complexity, which is not possible with the existing ordinal pattern-based entropy and complexity measures. The rest of the work is divided into four chapters: chapter 1 presents the 3ST algorithm; chapter 2 is focused on the permutation largest slope entropy (PLSE) algorithm; chapter 3 presents the matching energy (ME); while chapter 4 investigates the applicability of the OA-based indicators to strange non-chaotic attractors.

Chapter 1

The three-state test (3ST) algorithm

This chapter presents an algorithm for the analysis of the outputs of deterministic dynamical systems, namely the three-state test (3ST). 3ST is designed to distinguish clearly between periodic, quasi-periodic and chaotic dynamics by means of a chaos indicator called the periodicity index. In addition to the common outcomes of the existing tests based on time series analysis, it also allows us to estimate the period of stable limit-cycles. In simulations, data generated from discrete maps and ordinary differential equations were successfully characterized confirming the validity of the method, and the results were compared to those of the Lyapunov exponent.

The algorithms presented in this chapter were published in:

[26] J. S. A. Eyebe Fouda, J. Y. Effa, M. Kom, M. Ali, The three-state test for chaos detection in discrete maps, Applied Soft Computing 13 (2013) 4731-4737.

[27] J. S. A. Eyebe Fouda, W. Koepf, Efficient detection of the quasi-periodic route to chaos by the three-state test, Nonlinear Dyn. 78 (2014) 1477-1487.

1.1 Introduction

Understanding the internal dynamics of a nonlinear system given only its time observation is a key challenge in applied dynamical systems. The most interesting task is to classify systems into deterministic or stochastic, and the easiest is to classify dynamics into regular and non-regular. We recall that in this work we are dealing exclusively with deterministic

systems. Regular dynamics do not depend on the initial conditions of the underlying system. In contrast, non-regular dynamics are sensitive to the initial conditions. If in addition the underlying system is assumed to be deterministic, then non-regular dynamics are said to be chaotic.

Usually, the regular and non-regular behavior of a dynamical system is determined by the sign of the largest Lyapunov exponent (LLE) λ_{Lyap}: if $\lambda_{Lyap} \leq 0$, then the dynamics exhibited by the system is regular; otherwise, it is chaotic. However, computing the Lyapunov exponent is too time consuming, and the algorithms used are noise sensitive and may require the modeling equations of the underlying system. In order to achieve real-time analysis of real-world dynamical systems, fast and robust time series analysis based algorithms are required. In this chapter we present the three-state test (3ST), an ordinal pattern based algorithm designed to distinguish clearly between periodic, quasi-periodic and chaotic dynamics [26, 27]. In addition to the common outcomes of the existing tests based on time series analysis, the 3ST allows us to estimate the period of stable limit-cycles.

1.2 Mathematical foundations

The 3ST considers the properties of periodic and quasi-periodic signals for the definition of the ordinal patterns, which themselves are used for determining whether the dynamics are regular or non-regular. Ordinal patterns are derived from the order relation between values in a time series. Chaos can be seen as the ability of a deterministic system to exhibit new values in the phase space as the time evolves. However, given that the topological space is bounded, the number of distinct values exhibited by the system also can be limited, even though the system is chaotic. Therefore, the above definition needs to be extended. With the ordinal patterns approach, the number of ordinal patterns can increase infinitely with the observation time, although the number of distinct values in the phase space is bounded. This means that although chaos can be detected by counting the number of distinct values in the phase space, it is also useful to know whether the distribution of these values or their time evolution is regular or not. The ordinal pattern based time series analysis can then be considered as a complementary tool for chaos detection.

In nonlinear dynamics, there are three basic types of behaviors: the periodic, quasi-periodic and chaotic dynamics. The two first types belong to the category of regular dynamics while the third one belongs to the category of non-regular dynamics. The 3ST algorithm is assumed to distinguish between these different categories. As it is based on ordinal pattern analysis, its reliability also depends on their definition.

1.2.1 Patterns of periodic dynamics

It is common to characterize periodic dynamics by their period, the period itself being characterized by a basic shape (pattern) so that the whole dynamics can be seen as a repetition of this basic pattern. A simple example we can easily describe is the sinusoid. Indeed, a sinusoidal signal is characterized by its period, and the period itself is characterized by a basic shape so that the sinusoid can be effectively defined as a periodic recurrence of that basic shape. The feature which can better describe the basic shape of the sinusoid is for example its amplitude (also representing its maximum). So, for a dynamics to be sinusoidal, its maximum should take the same value (single value in the phase space) and should also appear periodically in the time space. Using these two characterizing features, the pattern that fits the description of a sinusoid is derived from the map of the time evolution of its maximum amplitude: if this local maximum varies as the time evolves or if it is constant, but does not appear periodically, the signal cannot be said sinusoidal. The maximum of the sinusoid can then be seen as a feature, while a pattern can be derived from its time evolution. This approach can be easily extended to dynamics with more than two harmonics by considering the series of local maxima.

In the case of discrete maps, a time series is said to be periodic if there exists a basic shape which is periodically repeated as the time evolves.

Definition 1.2.1. A time series $\mathrm{x} = \{x_t\}_{t=0,1,\ldots,T-1}$ of length T is called period-L cycle or simply L-periodic, if there exists a basic pattern of length q samples containing L distinct values ($L \leq q$) periodically repeated, independently of the time origin. q is known as the time space period and L as the phase space period.

In Fig. 1.1 are shown some examples of periodic signals. It clearly appears that L is the number of distinct values per period, while q is the total number of values per period of the time series.

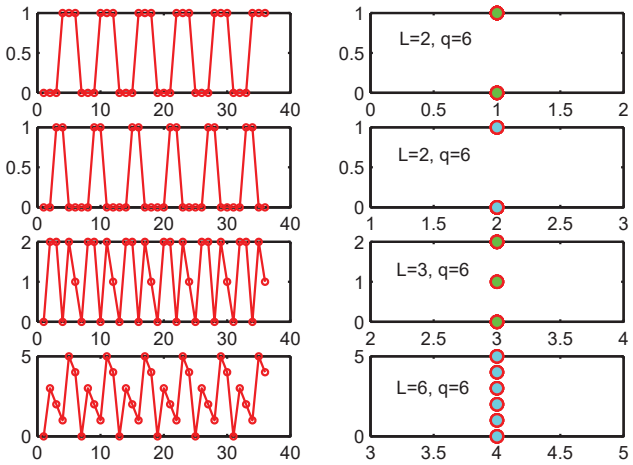

Figure 1.1: Example of periodic signals with various phase space periods L and time space period $q = 6$. In the left side is shown the time representation, while the right side corresponds to the phase space representation.

Definition 1.2.2. Let $\{x_t\}_{t=0,1,\ldots,T-1}$ be a data series of length T, g a sorting function such that $\{u_t\} = g(\{x_t\})$ is the data series containing the values of $\{x_t\}$ sorted into ascending order (identical values are sorted by the ascending order of their time index), and f a function such that $\mathrm{v} = f(\{u_t\})$ is the series of time indices of the values of $\{u_t\}$ in $\{x_t\}$. We define the *ordinal transform* to be the function $\mathcal{F} = f \circ g$ such that $\mathrm{v} = \mathcal{F}(\mathrm{x})$. $\mathcal{F}$ is a function which associates to an input time series x the series of time indices $\mathrm{v} = \{v_t\}_{t=0,1,\ldots,T-1}$ of its values sorted into ascending order. The argument of $\mathcal{F}$ can be a list or a vector of real numbers, while the corresponding output v is a list or a vector (permutation) of natural numbers.

If for example $\mathrm{x} = \{x_t\}_{t=0,1,\ldots,T-1}$ is such that $x_5 < x_{T-1} < x_0 < \ldots < x_3$, then the series of indices $\mathrm{v} = \mathcal{F}(\{x_t\})$ is equal to $\mathrm{v} = \{5, T-1, 0, \ldots, 3\}$.

Proposition 1.2.1. *Let $\{x_t\}_{t=0,1,\ldots,T-1}$ be an L-periodic time series of length $T \geq 2L$ with $L = q$, the corresponding series of time indices $\mathrm{v} = \mathcal{F}(\{x_t\})$ is a piece-wise linear function whose all the increasing linear segments present the same slope, and this slope is equal to the phase space period L of the time series.*

Proof. Let us assume that the length of $\{x_t\}$ is such that $T = L \cdot N$, where $N \geq 2$ is the number of periods observed. $\{u_t\} = g(\{x_t\})$ is a stair function having L stairs each of

length N. All the values in a stair are identical and two consecutive values $u_t = x_{v_t}$ and $u_{t+1} = x_{v_{t+1}}$ in a stair belong to two consecutive periods of $\{x_t\}$. So, their positions in $\{x_t\}$ are such that $v_{t+1} - v_t = L$. Now let us apply this relation to each stair of the series of time indices:

- First stair:
  The first stair contains N samples, that is

$$U_0 = \left\{u_0, u_1, \ldots, u_{N-1}\right\} = \left\{x_{v_0}, x_{v_1}, \ldots, x_{v_{N-1}}\right\}.$$

  Their positions in $\{x_t\}$ verify the relation $v_{t+1} - v_t = L$. This relation can be recursively written and generalized as $v_{t+i} = L \cdot i + v_t$. By setting $t = 0$ for the first element, the relation can be simplified to $v_i = L \cdot i + v_0$, where v_0 is the position of u_0 in $\{x_t\}$ and $0 \leq i \leq N-1$. u_0 is the first smallest value of $\{x_t\}$. It is now clear that the slope of the first stair is equal to L.

- Second stair:
  The second stair corresponds to the following samples:

$$U_1 = \left\{u_N, u_{N+1}, \ldots, u_{2N-1}\right\} = \left\{x_{v_N}, x_{v_{N+1}}, \ldots, x_{v_{2N-1}}\right\}.$$

  Using the same technique as for the first stair, but setting now $t = N$, we obtain $v_{N+i} = L \cdot i + v_N$, where v_N is the position of u_N in $\{x_t\}$ and $0 \leq i \leq N-1$. u_N is the first value of $\{x_t\}$ greater than u_0. Once more, it is clear that the slope of the second stair is equal to L.

- L-th stair:
  It corresponds to

$$U_{L-1} = \left\{u_{(L-1)N}, u_{(L-1)N+1}, \ldots, u_{LN-1}\right\} = \left\{x_{v_{(L-1)N}}, x_{v_{(L-1)N+1}}, \ldots, x_{v_{LN-1}}\right\}.$$

  In the same way as for the previous two stairs, but setting $t = (L-1)N$, the elements of the series of time indices vary as $v_{(L-1)N+i} = L \cdot i + v_{(L-1)N}$, where $v_{(L-1)N}$ is the position of $u_{(L-1)N}$ in $\{x_t\}$ and $0 \leq i \leq N-1$. $u_{(L-1)N}$ is the first greatest value of $\{x_t\}$. The slope of the L-th stair, similar to the two previous ones, is equal to L and recursively, we can extend this demonstration to the other ramps of v.

Given that $0 \leq i \leq N-1$ for all the ramps, it can be rewritten as $i = t \mod N$. The set of initial values for all the ramps is $\mathrm{v}^0 = \{v_0, v_N, \ldots, v_{(L-1)N}\}$ and the corresponding values are $\{u_j^0\}_{j=0,1,\ldots,L-1} = \{u_0, u_N, \ldots, u_{(L-1)N}\}$. Each of them is the first element of the different L stairs of $\{u_t\}$, so they all belong to the first period of $\{x_t\}$. Consequently, v^0 can be expressed as $\mathrm{v}^0 = \mathcal{F}(\mathrm{x}^0)$, where $\mathrm{x}^0 = \{x_0^0, x_1^0, x_2^0, \ldots, x_{L-1}^0\}$ is the basic period of $\{x_t\}$. Thus, v^0 is the series of time indices corresponding to the basic period of $\{x_t\}$ sorted into ascending order; so it depends on the ordering of the L distinct samples in x^0. As each element of v^0 is unique, the initial value of each ramp of v is unique and ranges from 0 to $L-1$. Finally, the general term of v_t describing the behavior of the series of time indices v can be expressed as

$$v_t = L \cdot (t \mod N) + v^0_{\lfloor \frac{t}{N} \rfloor}. \tag{1.2.1}$$

Equation (1.2.1) shows that v_t is a piece-wise linear function presenting L linear ramps with the same slope $S = L$, which ends the proof.

□

Following from Proposition 1.2.1, a periodic dynamics with $L = q$ can be efficiently described by its slope $S = L = q$, as predicted. Furthermore, this slope does not depend on the ordering v^0 of the values in the basic period x^0 of $\{x\}$.

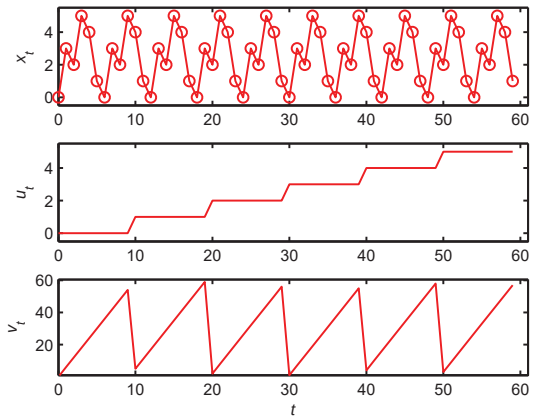

Figure 1.2: Example of period-6 signal and the corresponding series of time indices $\{v_t\}$. The results confirms that all the ramps of $\{v_t\}$ present the same slope $S = 6$

Example 1.2.1. *Let* $\mathrm{x} = \{0, 3, 2, 5, 4, 1, 0, 3, 2, 5, 4, 1, \ldots\}$ *be a period-6 time series observed*

on $N = 10$ periods, as shown in Fig. 1.2. Its basic period is $\mathrm{x}^0 = \{0, 3, 2, 5, 4, 1\}$ *and the series of time indices of the corresponding ordered version* u^0 *is* $\mathrm{v}^0 = \{0, 5, 2, 1, 4, 3\}$. *The general term of the series* $\{v_t\}$ *can then be written as* $v_t = 6 \cdot (t \mod N) + v^0_{\lfloor \frac{t}{N} \rfloor}$. *The corresponding plot is shown in Fig. 1.2 where* $\{v_t\}$ *is a function with 6 ramps which all present the same slope* $S = 6$.

Changing the basic shape into $\mathrm{x}^0 = \{0, 2, 3, 5, 4, 1\}$ *will also change the basic series of indices into* $\mathrm{v}^0 = \{0, 5, 1, 2, 4, 3\}$, *but the slope will remain unchanged.*

Proposition 1.2.2. *Let* $\{x_t\}_{t=0,1,\ldots,T-1}$ *be a L-periodic time series of length* $T \geq 2q$ *with* $L < q$, *the largest slope S of the corresponding series of time indices* $\mathrm{v} = \mathcal{F}(\{x_t\})$ *is equal to q iff there exists at least one non-repeated value in the basic period* x^0 *of* $\{x_t\}$.

Proof. Let us assume that the length of $\{x_t\}$ is such that $T = q \cdot N$, where $N \geq 2$ is the number of periods observed and $A = \{a_0, a_1, \ldots, a_j, \ldots, a_{L-1}\}$ the set of distinct samples. $\{u_t\} = g(\{x_t\})$ is a stair function presenting L stairs each of length $r_j \cdot N$, where r_j is the number of repetitions of a_j in the basic period x^0 of $\{x_t\}$. The repetitions are such that $\sum_{j=0}^{L-1} r_j = q$. Non-repeated values are those for which $r_j = 1$. Let us assume that there is a non-repeated value a_j in x^0. It ocurs only once per period and according to Proposition 1.2.1, the time indices of the ramp of the corresponding stair are such that $v_{t+i} = q \cdot i + v_t$, hence the corresponding slope is equal to q.

Now let us assume that all the samples in the basic period are repeated, and consider a twice repeated ($r_j = 2$) sample a_j. Let x_{t+i} and x_{t+k} be two occurrences of a_j belonging to the l-th period of $\{x_t\}$, with $i < k$. Their repetitions in the $(l+1)$-th period are respectively x_{t+i+q} and x_{t+k+q}. The series of times indices of the stair of $\{u_t\}$ corresponding to this value can be written as $\{\ldots, t+i, t+k, t+i+q, t+k+q, \ldots\}$. The corresponding slopes are $(k-i) < q$ as x_{t+i} and x_{t+k} belong to the same period, and $(i+q-k) < q$.

This technique, which can easily be extended to $r_j > 2$, shows that the slopes corresponding to repeated values are all smaller than q. So, the largest slope S equals q only for non-repeated values, which ends the proof.

□

Example 1.2.2. *Let us consider* $N = 10$ *periods of the period-3* ($q = 6$) *time series* $x = \{0, 3, 2, 3, 2, 2, 0, 3, 2, 3, 2, 2, 0, 3, 2, 3, 2, 2, \ldots\}$ *shown in Fig. 1.3. Its basic period is* $\mathrm{x}^0 =$

$\{0, 3, 2, 3, 2, 2\}$ *and the series of time indices of the corresponding ordered version* u^0 *is* $\mathrm{v}^0 = \{0, 2, 4, 5, 1, 3\}$. *It can be observed in that case that only the ramp corresponding to the non-repeated sample is linear and its slope* $S = 6$ *is the largest one.*

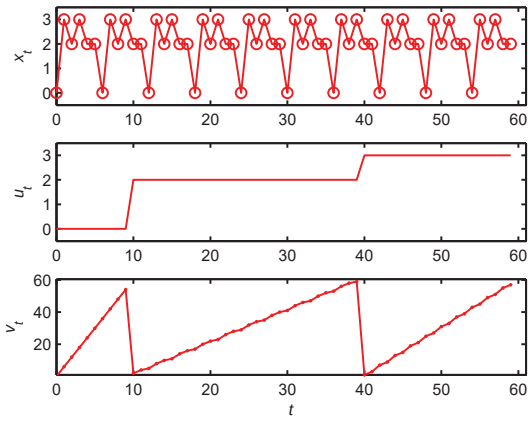

Figure 1.3: Example of period-3 signal with redundant values, and the corresponding series of time indices $\{v_t\}$. The results confirm that only the ramp of $\{v_t\}$ corresponding to the non-repeated value presents a slope $S = 6$

Finally, we can conclude that the series of time indices of a periodic dynamics is a piecewise linear function presenting a largest slope S which is equal to its time period q if its basic period contains at least one non-repeated value, and smaller than q otherwise. From the proof of Proposition 1.2.2, in the case all the values in x^0 are repeated, the largest slope of v depends on v^0 and is such that $S(\mathrm{v}^0) < q$. Nevertheless, one can notice that the largest slope is independent of the length T $(T \geq 2q)$ of the time series.

1.2.2 Patterns of quasi-periodic dynamics

By definition, a quasi-periodic dynamics contains at least two incommensurable frequencies, i.e their ratio is an irrational number. According to this definition, the number of distinct values cannot be rigorously determined as for periodic dynamics, due to the irrational ratio of the constitutive frequencies. However, as quasi-periodic dynamics are known to be regular, we agree that a quasi-periodic time series x can be seen as a dynamics presenting a large basic pattern which can be isolated only after a long observation time. Considering that the observation time in practice is not too large, it is difficult to fix such a basic shape

and all the samples in x are assumed to be different. Therefore, applying $\mathcal{F}$ to x outputs a series of time indices v which exclusively depends on the ordering of the whole set of values x. An example of quasi-periodic dynamics is derived from the sine-circle map whose equation is

$$x_{t+1} = \left[\Omega + x_t + \frac{r}{2\pi}\sin\left(2\pi x_t\right)\right] \mod 1, \tag{1.2.2}$$

where $x_0 = 0.3$, $\Omega = \frac{\sqrt{5}-1}{2}$ and $r = 0$.

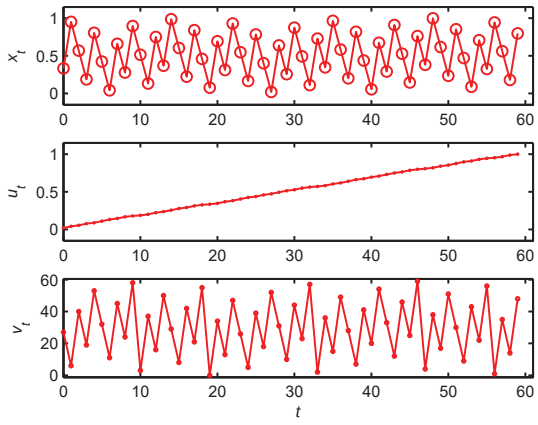

Figure 1.4: Example of quasi-periodic signal, and the corresponding series of time indices $\{v_t\}$.

As each value x_t is assumed to appear only once in x, the series of ordered values is no longer a stair function. This observation implies that although v remains a piece-wise linear function, the number of ramps cannot be properly determined, and depends on the ordering of x. Moreover, its behavior may change as the observation time grows, given that the number of distinct samples depends on the observation time T. Considering that the behavior of v changes as the observation time grows, we see that its largest slope S also depends on time, and approaches a limit value L for $T \to \infty$, under to the assumption that a basic pattern occurs after a long observation time T. Assuming that no repetition occurs in the basic period, the pattern of the quasi-periodic dynamics can be approximated by

$$L = \lim_{T\to\infty} S(T). \tag{1.2.3}$$

Fig. 1.5 shows an example of behavior of the largest slope corresponding to the dynamics presented in Fig. 1.4. It clearly appears on this figure that the largest slope in that case

depends on the observation time T. There are ranges of T where the largest slope is constant. We can also observe that the width of intervals of T where $S(T)$ is constant is increasing as $T \to \infty$, thus suggesting that there may exist a limit value L of the largest slope.

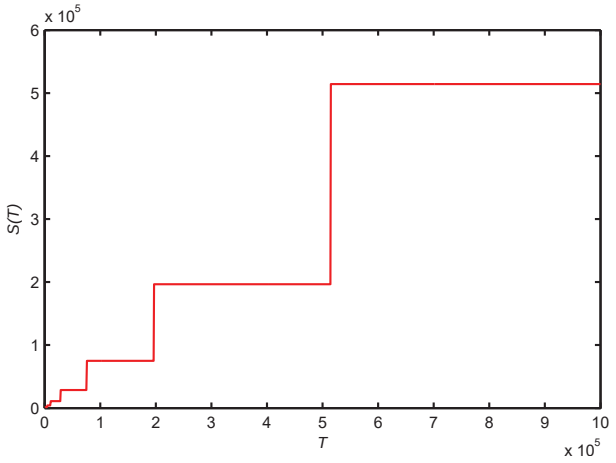

Figure 1.5: Behavior of the largest slope of a quasi-periodic dynamics in terms of the observation time T.

The largest slope expresses how large the number of features (distinct values) in the pattern is, so it can be efficiently used as a pattern describer. It is simply expressed as

$$S(T) = \max\Big(v_{t+1,T} - v_{t,T}\Big). \tag{1.2.4}$$

In the case of non-regular dynamics, the detection of a basic pattern is not possible and the period also cannot be estimated. The largest slope is then assumed to increase faster in terms of T than in the case of quasi-periodic dynamics. From the above considerations we derived the 3ST algorithm.

1.3 Description of the 3ST algorithm

The 3ST considers the properties of periodic and quasi-periodic signals for determining whether a dynamics is regular or not. It studies the ordering of data in the time series as a function of time, given that chaos manifests itself both in time and space. The corresponding shape for each observation time is considered as a pattern (qualitative description). For the

pattern to be quantitatively described, the data sequence is sorted into ascending order, and the largest slope S of the resulting sequence of time indices is retained as a pattern describer. Applying statistical analysis to the series of largest slopes allows us to determine chaos indicators such as the asymptotic growth rate K and the periodicity index λ_{3ST}.

1.3.1 Principle of the 3ST algorithm

Given a time series x, the principle of the 3ST algorithm consists to splitting it into Q sub-series $\mathrm{x_j}$ of length T_j, with $T_j < T_{j+1} < \cdots < T_Q$, and then to derive a set of largest slopes $\{S_j\}$. Let us consider for example a time series $\{x_t\}$ containing ten values such that $\{x_t\} = \{4, 7, 9, 10, 6, 11, 3, 2, 13, 5\}$. Let us also consider $Q = 4$ subsets of $\{x_t\}$ such that: $\mathrm{x_0} = \{4, 7, 9, 10, 6, 11, 3\}$, $\mathrm{x_1} = \{4, 7, 9, 10, 6, 11, 3, 2\}$, $\mathrm{x_2} = \{4, 7, 9, 10, 6, 11, 3, 2, 13\}$ and $\mathrm{x_3} = \{4, 7, 9, 10, 6, 11, 3, 2, 13, 5\}$ and thereafter apply the ordinal transform $\mathcal{F}$ to each subset. We obtain respectively the following series of time indices: $\mathrm{v_0} = \{7, 1, 5, 2, 3, 4, 6\}$, $\mathrm{v_1} = \{8, 7, 1, 5, 2, 3, 4, 6\}$, $\mathrm{v_2} = \{8, 7, 1, 5, 2, 3, 4, 6, 9\}$, and $\mathrm{v_3} = \{8, 7, 1, 10, 5, 2, 3, 4, 6, 9\}$. Considering the definition of the largest slope and applying it to each series of time indices, the following largest slopes are respectively obtained: $S_0 = 4$, $S_1 = 4$, $S_2 = 4$ and $S_3 = 9$.

In Fig. 1.6, it can be seen from top to bottom some particular behaviors of S for periodic dynamics with $n > L$, $n < L$ and chaotic dynamics respectively. We used for this example the logistic map whose equation of motion is given by:

$$x_{t+1} = r x_t \Big(1 - x_t\Big), \tag{1.3.1}$$

where $0 \leq r \leq 4$ is the control parameter, and $0 \leq x_t \leq 1$. The efficiency of the 3ST algorithm is based on the statistical exploitation of these three basic behaviors.

1.3.2 Determination of the asymptotic growth rate K

Statistically, the analysis of the behavior of the largest slopes is well described by the measurement of the standard deviation σ_S of S expressed by:

$$\sigma_S(T, n) = \sqrt{\frac{1}{Q} \sum_{j=0}^{Q-1} \Big(S_j - \bar{S}\Big)^2} \tag{1.3.2}$$

where

$$\bar{S} = \frac{1}{Q} \sum_{j=0}^{Q-1} S_j. \tag{1.3.3}$$

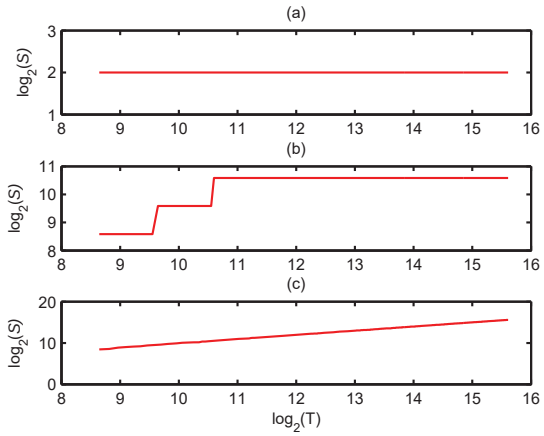

Figure 1.6: Example of observation time dependency of the largest slope (S). Dynamics are generated from logistic map (Eq. (1.3.1)) with $x_0 = 0.5$: (a) periodic dynamics ($r = 3.5$), (b) periodic dynamics with large period ($r = 3.84943363$), and (c) chaotic dynamics ($r = 3.86$).

S_j is the largest slope corresponding to the subset x_j whose length is $T_j = jp_0 + n$; $T = (Q-1)p_0 + n$ is the length of the data series, p_0 is the integration step, Q is a natural number different from zero (number of slopes evaluated), and n is the smallest observation time for the largest slope to be well evaluated. n should satisfy the relation $n < T$. In our example, $T = 10$, $Q = 4$, $p_0 = 1$ and $n = 7$.

$\sigma_S(T, n)$ measures the ability of a dynamical system to generate new patterns as time evolves. So, $\sigma_S(T, n)$ is bounded if the underlying dynamics is regular, according to the behavior of S [26]. We showed in the previous section that S remains constant for periodic motions, and assumed that S increases up to a limiting value in the case of quasi-periodic dynamics. For non-regular dynamics we assume that S is an increasing function of T as it can be observed in Fig. 1.6.

Assuming that $\sigma_S(T, n)$ increases linearly in the data length T, the growth rate is determined as follows:

$$\mu(T, n) = \frac{\log\Big(1 + \sigma_S(T, n)\Big)}{\log(T)}. \tag{1.3.4}$$

The asymptotic growth rate K of the largest slope is thus obtained as the limit value of $\mu(T, n)$:

$$K(n) = \lim_{T \to \infty} \mu(T, n). \tag{1.3.5}$$

Equation (1.3.5) shows that $K(n)$ is a non-negative indicator ($K(n) \geq 0$). $K(n)$ allows us

to distinguish between regular ($K(n) = 0$) and non-regular ($K(n) > 0$) motions. When the dynamics is periodic, the standard deviation is equal to zero, as S remains constant for any value of T, provided that $n > q$. For dynamics with large period (assumed to be quasi-periodic motions), the growth of S up to a limiting value results in a decrease in σ_S to zero, thus leading to $K(n) = 0$ also. Fig. 1.7 shows the behavior of the asymptotic growth rate $K(n)$ corresponding to the dynamics presented in Fig. 1.6. Given that $K(n) = 0$ for both periodic and quasi-periodic dynamics, we require another criterion for discerning between these two types of regular dynamics. We thus suggest to analyze the behavior of the growth rate μ.

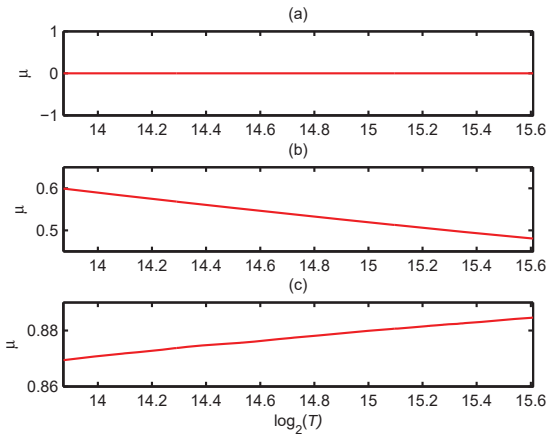

Figure 1.7: Example of observation time dependency of the growth rate (K) for the previous dynamics shown in Fig. 1.6: (a) periodic dynamics ($r = 3.5$), (b) periodic dynamics with large period ($r = 3.84943363$), and (c) chaotic dynamics ($r = 3.86$). The first value of σ_S is computed with 300 values of S.

1.3.3 Determination of the periodicity index λ_{3ST}

From the definition of the asymptotic growth rate K, both periodic and quasi-periodic dynamics are characterized by $K = 0$. In order to distinguish between these two types of dynamics, we propose to model the evolution rule of $\mu(T, n)$ in terms of T. While looking at the behavior of the growth rate μ in Fig. 1.7, it clearly appears that periodic dynamics with large periods present a decreasing growth rate function while periodic dynamics with $q < n$ present a constant growth rate equal to zero. In the case of chaotic dynamics, we also

also observe that μ does not behave linearly in terms of T. We thus suggest approximating its behavior by an exponential growth. For this purpose, the set of largest slopes $\{S_j\}$ is divided into P subsets S_k of length m_k such that such that $m_0 < m_1 < \ldots < m_{P-1}$. Indeed, each subset S_k is assumed to derive from a subset x_k of length $T_k \leq T$, which itself is derived from the initial time series $\{x_t\}$. Thus, assuming that μ behaves as

$$\mu(T_k, n) = \mu_0 + K_0 \cdot \exp\Big(- \lambda_{3ST}(n) \cdot \frac{T_k}{T}\Big) \tag{1.3.6}$$

where μ_0 and K_0 are constant values and $u_k = \frac{T_k}{T}$, $0 \leq T_k \leq T$, is the normalized integration time, the value of λ_{3ST} can be easily determined by exponential fitting.

From Eq. (1.3.4), $\mu = 0$ for $T_0 = 0$ ($u_k = 0$), hence $\mu_0 = -K_0$; as the maximum value of μ is approximately equal to 1, one can set $\mu_0 = 1$. Thus, including μ_0 in Eq. (1.3.6) and using exponential fitting leads to

$$\lambda_{3ST}(n) = \lim_{T_1 \to \infty} \frac{\sum_{k=1}^{P} \Big[u_k \cdot \Big(\Gamma(T_k, n) - \overline{\Gamma} \Big) \Big]}{\sum_{k=1}^{P} \Big[u_k \cdot \Big(u_k - \bar{u} \Big) \Big]} \tag{1.3.7}$$

where $\Gamma(T_k, n) = -\log\Big(1 - \mu(T_k, n)\Big)$.

Finally, the 3ST is based on the interpretation of the sign of $\lambda_{3ST}(n)$: for periodic dynamics, obviously $\lambda_{3ST}(n) = 0$ and for chaotic motions, $\mu(T, n)$ increases as a function of the observation time, hence $\lambda_{3ST}(n) > 0$. Based on the assumption made on the definition of quasi-periodic signals, $\mu(T, n)$ is decreasing as the observation time increases, thus implying $\lambda_{3ST}(n) < 0$. Another important result of the 3ST is the estimation of the period L of stable limit-cycles as

$$L = \lim_{T \to \infty} |S| \tag{1.3.8}$$

1.3.4 Algorithmic steps for the computation of λ_{3ST}

In this section, we summarize the algorithmic steps for computing the periodicity index λ_{3ST}.

Algorithm 1

---

1. Consider a time series x of length T;

2. Divide x into Q subsets x_j of length n_j such that $\mathrm{x}_0 \subset \mathrm{x}_1 \subset \ldots \subset \mathrm{x}_j \subset \ldots \subset \mathrm{x}_{Q-1}$, and $n_0 = n$;

3. Apply $\mathcal{F}$ to each sequence to obtain the largest slope S_j of the resulting series of time indices;

4. Divide the set S of largest slopes into P subsets S_k of length m_k such that $\mathrm{S}_0 \subset \mathrm{S}_1 \subset \ldots \subset \mathrm{S}_k \subset \ldots \subset \mathrm{S}_{P-1}$, and $m_0 > 2$;

5. For each S_k, compute the standard deviation σ_{S_k} and deduce the corresponding growth rate μ_k;

6. From the set of μ_k, deduce λ_{3ST} using Eq. (1.3.7), with $u_k = \frac{m_k}{P}$;

7. Consider $L = S_{Q-1}$ as the estimated period of the time series.

1.3.5 Phase sensitivity of the periodicity index (λ_P)

The three behaviors of μ presented in Fig. 1.7 are well described by three states of λ_{3ST}: $\lambda_{3ST} = 0$, $\lambda_{3ST} < 0$ and $\lambda_{3ST} > 0$. However, in the case of quasi-periodic dynamics, λ_{3ST} may alternate between positive and negative values, depending on the observation time. If this happens, the nature of the dynamics cannot be determined as it is considered as regular for $\lambda_{3ST} < 0$ (quasi-periodic) and non-regular for $\lambda_{3ST} > 0$. This observation requires to complete or extend the description of the quasi-periodic dynamics by the 3ST.

Quasi-periodic dynamics are well known as regular. As a consequence of this basic knowledge, the periodicity index should not depend on the initial conditions or on the initial phase, and The largest slope only depends on the parameter setting of the 3ST (n, T). Thus, the largest slope is the same for different sequences of the same length $T_k = M$ derived from a quasi-periodic dynamics. In this section, we evaluate the dependency of the periodicity index on the initial conditions and initial phase.

The dependency on the initial conditions assumes that there are at least two different time series (two stimuli) with different initial conditions, while the initial phase dependency refers to the time delay in a single time series. Indeed, the period of a regular dynamics should not be sensitive to the initial conditions. For periodic motions for example, the period

depends on neither the initial conditions, nor the initial phase. Quasi-periodic signals can be seen as signals with at least two competitive incommensurable frequencies. Although there is no defined period, a fixed largest slope should be found for the same parameter setting, independently of the initial condition or the initial phase. It then turns out that the 3ST should output the same period (largest slope) as well as the same periodicity index. Fig. 1.8 shows an example of behavior of the largest slope for the dynamics considered in Fig. 1.5, from where it can be verified that it remains constant for various initial phases, with a fixed value of M. Indeed, we considered a time series of length T and a sliding window of length M, and then computed the largest slope for each position i of the window.

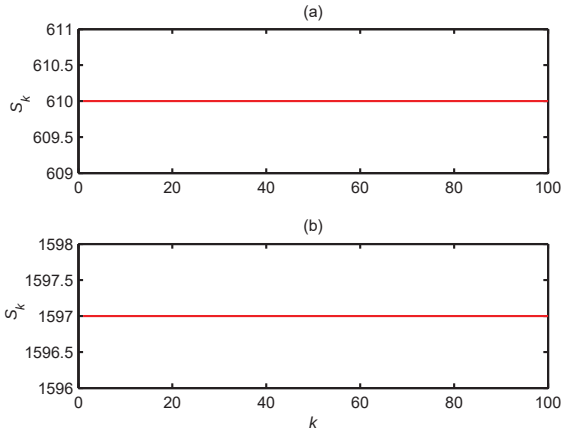

Figure 1.8: Behavior of the largest slope of series of indices derived from quasi-periodic sequences of the same length (a): $M = 1000$ and (b): $M = 2000$.

In dynamical systems, chaotic (non-regular) dynamics are those which are sensitive to initial conditions. So, let x_0 and x_1 be two time series generated from the same system with two different initial conditions. Applying the 3ST to each of them outputs two periodicity indexes λ^0_{3ST} and λ^1_{3ST} respectively. In order to evaluate the influence of the initial conditions, we can consider the sensitivity of the periodicity index λ_{3ST} on the initial conditions as

$$\lambda_C(n) = \frac{1}{\log(T)} \log\left(1 + \xi \cdot \left|\lambda^1_{3ST}(n) - \lambda^0_{3ST}(n)\right|\right). \tag{1.3.9}$$

$\xi \gg 1$ is a scaling factor to improve the readability of the result. The sensitivity of λ_{3ST} on initial conditions lets us to distinguish between regular ($\lambda_C(n) = 0$) and non-regular ($\lambda_C(n) > 0$) dynamics.

However, computing λ_C requires at least two time series (stimuli) derived from the same system with different initial conditions. In some practical cases, the decision needs to be taken from a single time series. For this purpose, let us consider a time series $\mathrm{x} = \{x_t\}_{t=0,1,\ldots,T-1}$ and a sliding rectangular window W_M^i of length $M < T$ centered at time index $M_0 + i$, with $M_0 = \frac{M}{2}$ and i the delay time (phase shift), and define the sensitivity of the periodicity index on the initial phase or time delay. Indeed, for each sequence corresponding to a position i (referring to the initial phase) of the sliding window, the 3ST will output a periodicity index λ_i. We can then consider λ_i as the periodicity index obtained from $\mathrm{x}^i = \mathrm{x} \cdot W_M^i$ and λ_{i+1} as the one obtained from $\mathrm{x}^{i+1} = \mathrm{x} \cdot W_M^{i+1}$. For example, let us consider $\mathrm{x} = \{4, 7, 9, 10, 6, 11, 3, 2, 13, 5\}$ and W_5^i a 5-length window centered at $3 + i, i = 0, 1, 2, 3, 4, 5$. Applying the sliding window to x_0 with $i = 0$ and $i = 1$ outputs $\mathrm{x}^0 = \{4, 7, 9, 10, 6\}$ and $\mathrm{x}^1 = \{7, 9, 10, 6, 11\}$, respectively. Extending this principle to the whole time series, we define the sensitivity of λ_{3ST} on the initial phase or delay time as

$$\lambda_P(n) = \frac{1}{\log(M)} \log \left(1 + \xi \cdot \sqrt{\sum_{i=0}^{i_{max}} \Big(\lambda_i(n) - \lambda_0(n) \Big)^2} \right) \tag{1.3.10}$$

with $i \in \mathbb{N}$. λ_P is determined from a single time series by considering different time delays and sequences of the same length M. Indeed, as in Fig. 1.8, series of time indices derived from quasi-periodic sequences of the same length exhibit the same largest slope. Dynamics which are not sensitive to initial conditions, even those which are sensitive to the initial phase, are considered as regular. The following detection approach is then proposed:

- Regular dynamics: $\lambda_C(n) = 0$;
- Non-regular dynamics: $\lambda_C(n) > 0$.

In the class of regular dynamics, periodic and quasi-periodic dynamics can be also distinguished as follows:

- Periodic dynamics: $\lambda_{3ST}(n) = 0$ and $\lambda_P(n) = 0, \forall i_{max} > 0$;
- Quasi-periodic dynamics: $\lambda_{3ST}(n) \neq 0$ and $\lambda_P(n) = 0, \forall i_{max} > 0$.

Periodic dynamics are insensitive to both initial phase and initial conditions and their periodicity index is equal to zero; quasi-periodic dynamics also are insensitive to both initial

phase and initial conditions but their periodicity index is different from zero while non-regular dynamics are sensitive to both time delay and initial conditions. According to the above observations, periodic and quasi-periodic dynamics can be distinguished by looking at the values of λ_{3ST} and λ_P exclusively. λ_C may be used for discerning between non-regular dynamics and regular dynamics which are sensitive to initial phase. The 3ST can thus help detecting efficiently quasi-periodic dynamics as regular as well as the quasi-periodic route to chaos from a single stimulus.

1.3.6 Algorithmic steps for the computation of λ_P

The computation of λ_P as above described is time consuming as it requires more than two values of λ_i. By reinterpreting the its definition, the term $\sqrt{\sum (\lambda_i(n) - \lambda_0(n))^2}$ can be seen as a single value of λ_i evaluated from sequences of the same length M, thus reducing the number of values of λ_i to be computed. The following algorithm is then proposed for a fast computation of λ_P.

Algorithm 2

---

1. Consider a time series x of length T;
2. Choose the length M of the sliding window W_M^i for scanning the whole time series and the number Q of largest slope to compute;
3. For each position i of W_M^i, apply $\mathcal{F}$ to the corresponding subsequence x_i and deduce the largest slope S_i of the resulting series of indices;
4. Evaluate λ_i as described in steps 4 to 6 of **Algorithm 1**;
5. Deduce $\lambda_P(M)$ from Eq. (1.3.9) where $\sqrt{\sum[\lambda_i(n) - \lambda_0(n)]^2}$ is replaced by $|\lambda_i|$ computed in step 4.

Finally, the outputs of the 3ST algorithms are the periodicity index λ_{3ST}, the sensitivity of the periodicity index to the initial phase λ_P and the period of limit cycles L. These three outputs are interpreted as follows:

- $\lambda_{3ST} > 0$ and $\lambda_P > 0$: the system is chaotic;

- $\lambda_{3ST} \neq 0$ and $\lambda_P = 0$: the system is quasi-periodic;

- $\lambda_{3ST} = 0$ and $\lambda_P = 0$: the system is periodic, a stable limit cycle with period $L \leq q$.

1.4 Example of chaos detection in the logistic map

Most of the researchers in the field of nonlinear dynamics are familiar with the rich nature of the logistic map (Eq. (1.3.1)) [17]. It is commonly used for the period doubling bifurcation it exhibits and has been widely studied in literature. In this example, we apply the 3ST to the logistic map to verify its efficiency for the detection of such a period doubling bifurcation, as well as for determining the period of stable limit-cycles. We also evaluate the impact of the 3ST parameters on the results. For this purpose, we took 501 values of the control parameter satisfying $3.5 \leq r \leq 4$, and with step size $\Delta r = 10^{-3}$. The spectra of the periodicity index and the sensitivity of the periodicity index to the initial phase are compared to the Lyapunov exponent λ_{Lyap}. For this experiment, the data length is set to $T = 20\,000$, while the 3ST parameters are set as: $n = 50$, $M = 10\,000$, $Q = 100$, $P = 70$ and $m_0 = 30$. For easier interpretation of λ_P, we set $\xi = 10^6$ for all the simulation results.

1.4.1 Estimation of the period of stable limit-cycles

The Feigenbaum diagram is given in Fig. 1.9 for comparison with the period L of limit-cycles in periodic windows. By comparing these two diagrams, it is observed that the 3ST by means of the cycle diagram clearly detects the period of stable limit-cycles. It is outputting a natural number even for regular dynamics with large periods where the Feingenbaum diagram is showing a large number of dots which is difficult to interpret. Indeed, for limit-cycles with large periods, one may confuse in the bifurcation diagram between regular dynamics and chaotic dynamics. For $r = 3.602$ for example, the system exhibits period-88 dynamics. While looking at the Feigenbaum diagram, such a dynamics is not easily observed as regular, whereas the cycle diagram clearly indicate $L = 88$. However, in order to make sure that such dynamics are clearly regular another decision making parameter is required, hence the use of the Lyapunov exponent.

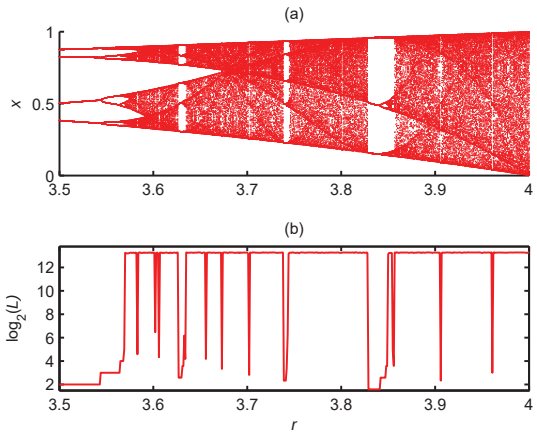

Figure 1.9: Comparison between the Feingenbaum diagram and the spectrum of the period of limit-cycles of the logistic map (a) Feigenbaum diagram, (b) cycle diagram.

1.4.2 Chaos detection by λ_{3ST} and λ_P spectra

The main advantage by using the 3ST algorithm resides in the fact that it outputs at once the period L and the chaos indicators λ_{3ST} and λ_P. So, even limit-cycles with large periods are easily detected, without needing further tests. In Fig. 1.10 we see λ_{Lyap}, λ_{3ST} and λ_P for a comparison of the chaos detection efficiency of the Lyapunov exponent and the 3ST algorithm. This figure clearly shows that periodic windows are well detected by the 3ST algorithm, as compared to the Lyapunov exponent λ_{Lyap}. Results of λ_{Lyap} and λ_P are consistent as $\lambda_P = 0$ when $\lambda_{Lyap} < 0$. We can then conclude that the dependence of the periodicity index on the initial phase may be efficiently used for the detection of the periodic route to chaos. However, to the best of our knowledge, there is no quasi-periodic dynamics in the logistic map. By rigorously interpreting the result in Fig. 1.10, one should conclude that dynamics for which $\lambda_{3ST} < 0$ and $\lambda_P = 0$ are quasi-periodic. For $r = 3.602$ for example, a rigorous interpretation of the 3ST results indicates that the dynamics is quasi-periodic, whereas it corresponds to a period-88 dynamics. In order to avoid such a false detection, the value of n needs to be increased. By choosing $n > 88$ for example, the previous period-88 dynamics will be detected as periodic. This observation also proves that $\lambda_{3ST} < 0$ does not necessarily indicate a quasi-periodic dynamics, but perhaps a dynamics whose period is greater than n.

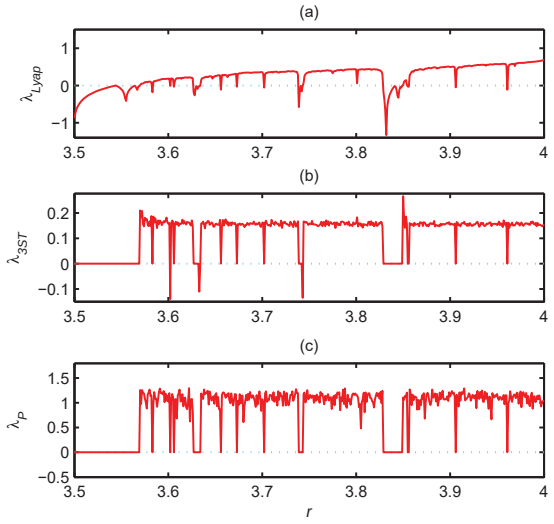

Figure 1.10: Spectra of (a) λ_{Lyap}, (b) $\lambda_{3ST}(n)$ and (c) $\lambda_P(M)$ (sensitivity to the initial phase). The 3ST parameters are: $n = 50, N = 20000, Q = 100, P = 70, m_0 = 30, M = 10000$.

1.5 Example of detection of the quasi-periodic route to chaos

For the detection of the quasi-periodic route to chaos, we consider the sine-circle map defined in Eq. (1.2.2). It can exhibit periodic, quasi-periodic or chaotic behaviors depending on the frequency ratio and the nonlinearity parameters, i.e. Ω and r, respectively. For $0 \leq r \leq 1$, the system dynamics is either periodic (frequency-locked) or quasi-periodic depending on whether the value of the frequency ratio parameter is rational or irrational. As the nonlinearity parameter r approaches zero, the system exhibits quasi-periodic behavior for all values of the frequency ratio parameter Ω. As the nonlinearity parameter r approaches one, frequency-locked steps extend to eventually occupy the whole Ω axis when r is equal to one. In this case, there is a special fraction of Ω value called the most irrational Ω_c. This value corresponds to the "golden mean" ($\Omega_c = \frac{\sqrt{5}-1}{2}$) winding number $\mathcal{W} = \lim_{t\to\infty} \frac{x_t - x_0}{t}$ if the frequency ratio parameter Ω is locked to its critical value Ω_c [10]. Shortly after this critical value in the (r, Ω) plane, $(1, \Omega_c)$ is the edge of the quasi-periodic route to chaos since chaotic behavior can occur. All these characteristic shapes in the (r, Ω) plane are called "Arnold Tongues" in the literature. For the $r > 1$ region where the nonlinearity parameter r is dominant for the system dynamics, there are periodic regions with different periods,

chaotic regions, and so edges of the periodic route to chaos [10].

As in the case of the logistic map, a sequence of length $N = 20000$ samples after transient die out (5000 samples), is considered as time series x for each value of the control parameter $0 \leq r \leq 2.5$, taken with step size $\Delta r = 0.01$. The initial conditions are set to $x_0 = 0.5$. Fig. 1.11 shows the bifurcation diagram of the sine circle map for $\Omega = \Omega_c$ and the behaviors of λ_{3ST} and λ_P.

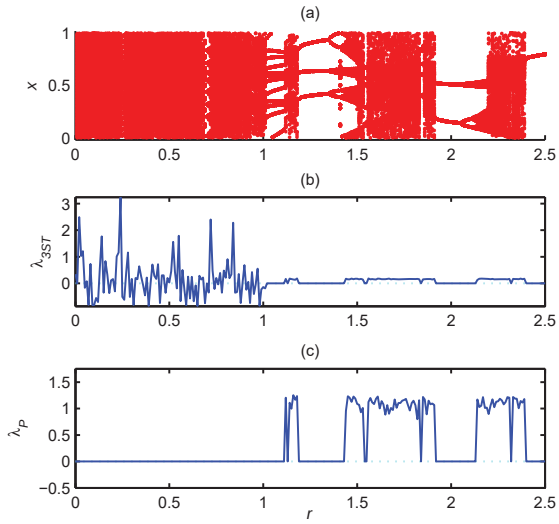

Figure 1.11: Detection of the quasi-periodic route to chaos: (a) bifurcation diagram, (b) diagram of λ_{3ST} and (c) diagram of λ_P. The 3ST parameters are: $n = 50, N = 20000, Q = 100, P = 70, m_0 = 30$.

It is observed from this figure that λ_{3ST} fails to properly characterize quasi-periodic dynamics. Sometimes it is detecting them as regular with large periods ($\lambda_{3ST} < 0$) and sometimes as chaotic ($\lambda_{3ST} > 0$). However, combining λ_{3ST} and λ_P allows to clearly distinguish between quasi-periodic and chaotic dynamics. The complete interpretation is the following [27]:

- $\lambda_{3ST} > 0$ and $\lambda_P > 0$: the dynamics is chaotic;
- $\lambda_{3ST} > 0$ and $\lambda_P = 0$: the dynamics is quasi-periodic;
- $\lambda_{3ST} = 0$ and $\lambda_P = 0$: the dynamics is periodic;

- $\lambda_{3ST} < 0$ and $\lambda_P = 0$: the dynamics may be periodic or quasi-periodic, depending on the choice of n as compared to the period of the dynamics.

Indeed, as we just said in the case of the logistic map, choosing $n < L$ leads to negative values of λ_{3ST}. Similarly, one may get $\lambda_{3ST} < 0$ for some quasi-periodic dynamics. We then conclude in that case that the underlying dynamics is regular. Nevertheless, the above results confirm the efficiency of the 3ST for the detection of the quasi-periodic route to chaos. We can also observe that using a single time series for computing λ_P is enough for the detection of the periodic and quasi-periodic dynamics ($\lambda_P = 0$).

1.6 Applicability of the 3ST algorithm to continuous time systems

Applying the 3ST algorithm to continuous time systems requires considering the data as noise contaminated, given that the acquisition process undoubtedly induces some errors due to sampling and quantization processes. In the case of simulation data, the error due to the integrator used as well as the choice of the sampling step can be considered as noise sources. Thus, for the algorithm to be efficiently used, it is necessary to reduce a priori the noise effect, hence to define an appropriate noise reduction algorithm.

1.6.1 The differential dynamical quantization (DDQ)

For the 3ST to be useful for the detection of regularity, it should output zero values for regular dynamics even in the presence of noise. However, we observed that the algorithm is extremely sensitive to small changes, so to the noise effect. In order to reduce this sensitivity, we suggest reducing the data precision. Indeed, by considering values with a too high precision, even very close samples are detected as different, which contributes to increasing the noise sensitivity of the algorithm. Reducing the data precision requires the definition of a new quantization step for the data series. We also suggest considering a new quantization method, namely the *differential dynamical quantization* (DDQ) [28].

The DDQ is a nonlinear approach which consists of assigning a single value (quantum) to those which are approximately the same in the data series. We thus define the *noise threshold* (or noise tolerance) η as its quantization step. Indeed, η is defined as the minimum

difference between x_t and $x_{t'}$ for two values that are considered as different. With this definition, it clearly appears that η can be considered as the precision of the quantized time series. As only a maximum number of T values is allowed in a quantized time series of length T, we suggest to consider η as

$$\eta \geq \frac{\max(\{x_t\} - \min(\{x_t\}))}{T}. \tag{1.6.1}$$

It should be noticed that whenever the true precision η_0 of the input time series is smaller than η ($\eta_0 > \eta$), the quantization has no effect on the output of the 3ST algorithm. For example, choosing $\eta = 10^{-5}$ for a 10-bits encoded time series has no impact on the 3ST result. For the 3ST algorithm to be sensitive to η in that case, we must take $\eta > 1/1024$.

The DDQ algorithm thus applies as follows: the $\{x_t\}$ values are first sorted into ascending order to obtain $\{u_t\}$ in which all equal values are neighbors; thereafter u_t and u_{t+1} are set to $u_{t'+1}$ if $|u_t - u_{t+1}| < \eta$ and $t' < t$, with t' such that $|u_{t'} - u_{t'+1}| \geq \eta$; else, these values are left unchanged; finally the quantized or noise reduced series $\{v_t\}$ is obtained by relocating the values of $\{u_t\}$ as in $\{x_t\}$. By this approach, the DDQ is used for reducing the precision of the series $\{x_t\}$, but the range of values is not explicitly determined as is the case for the other quantization methods. Indeed, the precision in $\{v_t\}$ is equal to η, but the range of data depends on the input time series. Then the 3ST is applied to $\mathbf{v}_t$. The algorithmic steps are the following:

Algorithm 3

---

1. A threshold or noise tolerance η is defined as the quantization step;

2. $\{x_t\}$ values are first sorted in ascending order to obtain $\{u_j\}$ in which all equal values are neighbors;

3. thereafter u_j and u_{j+1} are set to $u_{j'+1}$ if $|u_j - u_{j+1}| < \eta$ and $j' < j$, with j' such that $|u_{j'} - u_{j'+1}| \geq \eta$; otherwise, these values are left unchanged;

4. finally the quantized series v=$\{v_t\}$ is obtained by relocating the values of $\{u_j\}$ as in $\{x_t\}$

If for example $\{x_t\} = \{2.12, 2.61, 2.53, 2.30, 2.44, 2.28\}$, $t = 0, 1, \ldots, 5$, then the sorted sequence is $\{u_j\} = \{2.12, 2.28, 2.30, 2.44, 2.53, 2.61\}$. Setting $\eta = 0.04$ leads to $\{u_j\} = \{2.12, 2.28, 2.28, 2.44, 2.53, 2.61\}$, and finally $\{v_t\} = \{2.12, 2.61, 2.53, 2.28, 2.44, 2.28\}$. It appears that $x_3 = 2.30$ was noise contaminated and has been replaced by $v_3 = 2.28$. The choice of the right value of η depends on the noise amplitude ε.

Instead of sorting the data into ascending order, we can also consider descending order or both ascending and descending orders. Although the quantized sequence depends on the type of sorting used, we verified that only the noise contaminated samples are taking different values, while the others remain unchanged. It turns out that the detection result does not depend on the type of sorting. For the above example, if the data are sorted by descending order instead, then we will find that $x_5 = 2.28$ was noise contaminated and it will be replaced by 2.30. So, the change involves only $x_3 = 2.30$ and $x_5 = 2.28$.

1.6.2 Example of chaos detection in the Duffing oscillator

Data generated from the system are considered as noise contaminated due to the sampling process and the precision of the integrator. Thus, for the 3ST result to be efficiently determined, the use of the DDQ for noise reduction is required. The 3ST can be directly applied to the continuous time series or to the series of local extrema. The Duffing system is described by the following system of ordinary differential equations

$$\begin{cases} \dot{x} = y \\ \dot{y} = x - ay - x^3 + r\cos(z) \\ \dot{z} = \omega \end{cases} \tag{1.6.2}$$

where $\dot{(\cdot)} = d(\cdot)/dt$ and r is the control parameter. We used the fourth order Runge-Kutta algorithm to solve Eq. (1.6.2) with sampling step $T_s = 4\pi/1000$. We set $a = 0.3$ and $\omega = 1.25$. For the analysis of this system, the observation time is set to $\frac{200\pi}{\omega}$ after transient die out ($\frac{200\pi}{\omega}$). The 3ST algorithm is then applied to the noise reduced version of solutions x_t and y_t and only the maximal value of the corresponding outputs is retained. The result depends on the choice of η, which itself depends on the sampling frequency F_s and the precision of the integrator. We recommend choosing the largest sampling frequency possible, as the largest frequency F_{max} of the spectra of x_t and y_t is not a priori known. For this experiment, we set $\eta = \frac{T_s}{10}$ independently of the sequence to be analyzed, where $T_s = \frac{1}{F_s}$

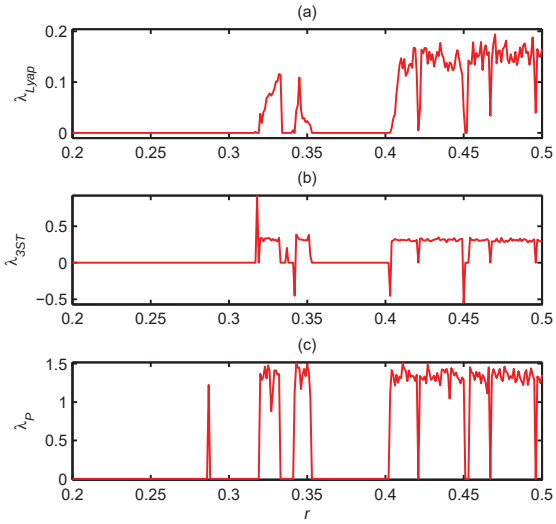

Figure 1.12: Chaos and limit-cycle detection in the forced Duffing system: (a) spectrum λ_{Lyap}, (b) spectrum of the maximum λ_{3ST} and (c) spectrum of the maximum λ_P. The control parameter r varies from 0.2 to 0.5. The 3ST parameters are: $n = 5000, M = 15000, Q = 100, P = 70, m_0 = 30$.

is the sampling period. This value of noise tolerance $\eta = 0.0013$ is effectively greater than the absolute tolerance $AbsTol = 10^{-5}$ and the relative tolerance $RelTol = 10^{-6}$ of the integrator.

We thus consider that times series $\{x_t\}$ and $\{y_t\}$ are corrupted by a small amount of noise of amplitude $\varepsilon \leq T_s/10$, due to sampling and numerical integration. Taking $\eta = T_s/10$ and applying the DDQ to $\{x_t\}$ and $\{y_t\}$, we obtained the result in Fig. 1.12 which shows the spectra of the the largest Lyapunov exponent λ_{Lyap}, the periodicity index λ_{3ST} and the sensitivity of the periodicity index to the initial phase λ_P.

As in the case of the logistic map, 3ST results are consistent with those of the Lyapunov exponent and allow us to easily detect limit-cycles. For the comparison to be plausible we have considered the largest periodicity index for 3ST, given that only the largest Lyapunov exponent is considered. However, we observe other possibilities which were not described previously: $\lambda_{3ST} = 0$ and $\lambda_P > 0$ ($r = 0.288$), $\lambda_{3ST} < 0$ and $\lambda_P > 0$ ($r = 0.4$). As compared to the Lyapunov exponent, the first case corresponds to a periodic dynamics and indicates a transition between two stable limit-cycles (see Fig. 1.14); while the second combination clearly indicates a chaotic dynamics. These decisions can also be confirmed by readjusting

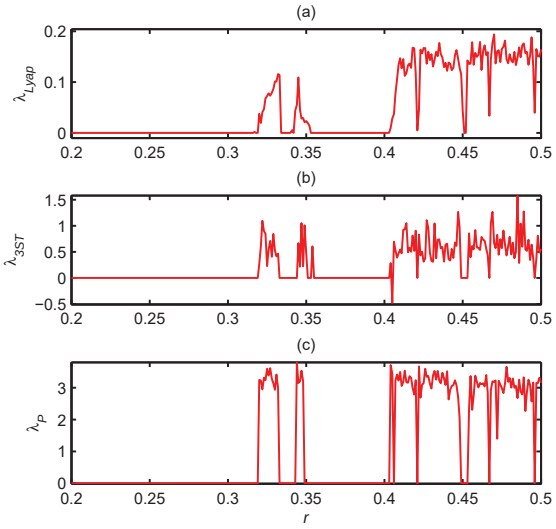

Figure 1.13: Chaos detection in the forced Duffing oscillator using the series of local maxima: (a) spectrum of λ_{Lyap}, (b) spectrum of the maximum λ_{3ST} and (c) spectrum of the maximum λ_P. The control parameter is set as $0.2 \leq r < 0.5$ (step size $\Delta r = 10^{-3}$), and the 3ST parameters as $n = 20$, $M = 40$, $Q = 50$, $P = 35$ and $m_0 = 15$.

the parameter setting or by using the series of local extrema.

Indeed, instead of considering the whole continuous time series $\{x_t\}$ and $\{y_t\}$, the 3ST can also be applied to the series of their local extrema. However, one should take care of the data length as the number of extrema strongly depends on the phase space period of the underlying dynamics. The results obtained are depicted in Fig. 1.13 where we used the series of local maxima. As compared to λ_{3ST} obtained with the continuous time series, the result of the series of local maxima is easily interpretable (there are no more cases with $\lambda_{3ST} < 0$ and $\lambda_P > 0$). In contrast, as compared to λ_P, the result of the continuous time series is closer to the Lyapunov exponent than the one obtained with the series of local maxima; but this result strongly depends on the parameter setting. For this example, we set the 3ST parameters as $n = 20$, $M = 40$, $Q = 50$, $P = 35$ and $m_0 = 15$.

As well, the detection of the period of periodic cycles is well performed by 3ST as shown in Fig. 1.14.

One can clearly observe the period doubling bifurcation for $0.2 \leq r \leq 0.319$ for both x_t and y_t variables. For $r = 0.467$, the system exhibits a period-7 dynamics. There are also some parameter values where the periods of the two variables are different, e.g for $r = 0.38$

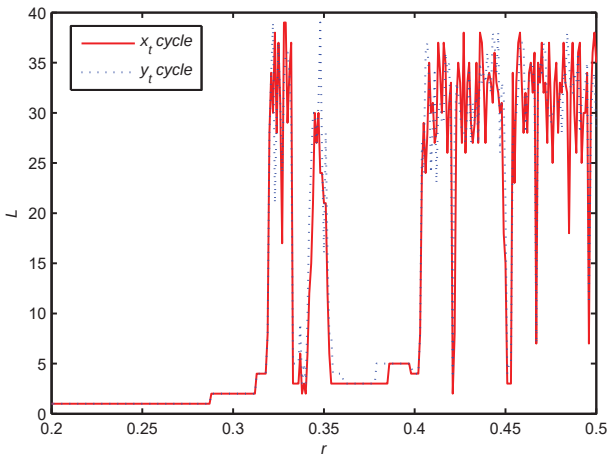

Figure 1.14: Cycle diagrams of variables x_t and y_t. This diagram is obtained using the local maxima of the corresponding variables. The control parameter r varies from 0.2 to 0.5.

where the period of x_t is $L_x = 3$ and that of y_t is $L_y = 5$; and $r = 0.496$ where $L_x = 7$ and $L_y = 11$. In Fig. 1.15 we show some examples of phase portraits of periodic dynamics. Without noise reduction, the corresponding periods are respectively $L_x = L_y = 26$ for $r = 0.3$, $L_x = 36, L_y = 35$ for $r = 0.38$, $L_x = L_y = 14$ for $r = 0.467$, and $L_x = 7, L_y = 37$ for $r = 0.496$. Looking at Fig. 1.15(a) ($r = 0.3$), the use of the DDQ is helpful as it allows us to obtain the period shown by the phase portrait. Indeed, by zooming into this plot, there are clearly other lines which are too close each other, confirming the presence of what we consider as noise due to sampling, integration and approximation errors (the approximation of π for example induces some errors).

1.6.3 Example of chaos detection in the Rössler system

The Rössler system is a three dimensional nonlinear system defined by

$$\begin{cases} \frac{dx}{dt} = -(y+z) \\ \frac{dy}{dt} = x + ry \\ \frac{dz}{dt} = r + z(x-a) \end{cases} \tag{1.6.3}$$

where $a = 4.3$ and r is the control parameter. For this example, we set the sampling period to $T_s = 0.01$ and the control parameter as $0.05 \leq r \leq 0.5$. The integration duration is set to 2500 time units after transient die out (300 time units). The corresponding Lyapunov

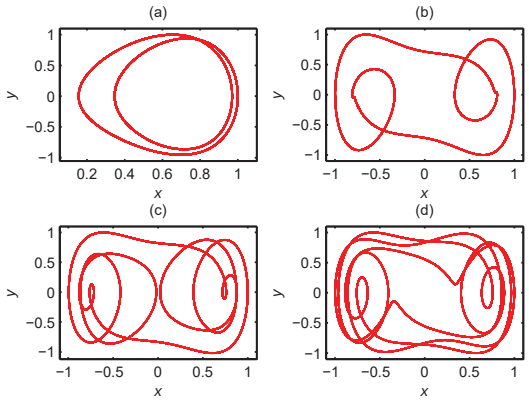

Figure 1.15: Example of phase portraits of periodic dynamics: (a) $r = 0.3$ ($L_x = L_y = 2$), (b) $r = 0.38$ ($L_x = 3, L_y = 5$), (c) $r = 0.467$ ($L_x = L_y = 7$) and (d) $r = 0.496$ ($L_x = 7, L_y = 11$).

and 3ST spectra are shown in Fig. 1.16. For a better readability of the results, we plotted $\log(1 + 4\lambda_{3ST})$ instead of λ_{3ST} itself. One can then appreciate the effectiveness of the 3ST algorithm, except for some particular values of the control parameter. Indeed, for $r < 0.196$, according to the Lyapunov spectrum, the system is exhibiting limit cycles, whereas the 3ST spectrum is showing some peaks indicating transitions between these limit cycles. For $r = 0.125$ for example, 3ST indicates a chaotic dynamics, which is not in accordance with the Lyapunov exponent. The observed peak in this example indicates the transition between a period-1 cycle and a period-2 cycle. Increasing the sampling frequency or considering more samples in transient die out can make the transition bandwidth very fine, but do not suppress it. By setting $T_s = 0.001$ for example, the dynamics is detected as period-2 cycle while it is detected as period-1 cycle for $T_s = 0.01$. The appearance of false detection is thus due to the transition between period-1 and period-2 cycles.

1.7 Influence of the parameter setting

Getting right results with the 3ST requires suitable good parameter settings. For this purpose, it is useful to analyze the impact of each parameter on the result. There are three main parameters, namely n, M and Q.

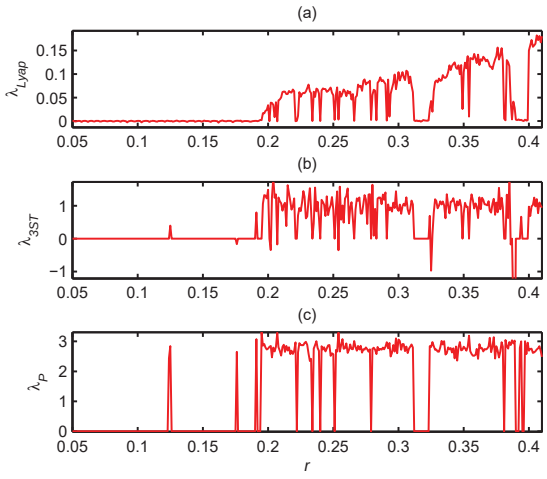

Figure 1.16: Chaos detection by the 3ST algorithm in the Rössler system: (a) spectrum of the largest Lyapunov exponent (λ_{Lyap}), (b) spectrum of the maximum λ_{3ST} and (c) spectrum of the maximum λ_P. The control parameter is set as $0.05 \leq r < 0.5$ (step size $\Delta r = 10^{-3}$), and the 3ST parameters as $n = 90$, $M = 70$, $Q = 50$, $P = 35$ and $m_0 = 15$.

1.7.1 Influence of parameters n and M

The parameter n is the smallest data length for the largest slope to be well evaluated. n determines the upper limit of the period that can be estimated without bias. Any periodic dynamics whose period is less than n is detected by $\lambda_{3ST} = 0$ while those for which the period is greater than n may be detected by $\lambda_{3ST} < 0$. This observation also confirms that $\lambda_{3ST} < 0$ describes both quasi-periodic and periodic dynamics, but not exclusively quasi-periodic dynamics as predicted in [26, 27]. The choice of n can help to detect transitions between different types of dynamics (periodic-periodic, periodic-chaotic...).

The parameter M is acting in λ_P similarly as n in λ_{3ST}. It indicates the largest period which can be detected without error. When the period of the underlying dynamics is greater than M, the algorithm outputs a largest slope close to M for all the positions of W_M. It then results in $\lambda_P = 0$, confirming that the dynamics are regular. The larger M, the more accurate the computation of λ_P and the larger the computational time.

Fig. 1.17 presents the behavior of λ_{3ST} as a function of n and λ_P as a function of M for periodic ($r = 1.05$), quasi-periodic ($r = 0$) and chaotic ($r = 1.7$) dynamics derived from the sine-circle map. n is varying from 10 to 400 by step size $\Delta n = 1$, while M is varying

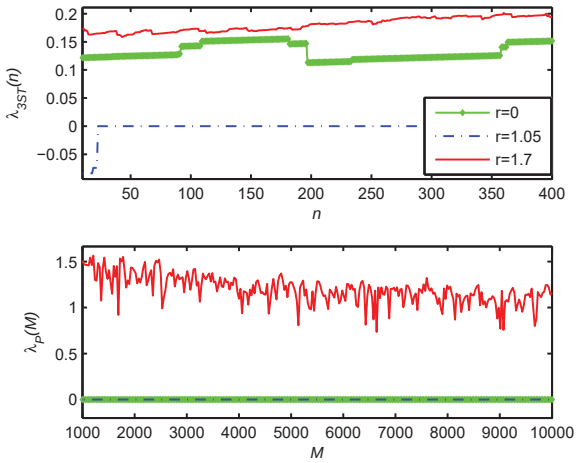

Figure 1.17: Dependence of λ on n and λ_P on M, $10 \leq n \leq 400$ by step size $\Delta n = 1$ and $10^3 \leq M \leq 10^4$ by step size $\Delta M = 30$, for periodic ($r = 1.05$), quasi-periodic ($r = 0$) and chaotic ($r = 1.7$) dynamics derived from the sine-circle map. The other 3ST parameters are: $N = 20000, Q = 100, P = 70, m_0 = 30$.

from 10^3 to 10^4 by step size $\Delta M = 30$. $r = 1.05$ corresponds to a dynamics whose period is $L = 22$ and $\lambda_{3ST} < 0$ for $n < 22$. It can be concluded from Fig. 1.17 that the choice of n does not influence the 3ST result, provided that dynamics with $\lambda_{3ST} < 0$ are interpreted as regular dynamics with period larger than n. In the case of λ_P, some errors can occur at the transitions between different types of dynamics (quasi-periodic to periodic, periodic to chaotic, ...)

1.7.2 Influence of parameter Q

The choice of the parameter Q is less constraining than that of n as it determines the integration step. The maximum value of Q is $Q = N - n$ which corresponds to an integration step $p_0 = 1$. Q should be chosen such that the computation of λ is statistically feasible. The larger Q, the smaller the integration step and the larger the computational time. For small data length, Q can be set to its maximum value. However, m_0 which is the smallest number of largest slopes used for computing σ_S should be chosen such that $m_0 \ll Q$. The behavior of λ in terms of Q is shown in Fig. 1.18 and confirms that there is no need to consider very large values of Q as compared to the data length.

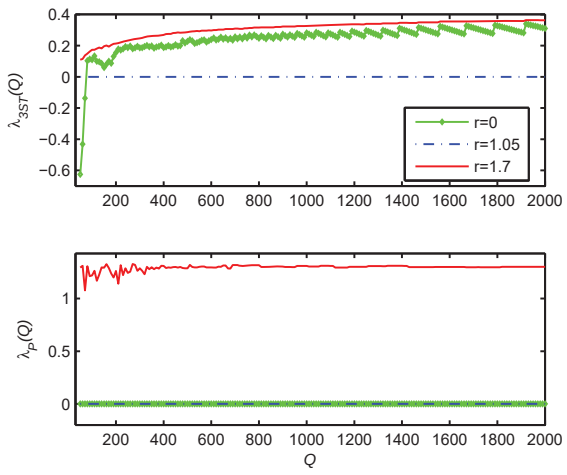

Figure 1.18: Dependence of λ on Q, Q varying from 50 to 2000 by step size $\Delta Q = 10$, for periodic ($r = 1.05$), quasi-periodic ($r = 0$) and chaotic ($r = 1.7$) dynamics derived from the sine-circle map. The other 3ST parameters are: $n = 50, M = 5000, N = 20000, m_0 = 30$ and $P = Q - m_0$.

1.8 Conclusion

In this chapter, we presented the 3ST algorithm for discerning between periodic, quasi-periodic and chaotic dynamics. The algorithm gives satisfactory results in the case of discrete maps. While dealing with continuous time systems, a prior noise reduction step should be considered. Three different combinations of λ_{3ST} and λ_P are necessary for decision making: the pair ($\lambda_{3ST} = 0$, $\lambda_P = 0$) which describes periodic dynamics; the combination ($\lambda_{3ST} \neq 0$, $\lambda_P = 0$) implying quasi-periodic dynamics and ($\lambda_{3ST} > 0$, $\lambda_P > 0$) indicating chaotic dynamics. Nonetheless, it should be pointed out that there are other combinations, ($\lambda_{3ST} \leq 0$, $\lambda_P > 0$) for example, whose interpretation is not clearly determined. Moreover, the algorithm is very sensitive to the parameter setting, and for some inappropriate setting, the 3ST may not allow to clearly distinguish between periodic and quasi-periodic dynamics, or between quasi-periodic and weakly chaotic dynamics. In addition, the number of parameters required is large and users may get confused while setting them. For this purpose, we opt in chapter 2 for an algorithm based on entropy measure applied to the largest slopes, and which involves few parameters.

Chapter 2

The permutation largest slope entropy (PLSE)

In this chapter we present the entropy related to the permutation largest slopes as an efficient approach for distinguishing between regular and non-regular dynamics. The permutation largest slope entropy (PLSE) is seen as a simplified algorithm for computing the phase sensitivity of the periodicity index of 3ST (λ_P) as presented in chapter 1, so as to improve its dependency on the large number of parameters involved. We theoretically establish that, for suitably chosen delay times, permutations generated in the case of regular dynamics present the same largest slope if their order is greater than the period of the underlying orbit. This investigation helps us make a clear decision in the detection of regular dynamics with large periods for which permutation entropy (PE) for example gives nonzero complexity measure. We also extend the investigation to the detection of strange nonchaotic attractors (SNA).

The algorithms presented in this chapter have been published in:

[23] J. S. A. Eyebe Fouda, Applicability of the permutation largest slope entropy to strange nonchaotic attractors, Nonlinear Dyn. (Submitted)

[24] J. S. A. Eyebe Fouda, B. Bodo, G. M. D. Djeufa, and S. L. Sabat, Experimental chaos detection in the duffing oscillator, Commun Nonlinear Sci. Numer. Simulat. 33 (2016), 259-269.

[28] J. S. A. Eyebe Fouda, W. Koepf, Detecting regular dynamics from time series using permutations slopes, Commun. Nonlinear Sci. Numer. Simulat. 27 (2015) 216-227.

2.1 Introduction

Measuring the complexity of a deterministic system is useful for determining whether its behavior is predictable or not. Entropies, fractal dimension and Lyapunov exponent (LE) are some examples of complexity parameters. Particular interest has been given to entropies as some of them can be directly applied to the series of observations [8, 30, 40, 43, 57, 59]. In this perspective, Bandt and Pompe [4] proposed the permutation entropy (PE), which is actually widely used in many fields due to its conceptual and computational simplicity. It has been successfully applied to the study of structural changes in time series and the underlying system dynamics [9, 10, 45, 46, 48]. In addition to its robustness against noise, it has been verified that the PE behaves similarly to the largest Lyapunov exponent and can therefore be used for the detection of chaos in dynamical systems [3]. The PE is based on ordinal pattern analysis, and is easily calculated for any type of time series, be it regular, chaotic, noisy, or reality based.

Unfortunately, although regular dynamics present vanishing or negligible complexities, PE does not give any particular value or property for the characterization of regular dynamics as we have with the LLE, therefore it appears to be less suitable for chaos detection. Indeed, in some examples on chaos detection, PE tracks the largest LE with a uniform bias that depends on the underlying system and the parameter setting of the PE algorithm: even perfectly predictable dynamics are characterized by a nonzero entropy. The dependence on the uniform bias can be sometimes difficult to determine when dealing with an unknown single time series. Some improvements including the weighted PE [21] and the modified PE [6, 68] have been proposed, but none of them has definitely fixed the problem related to the above mentioned bias. Nevertheless, using the recently defined conditional entropy of ordinal patterns [67], a more reliable approximation of the Kolmogorov-Sinai (KS) entropy is obtained.

Without prior knowledge on the PE, we proposed the three-state test (3ST) which also belongs to the class of ordinal pattern analysis methods [26]. As shown in chapter 1, the 3ST has the advantage of performing both the detection of the regularity or non-regularity and the period estimation in time series. The difference between the PE and the 3ST comes from the statistical exploitation of the permutations. Indeed, in the 3ST, instead of constructing ordinal patterns (permutations) of fixed order n like in the PE, data sequences are ordered

using different values of n and the corresponding permutations are studied for computing the periodicity index. With this approach, no probability is computed as the permutations do not have the same length. Moreover, the permutation list may be very large, depending on the length of the time series, hence it is both memory and computationally expensive. For this purpose, each permutation is replaced by its largest slope S. For discerning between periodic, quasi-periodic and chaotic dynamics, the sensitivity of the periodicity index to the initial phase is computed using permutations of fixed length n [27]. With this definition, the 3ST and the PE appear closer, even if only the largest slopes of permutations and no probabilistic approach are used in the 3ST algorithm. However, the fundamental question is to know whether the use of the largest slopes is reliable for chaos detection.

In this chapter, we theoretically prove the usefulness of the permutation slopes for discriminating between regular and non-regular dynamics. We further establish the relationship between the 3ST and the PE and simplify the 3ST algorithm by computing the entropy related to the permutations largest slopes, and show that it can be efficiently applied to the detection of chaos in dynamical systems [24, 28]. We also investigate the applicability of the above algorithm to the detection of strange nonchaotic attractors (SNA) [23].

2.2 Mathematical fundamentals

2.2.1 Brief recap of the PE algorithm

Let $\{x_t\}_{t=0,1,\cdots,T-1}$ be a time series of length T where t is the time index. The PE of order n is defined as the entropy related to permutations of order n [4]. Permutations of order n are obtained from the comparison of neighboring values (increasing order) in embedding vectors $\mathbf{x}_k = \big(x_{k\tau_0}, x_{k\tau_0+\tau} \ldots, x_{k\tau_0+m\tau}, \ldots, x_{k\tau_0+(n-1)\tau}\big)$, where $0 \leq k \leq \lfloor \frac{T-(n-1)\tau-1}{\tau_0} \rfloor$, n is the embedding dimension (number of values in $\mathbf{x}_k$), $\tau_0 \in \mathbb{N}_{\geqq 1}$ is the delay time of the embedding vectors, $\tau \in \mathbb{N}_{\geqq 1}$ is the delay time of samples and $m+1$ the index of $x_{k\tau_0+m\tau}$ in $\mathbf{x}_k$, $0 \leq m \leq n-1$. Let P_k be the permutation derived from $\mathbf{x}_k$, with $\tau_0 = 1$. $P_k = \left(\frac{1,2,3,\ldots,n}{5,n,1,\ldots,3}\right)$ for example is obtained by sorting the values of $\mathbf{x}_k$ into ascending order, with $x_{k+4\tau} < x_{k+(n-1)\tau} < x_k < \ldots < x_{k+2\tau}$. Identical values are sorted by ascending order of their time index. The permutation entropy of order n is thus given by

$$H_p(n) = -\sum p(\theta) \cdot \ln(p(\theta)), \tag{2.2.1}$$

where

$$p(\theta) = \frac{\#\{k \mid 0 \leq k \leq T-(n-1)\tau-1, P_k = \theta\}}{T-(n-1)\tau}, \tag{2.2.2}$$

is the probability of the permutation θ and $\#$ denotes the cardinality [4].

Despite the efficiency of the PE as complexity measure, it remains unsuited for distinguishing between regular and non-regular dynamics. Indeed, obtaining $H_p(n) = 0$ for regular dynamics requires large embedding dimensions n and an observation time $T \gg n!$. This requirement is difficult to satisfy as the memory space is not infinitely large. Therefore n is reduced to small values ($2 \leq n \leq 15$) [4]. As a consequence, $H_p(n) \neq 0$ even for perfectly predictable dynamics. It is evident that regular dynamics cannot be detected as periodic unless the observation time is greater than its period [25, 67]. Let q be the time period of the underlying dynamics, if $n < q$, then the corresponding PE is greater than zero. It then appears from the above restriction that only dynamics with a period less than 15 samples may be detected with zero entropy. Moreover, for a regular dynamics to be detected with zero entropy, all the embedding vectors $\mathbf{x}_t$ should output the same permutation, which is possible only if the dynamics is a period-1 cycle, otherwise the embedding vectors will output different permutations so that the entropy of the whole dynamics is different from zero. For example, let us consider a period-5 cycle orbit obtained by generating 5 distinct random numbers $(0.8147, 0.9058, 0.1270, 0.9134, 0.6324)$ and repeating this basic sequence M-times ($M > 2$). The first four 6-order permutations obtained by sorting values of vectors $\mathbf{x}_t$, t=0 to 3, are the following:

$$\begin{cases} P_0 = \left(\frac{1,2,3,4,5,6}{3,5,1,6,2,4}\right); \\ P_1 = \left(\frac{1,2,3,4,5,6}{2,4,5,1,6,3}\right); \\ P_2 = \left(\frac{1,2,3,4,5,6}{1,6,3,4,5,2}\right); \\ P_3 = \left(\frac{1,2,3,4,5,6}{5,2,3,4,1,6}\right). \end{cases} \tag{2.2.3}$$

This example shows that the entropy related to the permutation (PE) is different from zero as there are at least four different permutations, although the dynamics is regular. It appears that the permutations are sensitive to the initial phase (or initial condition), and therefore cannot efficiently help for recognizing periodic dynamics as regular.

2.2.2 Usefulness of the permutations slopes

Definition 2.2.1. Viewing the permutation P_k as a piece-wise linear interpolation function, we simply consider as slope of each linear interpolation function the difference $s_i = P_k(i+1) - P_k(i)$, $1 \leq i \leq n-1$, between pairs of neighboring values in P_k. For a permutation P_k of order n, the maximum number of distinct slopes is $n-1$. We define the largest slope S_k of P_k as

$$S_k = \max\left(s_i,\, 1 \leq i \leq n-1\right), \tag{2.2.4}$$

We showed that $L = \lim_{n\to\infty} |S_k|$ for regular dynamics [26, 27].

If P_k includes some increasing pieces, then the largest slope is positive; otherwise, we note that the largest slope is equal to -1. Thus, there are n possible values of largest slope which all belong to the set $\mathcal{S}_p = \{-1,\, 1,\, 2, \ldots,\, n-1\}$ of largest slopes.

Theorem 2.2.1 (see [28])**.** *All the Permutations of length n generated using ascending order of the values of embedding vectors $\mathbf{x}_k$ of length n derived from a period-L time series $\{x_t\}$, $L = q$, $\tau_0 = 1$ and $n > \frac{L}{\gcd(L,\tau)}$, have the same largest slope $S = \frac{L}{\gcd(L,\tau)}$, where τ is the delay time of samples.*

Proof. Each $\mathbf{x}_k = (x_k, x_{k+\tau}, \cdots, x_{k+m\tau}, \cdots, x_{k+(n-1)\tau})$ corresponds to permutation P_k of order n after sorting into ascending order. Extracting samples from a periodic time series with a fixed step leads to another periodic sequence. We recall that L and q are respectively the phase space and time space periods.

If $\gcd(L,\tau) = 1$ and $n \leq L$, all the differences $P_k(i+1) - P_k(i)$, $i = 1$ to $n-1$ can take any value in $\mathcal{S}_p$, depending on the ordering of samples in $\mathbf{x}_k$, hence $S < L$.

If $\gcd(L,\tau) \neq 1$, then $x_{k+k'}{=}x_{k+k'+L}$ where $k' = m\tau$, $0 \leq m \leq n-1$. The corresponding indices in $\mathbf{x}_k$ are respectively $m+1$ and $m+1+\delta$ with $\delta = \frac{L}{\gcd(L,\tau)}$. The possible number of distinct samples in $\mathbf{x}_k$ is equal to δ: $\mathbf{x}_k$ is δ-periodic. In the case $n \leq \delta$, none of the L distinct values of $\{x_t\}$ is repeated in $\mathbf{x}_k$ and the largest slope takes any value $S < \delta$ in $\mathcal{S}_p$, depending on the ordering of samples in $\mathbf{x}_k$. If $n > \delta$, at least one of the possible δ distinct samples in $\mathbf{x}_k$ is repeated at least once. In that case, x_k for example is always repeated and each of its occurrences indicates the end of the previous period or the beginning of the next one. The time index of such occurrences in $\{x_t\}$ is $k + \alpha\tau$, α being an integer such that

$\alpha \geq \delta$. As $\mathbf{x}_k$ is δ-periodic, the index α indicating the repetition of $x_{k+m\tau}$, $0 \leq m \leq n-1$, is such that:

$$\alpha \equiv m \mod \delta. \tag{2.2.5}$$

The general solution of Eq.(2.2.5) is $\alpha(\kappa) = \kappa \cdot \delta + m$, where $\kappa \geq 0$ is the repetition index. From the definition of $\mathbf{x}_k$, the largest slope S is equal to the distance between indices of successive occurrences of the same value, so $S = \alpha(\kappa+1) - \alpha(\kappa) = \delta$. Thus, considering the definition of δ, the largest slope is:

$$S = \frac{L}{\gcd(L,\tau)}, \tag{2.2.6}$$

which ends the proof.

□

For example the largest slopes of the 6-order permutations P_0, P_1, P_2 and P_3 in Eq. (2.2.3) are $S_0 = S_1 = S_2 = S_3 = 5$. Each of the corresponding four vectors $\mathbf{x}_k$, $k = 0$ to 3, contains the same values and differ only by their ordering. All of them are then period-5 sequences.

Remark 2.2.1. Theorem 2.2.1 shows that the estimate of the phase space period of the time series $\{x_t\}$ by the largest slope S depends on the delay time τ. For this estimate to be equal to L, it is necessary that $\gcd(L,\tau) = 1$. As it is difficult to meet such a condition for arbitrary time series, choosing $\tau = 1$ is sufficient.

In the case of the PE for example, choosing $\tau > 1$ can lead to some misinterpretations in complexity values in the case of regular dynamics. Indeed, let us consider a 3-periodic and a 10-periodic time series. Normally, the first dynamics is less complex than the second one, but choosing $\tau = 5$ will reduce the second dynamics into a 2-periodic one, thus leading to a smaller complexity. For $n = 7$, the corresponding PE are respectively $H_1(7) = \ln(3) = 1.0986$ and $H_2(7) = \ln(10) = 2.3026$ for $\tau = 1$; and $H_1(7) = \ln(3) = 1.0986$ and $H_2(7) = \ln(2) = 0.6931$ for $\tau = 5$. It therefore turns out that the PE is such that $\ln(\delta) \leq H_p(n) \leq \ln(L)$. This dependence on the ordering of the time series proves that the bias between the PE and the largest Lyapunov exponent in the case of regular dynamics cannot be determined rigorously.

However, although choosing $\tau > 1$ can lead to false results for the detection of regular dynamics periods, it can be useful for detecting regular dynamics of large period from small

embedding dimensions ($n < L$). Indeed, if τ is such that $\gcd(L, \tau) > 1$, then the period of the time series is reduced to $\delta < L$ and choosing $\delta < n < L$ even allows to detect the dynamics as periodic.

Theorem 2.2.2 (see [28]). *Given a period-L time series $\{x_t\}$, $L = q$, and τ such that $\gcd(L, \tau) = 1$, the number of distinct permutations of length $n > L$, generated from the ascending sorting of the values of embedding vectors $\mathbf{x}_k$, $\mathbf{x}_{k+1}$, $\cdots$, $\mathbf{x}_{k+l}$, $\tau_0 < n$, is equal to $\frac{L}{\gcd(L,\tau_0)}$, where τ_0 is the delay time of the embedding vectors.*

Proof. If $\tau_0 = 1$, $\mathbf{x}_k$ and $\mathbf{x}_{k+L}$ according to Theorem 2.2.1 are repeats: $\{\mathbf{x}_k\}$ is L-periodic. It then results that P_k and P_{k+L} are the same, and only P_k to P_{k+L-1} are distinct permutations. So, the set of permutations in that case is L-periodic like the time series $\{x_t\}$.

If $\tau_0 > 1$ and $\frac{L}{\gcd(L,\tau_0)} = \gamma$, then by Theorem 2.2.1, it is easily verified that $\mathbf{x}_k$ and $\mathbf{x}_{k+\gamma}$ are redundant as $\{x_t\}$ is L-periodic. So, the number of distinct permutations obtained from $\{\mathbf{x}_k\}$ is equal to γ: $\{P_k\}$ is thus γ-periodic.

For $\gcd(L, \tau) > 1$, the number of distinct permutations can be smaller than γ, depending on the ordering of the values in $\{x_t\}$: the choice of τ can reduce the number of distinct permutations. Thus, γ is the maximum number of distinct permutations which can be obtained, given the couple (τ, τ_0), which ends the proof.

□

Example 2.2.1. *Let us consider for example $\{x_t\} = \{a_0, a_1, a_2, a_3, a_0, a_1, a_2, a_3, a_0, \cdots\}$, a 4-periodic ($L = 4$) time series, where $a_0 \neq a_1 \neq a_2 \neq a_3$ are distinct real numbers and an embedding dimension $n = 5$. For $\tau = 1$ and $\tau_0 = 1$, the corresponding embedding vectors are: $\mathbf{x}_0 = (a_0, a_1, a_2, a_3, a_0)$, $\mathbf{x}_1 = (a_1, a_2, a_3, a_0, a_1)$, $\mathbf{x}_2 = (a_2, a_3, a_0, a_1, a_2)$, $\mathbf{x}_3 = (a_3, a_0, a_1, a_2, a_3)$, $\mathbf{x}_4 = \mathbf{x}_0$, $\mathbf{x}_5 = \mathbf{x_1}, \ldots$, $\mathbf{x}_k = \mathbf{x}_{k-4}$, $k \geq 4$. In this example, there are only four distinct embedding vectors, so only four distinct permutations can be observed ($\gamma = \frac{L}{\gcd(L,\tau_0)} = 4$) and all of them have the same largest slope equal to the period of the time series, $S = L = \frac{L}{\gcd(L,\tau)} = 4$.*

Now let us consider $\tau = 2$ and $\tau_0 = 1$, the embedding vectors become: $\mathbf{x_0} = (a_0, a_2, a_0, a_2, a_0)$, $\mathbf{x}_1 = (a_1, a_3, a_1, a_3, a_1)$, $\mathbf{x}_2 = (a_2, a_0, a_2, a_0, a_2)$, $\mathbf{x}_3 = (a_3, a_1, a_3, a_1, a_3)$, $\mathbf{x_4} = \mathbf{x_0}$, $\mathbf{x}_5 = \mathbf{x}_1, \ldots$, $\mathbf{x}_k = \mathbf{x}_{k-4}$, $k \geq 4$. Once more, the number of distinct embedding vectors is equal to 4; but the number of distinct permutations depends on the ordering of the samples in

the time series. For the case $a_0 < a_2 < a_3 < a_1$, there are only two distinct permutations: $P_0 = P_3 = \left(\frac{1,2,3,4,5}{1,3,5,2,4}\right)$ and $P_1 = P_2 \left(\frac{1,2,3,4,5}{2,4,1,3,5}\right)$; this number of permutations is less than $\gamma = \frac{L}{\gcd(L,\tau_0)} = 4$ permutations. However, the largest slope of the permutations now is half the period of the time series, $S = \frac{L}{\gcd(L,\tau)} = 2$.

By setting $\tau = 1$ and $\tau_0 = 2$, the embedding vectors are: $\mathbf{x_0} = (a_0, a_1, a_2, a_3, a_0)$, $\mathbf{x}_2 = (a_2, a_3, a_0, a_1, a_2)$, $\mathbf{x}_4 = \mathbf{x}_0$, $\mathbf{x}_6 = \mathbf{x}_2, \ldots, \mathbf{x}_{2k} = \mathbf{x}_{2k-4}$, $k \geq 2$. It then turns out that the maximum number of distinct permutations is now half the period of the time series: $\gamma = \frac{L}{\gcd(L,\tau_0)} = 2$; while the largest slope of these permutations remains $S = L = 4$

Finally, if $\tau = 2$ and $\tau_0 = 2$, the embedding vectors are: $\mathbf{x}_0 = (a_0, a_2, a_0, a_2, a_0)$, $\mathbf{x}_2 = (a_2, a_0, a_2, a_0, a_2)$, $\mathbf{x_4} = \mathbf{x_0}$, $\mathbf{x}_6 = \mathbf{x_2}, \ldots, \mathbf{x}_{2k} = \mathbf{x}_{2k-4}$, $k \geq 2$. It is now clear that both the number of permutations and the largest slopes are reduced to half the period of the time series. This example can be extended to any period to see the interplay between τ and τ_0

Remark 2.2.2. Theorem 2.2.2 shows that only γ ($\gamma \leq L < n$) permutations are periodically repeated in the case of regular dynamics, instead of $n!$. This number is less than or equal to the possible number of largest slopes, so the permutations can be efficiently represented by their largest slopes with no information loss. In addition, for a given regular dynamics, all the γ permutations have the same largest slope.

On the contrary, for non-regular dynamics if the period L is assumed to be infinitely large, then $n < L$ implies that the number of distinct permutations is greater than n. Therefore the permutations cannot be efficiently described by the n possible values of largest slopes any more. It then turns out that for a given dynamics, there is more than a single value of largest slope as in the case of regular dynamics.

From the remark 2.2.2, we can conclude that regular dynamics can be characterized by a single largest slope whereas non-regular dynamics cannot. This difference can help to distinguish between the two types of dynamics. The largest slopes do not allow to represent all the possible permutations in the case of non-regular dynamics and therefore are not useful for estimating their complexity.

Remark 2.2.3. Theorem 2.2.2 shows that the number of distinct permutations is less than or equal to L and that $\{P_k\}$ is γ-periodic. It thus implies that there is no need to consider large observation durations, as the periodicity of the permutations can be detected from only three to four cycles. So, the effective observation time can be set such that $3n \leq T \leq 4n$,

with $n > L_m$ the largest period to be estimated without error. This observation also implies that only 3γ to 4γ permutations can be sufficient for the detection to be accurate. When τ_0 is chosen such that $\gcd(L, \tau_0) > 1$, 4γ can be too small and allows to save computation time. Indeed, considering the largest slope does not allow us to determine the complexity, but only to distinguish between regular and non-regular dynamics. So, it is not useful any more to consider $T \gg n!$, but only $T > 3n$. This observation is important as it can help speed up the detection of the regularity of dynamics for real-time applications, and to make a clear decision from a small amount of data. For low-dimensional systems for example, where periodic dynamics have few number of harmonics, large values of n are not required.

Remark 2.2.4. In the case $L = q$ and $n < L$, the set $\{S_k\}$ of largest slopes derived from $\{\mathbf{x}_k\}$ is γ-periodic. Indeed, for any embedding dimension $n < L$, the embedding vectors $\mathbf{x}_k$ are periodically repeated as the time series $\{x_t\}$ is L-periodic, even if the largest slopes of the corresponding permutations P_k take possible values between 1 and $n-1$, depending on the ordering of the values in $\{x_t\}$. Theorem 2.2.2 shows that embedding vectors $\mathbf{x}_k$ are periodically repeat, and only a maximum of γ distinct permutations P_k can be derived from such embedding vectors. The number of distinct permutations for a regular dynamics does not explicitly depend on the embedding dimension, but only on L, τ_0, T and the ordering of the values. As stated above, the time period of $\{S_k\}$ is equal to γ, similar to that of $\{\mathbf{x}_k\}$, except when all the S_k values are the same. When $\{S_k\}$ corresponds to a period-1 cycle time series. As only a maximum of γ distinct permutations can be derived from the set of embedding vectors $\mathbf{x}_k$, although the corresponding largest slopes may be different, it can be conjectured that the upper limit of the PE of a L-periodic dynamics is $\ln(\gamma)$, where $\gamma = \frac{L}{\gcd(L,\tau_0)}$. This limiting value is obtained when all the γ permutations are realized with the same probability. The dependence of the number of distinct permutations on the ordering of values in $\{x_t\}$ and τ can lead to arbitrary nonzero values of the PE for regular dynamics: two regular dynamics with the same period can give different permutation entropies.

Remark 2.2.5. In the case $L < q$, repeated values occur in the basic period of $\{x_t\}$. For the largest slope to be unique and equal to q, at least one non-repeated value should appear twice in $\mathbf{x}_k$. For avoiding any detection error, it is necessary to consider the time period as it remains constant even for embedding vectors with repeated values in the basic period

($L < q$). This requirement can be easily justified by considering $n \geq 2q$ as embedding dimension. For example, $n = 200$ is enough for detecting dynamics with period $q = 100$. When there is no redundant value, even a period $q = 199$ can be efficiently detected with $n = 200$.

2.2.3 Permutation largest slope entropy

Theorems 2.2.1 and 2.2.2 indicate that L-periodic dynamics are characterized by a single value of largest slope if the embedding dimension is such that $L < n$. It turns out that the entropy related to the distribution of the largest slopes is equal to zero in the case of regular dynamics, thus ideal for detecting it, unlike the PE which can take arbitrary values. Thus, we define the *permutation largest slope entropy* (PLSE) of order $n \geq 2$, $\tau_0 = \tau = 1$, as:

$$H_S(n) = -\sum p(S) \ln(p(S)) \tag{2.2.7}$$

where

$$p(S) = \frac{\#\{k \mid 0 \leq k \leq T - n, S_k = S\}}{T - n + 1} \tag{2.2.8}$$

is the probability, or relative frequency, of S and $\#$ denotes the cardinality. $H_S(n) = 0$ for regular dynamics with period $L < n$ and $0 < H_S \leq \ln(n)$ for non-regular dynamics. We can also define the normalized PLSE as:

$$h_S(n) = H_S(n)/\ln(n). \tag{2.2.9}$$

$h_S(n) = 0$ for regular dynamics and $0 < h_S(n) \leq 1$ for non-regular dynamics. Indeed, regular dynamics are characterized by a single value of largest slope $S_k = S$, for all k and $H_S = 0$ as $p(S) = 1$; for non-regular dynamics, S_k takes different values, thus leading to a nonzero entropy. By this approach, the PLSE can help to distinguish between regular and non-regular dynamics.

The definition of the entropy related to $\{S_k\}$ allows us to reduce redundant permutations in the case of regular dynamics: two permutations with the same largest slope are equivalent. The maximum number of permutations with different largest slopes is thus n instead of $n!$.

2.2.4 Relationship between the 3ST and the PLSE

We defined the 3ST algorithm for distinguishing between regular and non-regular dynamics. The difference between the PLSE and 3ST resides in the statistical analysis of the largest

slope. We first computed the periodicity index λ_{3ST} by considering embedding vectors of different lengths [26]. Thereafter, we studied the sensitivity of λ_{3ST} to the initial phase, namely λ_P, by considering embedding vectors of fixed length [27]. The interpretation of λ_P is similar to that of the PLSE: $\lambda_P = 0$ for regular dynamics and $\lambda_P > 0$ for non-regular dynamics. Computing the PLSE is similar to computing λ_P, except that the PLSE algorithm is easy to implement. Indeed, apart from the delay times τ and τ_0 which are common to the two algorithms, four parameters are required for the determination of λ_P, whereas only the permutation length n is useful for computing the PLSE $h_S(n)$. The lower number of parameters in the PLSE algorithm reduces the chance of detection errors due to inappropriate parameter settings.

The number of distinct permutations in the case of regular dynamics does not explicitly depend on the embedding dimension n. However, choosing $n < L$ may lead to permutations with different largest slopes, hence to $h_S > 0$ for regular dynamics. In order to prevent such false detection, large embedding dimensions are required. The value of n is then chosen such that $n > L_m$, where L_m is the largest period to be detected with no error. Periodic dynamics whose periods are greater than L_m are considered to be chaotic and the choice of L_m depends on the complexity of the system under study. Similarly to the 3ST algorithm, the DDQ can be applied to the PLSE for the noise reduction.

2.3 Influence of the parameter setting

For the analysis of the impact of the parameter setting on the PLSE result, we used the logistic map whose the control parameter r varies from 3.5 to 4 with a step size of $\Delta r = 10^{-3}$. We also compare the PLSE results to those of the PE.

2.3.1 Impact of τ and τ_0 on the PE and PLSE

The logistic map exhibits a period doubling bifurcation for $3.5 \leq r < 3.57$, starting with a period-4 cycle. The Feigenbaum diagram is given in Fig. 2.1(a) for comparison with entropy values in periodic windows. Fig. 2.1 shows that choosing $\tau > 1$ effectively reduces the PE of regular dynamics for which $\gcd(L, \tau) > 1$. The PE of period-4 and period-8 cycles which are respectively $\ln(4)$ and $\ln(8)$ for $\tau = 1$ are now all equal to zero for $\tau = 8$ and less than the PE of period-3 cycle which remains equal to $\ln(3)$ for both $\tau = 1$ and $\tau = 8$. The

same result is observed with the PLSE. For example, $r = 3.606$ corresponds to a period-20 cycle and the smallest embedding dimension for H_S to be zero is equal to 21. However, considering $\tau = 8$ brings back this period to 5, which is less than the embedding dimension $n = 7$, hence $H_S(7) = 0$ for this dynamics.

For $\tau_0 = 8$, the number of distinct permutations in the case of period-4 and 8 cycles is reduced to $\gamma = \frac{L}{\gcd(L,\tau_0)} = 1$, thus leading to $H_S(7) = 0$; for all other period-L cycles with L a multiple of 8, the number of distinct permutations becomes $\gamma = L/8$ instead of $\gamma = L$. This reduction of the number of permutations does not guarantee a zero value of the PLSE as $7 < L \leq 32$ may lead to different largest slopes. For the PLSE to be zero, the embedding dimension needs to be greater than the period of the underlying dynamics: τ_0 does not reduce the period of the orbit, but only the number of distinct permutations. Fig. 2.1 also shows that complexities corresponding to $\tau = 1$, $\tau_0 = 1$ and $\tau = 1$, $\tau_0 = 8$ are quite the same for non-regular dynamics, while for $\tau_0 = 1$ and $\tau > 1$ an increase of the complexities is observed. This observation confirms that $\tau_0 > 1$ preserves the ordering/nature of the underlying dynamics, hence its complexity, while $\tau > 1$ does not, thus giving a more complex appearance to the dynamics than truly exists: we have shown in Theorem 2.2.1 that $\tau > 1$ can lead to the reduction of the periods of regular dynamics while Theorem 2.2.2 has shown that only the number of distinct permutations can change without affecting the period of the dynamics. Considering the simulation results, we can conjecture that in the case of non-regular dynamics, choosing $1 < \tau_0 < n$ does not significantly modify the number of distinct permutations, hence the complexity measure of the dynamics. Considering $\tau_0 > n$ contributes to skipping samples in $\{x_t\}$ and may lead to false detection results. It also appears that choosing large values of τ is a limiting factor for the chaos scaling as the PE is taking about the same value for all the non-regular dynamics. On the other hand, choosing $\tau_0 > 1$ reduces the PE of regular dynamics for which $\gcd(L, \tau_0) > 1$, while maintaining the scaling of the complexity of non-regular dynamics. Fig. 2.1(b) and Fig. 2.1(c) show that $H_S(7) < H(7)$, which confirms that the number of distinct permutations in the case of non-regular dynamics is effectively greater than the number of possible slopes, and therefore cannot be suitably described by the largest slopes.

The impacts of τ and τ_0 on the PE and the PLSE for regular dynamics are quite opposed. For $\tau_0 = 1$, $\gcd(L, \tau) > 1$ contributes to reducing the period of the underlying dynamics to $\delta < L$, but does not change the number of distinct permutations. It therefore turns

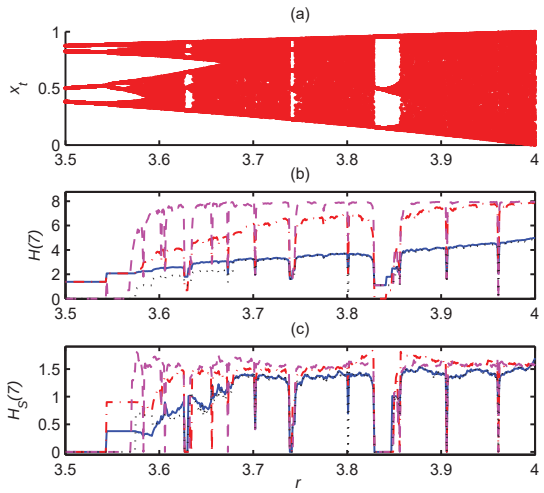

Figure 2.1: Logistic equation for varying control parameter $3.5 \leq r \leq 4$ (step $\Delta r = 10^{-3}$), $T = 5000$: (a) Bifurcation diagram, (b) PE $H(7)$ for $\tau = 1$ and $\tau_0 = 1$ (blue solid line), $\tau = 3$ and $\tau_0 = 1$ (red dash-dotted line), $\tau = 8$ and $\tau_0 = 1$ (magenta dashed line) and $\tau = 1$ and $\tau_0 = 8$ (black dotted line); (c) PLSE $H_S(7)$ for $\tau = 1$ and $\tau_0 = 1$ (blue solid line), $\tau = 3$ and $\tau_0 = 1$ (red dash-dotted line), $\tau = 8$ and $\tau_0 = 1$ (magenta dashed line) and $\tau = 1$ and $\tau_0 = 8$ (black dotted line).

out that the PLSE of regular dynamics with period L such that $\delta < n < L$ is equal to zero, while the corresponding PE is such that $\ln(\delta) \leq H(n) \leq \ln(L)$. In the case $\tau = 1$ and $\gcd(L, \tau_0) > 1$, the number of distinct permutations is reduced to $\gamma < L$, while the period L remains unchanged. As a consequence, the PE of L-periodic orbits is reduced to $H(n) \leq \ln(\gamma)$ whilst their PLSE is such that $0 \leq H_S(n) \leq \ln(n)$ if $n \leq L$ and $H_S = 0$ if $n > L$. We choose $n = 7$ in Fig. 2.1 for comparison purposes, but this value needs to be large enough for efficient detection of regular dynamics with large periods.

2.3.2 Impact of n on the detection result

Now let us consider $n = 1024$ with $\tau = 1$, $\tau_0 = 8$ and $n = 32$ with $\tau = 8$, $\tau_0 = 1$. Such large values of n are difficult to consider with the PE as the requirement $T \gg n!$ may be difficult to achieve in practice. In the simulation below, the results of the PLSE are compared with the Lyapunov exponent. From Fig. 2.2, choosing large values of n effectively allows us to give a better estimate of the periods and to measure zero entropy even for dynamics with large periods. This result also shows that there is no need to increase the observation time

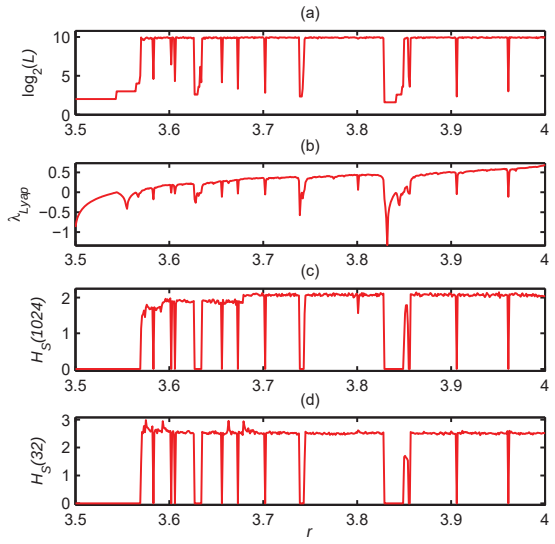

Figure 2.2: Logistic equation for varying control parameter $3.5 \leq r \leq 4$ (step $\Delta r = 10^{-3}$), $T = 5000$: (a) Cycle diagram for $\tau = 1$ and $\tau_0 = 8$; (b) Lyapunov exponent λ_{Lyap}; (c) $H_S(1024)$, $\tau = 1$ and $\tau_0 = 8$; (d) $H_S(32)$, $\tau = 8$ and $\tau_0 = 1$.

T, as only three to four cycles of the distinct permutations are required for the dynamics to be detected as periodic. Choosing $\tau_0 = 8$ allows us to reduce the number of permutations for all regular dynamics whose periods are such that $\gcd(L, \tau_0) > 1$ and to reduce the computational time, while choosing $\tau = 8$ allows to achieve zero PLSE even for period-L cycle dynamics with $L > 32$ and $\delta < 32 < L$. For $r = 3.602$ for example, the logistic map exhibits a period-88 cycle dynamics and considering $n = 32$ is not enough for detecting this dynamics as periodic. However, combining $n = 32$ with $\tau = 8$ allows to obtain $H_S(32) = 0$ as the 88-periodic orbit is reduced to period-δ cycle dynamics, with $\delta = 11$. Normally, there is a tiny periodic window around $r = 3.801$ which cannot be clearly observed as $\Delta r = 0.001$ only. For $r = 3.801$ the LE is coming close to zero ($\lambda_{Lyap} = 0.0619$), but remains positive. This result is clearly expressed by the PLSE which remains positive even for $n = 1024$ ($H_S(1024) = 1.5652$), thus confirming the chaotic nature of the corresponding dynamics.

2.4 Applicability to continuous time systems

Similarly to the 3ST, applying the PE or the PLSE to continuous time series is quite difficult due to the sampling process and the precision of the integrator. Thus, the time series should be considered as noise contaminated. For the PLSE to be efficiently determined, we used the DDQ as for the 3ST for noise reduction. We thus used as dynamical system the forced Duffing oscillator described in Eq. (1.6.2). The PLSE algorithm is then applied to the solutions x_t and y_t and only the maximal value of the corresponding entropies is retained. As in chapter 1, we considered in the case of PLSE and 3ST that the time series $\{x_t\}$ and $\{y_t\}$ are corrupted by a small amount of noise of amplitude $\varepsilon \leq T_s/10$, due to sampling and numerical integration. Taking $\eta = T_s/10$ and applying the DDQ to $\{x_t\}$ and $\{y_t\}$, we obtained the result in Fig. 2.3(b), which is to be compared to λ_P in Fig. 2.3(c) computed in chapter 1. Applying the DDQ prior to PE gives approximately the same result as in Fig. 2.3(d), for which no noise reduction is considered. The results in Fig. 2.3 show that the LE λ_{Lyap} and $h_S(n)$ behave similarly, except for $r = 0.287$ where $h_S(n) > 0$ indicates a transition between two stable limit-cycles. This transition is characterized by the detection of two values of largest slopes and can be easily recognized. Fig. 2.3(d) shows that PE can only detect changes in the dynamics, but cannot give details on their nature. The PLSE algorithm may also be applied to the set of local maxima of $\{x_t\}$ and $\{y_t\}$ to obtain effectively the same detection result.

So, according to the observation made on the impact of τ and τ_0, PE accurately estimates the complexity of L-periodic dynamics iff the conditions $\gcd(L, \tau) = 1$ and $\gcd(L, \tau_0) = 1$ are satisfied. As there is no defined period in the case of non-regular dynamics, such a condition is not required and the PE approximates the complexity of the underlying dynamics better when $\tau_0 < n$. In contrast, the PLSE always indicates a zero complexity for the regular dynamics whose periods are such that $L < n$, as they are perfectly predictable. In the case of non-regular dynamics, the maximum number of distinct permutations is greater than the n possible values of largest slopes, and the permutations therefore cannot be effectively described by their largest slopes. Consequently, the corresponding entropy cannot be considered as a complexity measure. However, as nonzero entropies are supposed to be obtained only for non-regular dynamics and zero entropies for regular dynamics, the PLSE can be considered to be a detection entropy. Choosing $\tau > 1$ allows to reduce

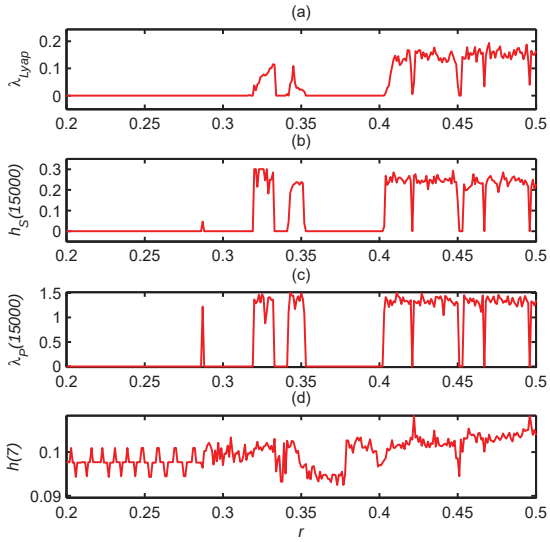

Figure 2.3: Forced Duffing System for varying control parameter $0.2 \leq r < 0.5$ (step $\Delta r = 10^{-3}$), $T = 4 \cdot 10^4$: (a) Lyapunov exponent, (b) $h_S(15000)$, (c) $\lambda_P(15000)$ and (d) $h(7)$.

detection errors due to small values of embedding dimensions n while $1 < \tau_0 < n$ allows to consider smaller observation time T for detection purposes. Moreover, choosing $1 < \tau_0 < n$ speeds up the scanning time of the time series under study, hence the PLSE algorithm, as the number of embedding vectors analyzed for $\tau_0 = 1$ is reduced by a factor of τ_0 without error on the detection result. For the purposes of detection, the above results show that the PLSE behaves similarly to the positive Lyapunov exponent, whilst outputting zero entropy for regular dynamics without bias. Compared to λ_P, the calibration of the PLSE algorithm is easier than that of the 3ST algorithm.

We also applied the PLSE algorithm to experimental data acquired from an electronic circuit exhibiting a Duffing attractor in order to validate its effectiveness and robustness against noise [24]. We compared the results obtained to those of the 0-1 test, the conditional entropy of ordinal patterns (CPE) and the maximal Lyapunov exponent (MLE). From the comparison of the experimental spectra of the four methods with the analogue phase portraits of the experimental system, it appeared that the PLSE is the more reliable algorithm for chaos detection from experimental data.

2.5 Applicability to strange nonchaotic attractors (SNA)

Strange nonchaotic attractors (SNA) are usually observed in quasi-periodically forced nonlinear systems. The general term for such systems in the case of one-dimensional maps is given by

$$\begin{cases} x_{t+1} = f(x_t, 2\pi y_t) \\ y_{t+1} = y_t + \Omega \mod 1, \end{cases} \tag{2.5.1}$$

where $\Omega = (-1 + \sqrt{5})/2$. SNA are geometrically strange (i.e described by a fractal dimension), but the corresponding nontrivial largest Lyapunov exponent is negative, thus implying a nonchaotic dynamics. They were only seen in laboratory experiments, but never in the nature until the recent observation of stellar strange nonchaotic dynamics [49]. This observation of course could imply an increasing interest for SNA detection in the forthcoming years, as it may improve the classification and refine the physical modeling of the stars' interiors [49, 61].

Although the PLSE like the 3ST can detect periodic and quasi-periodic dynamics [27, 28], it should be noticed that this detection can require a long observation time, depending on the period of the time series. In the case of quasi-periodically forced dynamics, the time series period may be too long as compared to the observation time. In these cases, the detection of the corresponding tori and SNA is no longer possible. For the PLSE to be efficient in such cases, some preprocessing or transform must be applied to the initial time series. In this section, we suggest applying the PLSE algorithm to quantized ordinal matrices (QOM) derived from the input time series [23].

In fact, we observed that there is no possibility of detecting quasi-periodic dynamics as regular while considering the phase space periodicity. Indeed, given the irrational nature of the driving frequency, observing some repetition of a certain basic shape is somehow impossible. However, while considering the order relation between the time series values, we observed that some periodicity properties may occur in the resulting data series. For this purpose, we suggest using the order relation between values in the time series as a quantizer (ordinal quantizer), so as to reduce the number of distinct values in the initial time series, and hence its complexity which is due to the numerical approximation of the irrational driving frequency. With this approach, the periodicity related to the order relation can

then be exploited for detecting torii and SNA as regular dynamics.

2.5.1 Ordinal quantization of the time series

The principle of the ordinal quantization process is described in what follows. Given the time series $\{x_t\}_{t=0,\cdots,T-1}$, we first choose the embedding dimension k, and consider embedding vectors $\mathbf{x}_k = (x_k, x_{k+1}, \ldots, x_{k+j}, \ldots, x_{k+(l-1)})$, where $j+1$ is the index of x_{k+j} in $\mathbf{x}_k$, $j \in \mathbb{N}$. Thereafter, permutations P_k of order l are derived from embedding vectors $\mathbf{x}_k$ by sorting the amplitude of the elements of each $\mathbf{x}_k$ into ascending order. The possible number of distinct permutations is $l!$ and depends on the time series under study. This value may be greater or less than the initial number L of distinct values in the time series. Finally, the largest slope S_k, $k = 0, 1, \cdots, T-l+1$, of each permutation P_k derived as in Eq. (2.2.4) is considered as the quantized value. The ordinal quantization thus defined allows us to convert the phase space period L of the initial time series into l: $S_k \in \{-1, 1, 2, \cdots, l-1\}$. Choosing $l = 2$ for example is equivalent to the ordinal binarization of the time series, as only two distinct values are allowed, namely $S_k \in \{-1, 1\}$. Indeed, reducing the phase space period is required for the detection of regular dynamics with large period L. Since the quantization process may introduce repetitions in the quantized time series, some hidden periods may appear, thus helping to characterize complex regular dynamics.

2.5.2 Ordinal matrix transform of the quantized time series

While quantizing the initial time series, some properties are lost. Therefore, even weakly chaotic dynamics may be detected with a zero entropy. In order to avoid such errors, we propose increasing the complexity of the quantized time series by transforming it into a series of ordinal matrices of order m. The principle consists of combining m symbols of the previously quantized series $\{S_k\}$ into a single value such that:

$$z_{t_1} = \frac{1}{\sum_{i=1}^{m} a^{-\frac{i}{i+1}}} \cdot \sum_{i=1}^{m} a^{-\frac{i}{i+1}} S_{t_1+i-1}, \tag{2.5.2}$$

with $t_1 = 0, 1, \ldots, T-(l+m)+2$, $a = 2$. Given that S_{t_1} corresponds to the quantized value of the embedding vector $\mathbf{x}_{t_1}$, combining m values of S_{t_1} is equivalent to designing $l \times m$ matrices whose quantized value is z_{t_1}. $\{z_{t_1}\}$ is the quantized series of embedded delayed matrices (QOM) derived from the series $\{x_t\}$, or embedded quantized vectors derived from

the series $\{S_k\}$ of quantized ordinal patterns (permutations), which itself is derived from $\{x_t\}$ using ordinal relations. The whole process can be summarized as follows:

$$\begin{pmatrix} x_{t_1} & x_{t_1+1} & \cdots & x_{t_1+l-1} \\ x_{t_1+1} & x_{t_1+2} & \cdots & x_{t_1+l} \\ \vdots & \vdots & \vdots & \vdots \\ x_{t_1+j} & x_{t_1+j+1} & \cdots & x_{t_1+l+j-1} \\ \vdots & \vdots & \vdots & \vdots \\ x_{t_1+m-2} & x_{t_1+m-1} & \cdots & x_{t_1+l+m-3} \\ x_{t_1+m-1} & x_{t_1+m} & \cdots & x_{t_1+l+m-2} \end{pmatrix} \longrightarrow \begin{pmatrix} S_{t_1} \\ S_{t_1+1} \\ \vdots \\ S_{t_1+j} \\ \vdots \\ S_{t_1+m-2} \\ S_{t_1+m-1} \end{pmatrix} \longrightarrow z_{t_1}$$

So, each line $j = 0, 1, \ldots, m-1$ of the matrix corresponds to the embedding vector $\mathbf{x}_{t_1+j}$ and is transformed into a single scalar S_{t_1+j} corresponding to the largest slope of the permutation obtained by sorting its values. Given an initial time series $\{x_t\}$ of length T, a quantized series $\{S_{t_1}\}$ of embedding vectors of length l, whose the length is $T-l+1$, can be derived. Even if the number of distinct values in $\{x_t\}$ is unknown, the possible number of distinct values in $\{S_{t_1}\}$ is equal to l. Combining m values of $\{S_{t_1}\}$ to define the series $\{z_{t_1}\}$ allows to generate new words, thus to increase the number of distinct values from l to l^m. By this approach, a small difference between two quantized series of permutations is amplified so that the PLSE values of the corresponding transformed time series are no longer the same.

Let us consider for example a period-5 cycle ($L = 5$) time series obtained by generating 5 distinct random numbers $(0.8147, 0.9058, 0.1270, 0.9134, 0.6324)$ and repeating this basic shape 200-times. Similarly, using the circle map defined in Eq. (1.2.2) with $r = 0$ and $\Omega = \frac{-1+\sqrt{5}}{2}$, let us generate a quasi-periodic time series. The first 100 values of the corresponding time series as well as the corresponding binarized time series are shown in Fig. 2.4(a)-(b). For the period-5 time series, the phase space period is decreased from $L = 5$ to $L_1 = 2$. However, for the binarized time series to be detected as regular, an embedding dimension $n \geq 8$ is required for the PLSE algorithm, while only $n = 6$ would have been necessary for the initial time series. It should be pointed out that the time period of the binarized series remains $q = 5$ as for the initial time series. This increase of the PLSE embedding dimension is due to repetitions introduced by the quantization process. In the quasi-periodic dynamics all the 1000 samples generated with $x_0 = 0.25$ are distinct and no

phase and time period can be determined. However, the binarization process converts this dynamics into a period-2 time series, while some time periods can be observed on short sequences ($q = 8$, $q = 13$, $q = 21$,...). We observed that an embedding dimension $n = 8$ is enough for the PLSE to output zero, whereas no precise small embedding dimension can be initially estimated theoretically. The binarization process thus reduces the complexity of the quasi-periodic dynamics by highlighting some hidden periods. Indeed, we verified that repeating patterns of length q can be extracted from the binarized series derived from the quasi-periodic dynamics and that the values of q belong to the Fibonacci sequence. Depending on the initial condition, some Fibonacci numbers may not occur on the sequence of hidden periods $\mathrm{G}_q = \{q_j\}$. For our example, the sequences of the first 8 hidden periods obtained for $x_0 = 0.25$ and $x_0 = 0.251$ are respectively $\mathrm{G}_q^1 = \{5, 8, 13, 21, 89, 144, 233, 377\}$ and $\mathrm{G}_q^2 = \{5, 8, 13, 21, 89, 144, 610, 987\}$. By using the binarization, two distinct quasi-periodic dynamics generated with slightly different initial conditions can then be characterized by their respective signatures G_q^1 and G_q^2. In the case of periodic dynamics of period q, the signature does not depend on the initial condition and behaves linearly, i.e $q_j = j \cdot q$. So, from these examples, it is clear that the phase space period of the quantized time series is smaller than that of the initial time series. However, the embedding dimension required for the PLSE to output a zero entropy may be slightly increased as repetitions appear in the quantized series. In the case of quasi-periodic dynamics, in addition to the phase space period, a variable time space period clearly appears, whereas no pattern can be observed in the initial time series, thus attesting that its complexity is reduced.

Applying the ordinal matrix transform with $m = 3$ to the above quantized series leads to new time series as shown in Fig. 2.4(c). The maximum number of distinct values is equal to $l^m = 8$. For the period-5 data series, the phase period is increased from $L = 2$ to $L = 4$, while the time period remains $q = 5$ with one repeated value. The PLSE thus outputs a zero value for this time series when considering an embedding dimension $n \geq 7$. For the quasi-periodic time series, the new phase period is also $L = 4$, while the time period sequences are now $\mathrm{G}_q^1 = \{13, 21, 89, 144, 233, 377, 1597, 2584, \ldots\}$ and $\mathrm{G}_q^2 = \{13, 21, 89, 144, 610, 987, 1597, 6765, \ldots\}$ respectively for $x_0 = 0.25$ and $x_0 = 0.251$. The PLSE now requires $n \geq 21$ as embedding dimension for the time series to be detected as regular. It is observed from the period sequences that the shorter periods 5 and 8 do not appear anymore. This observation implies that the series of QOM are more complex than

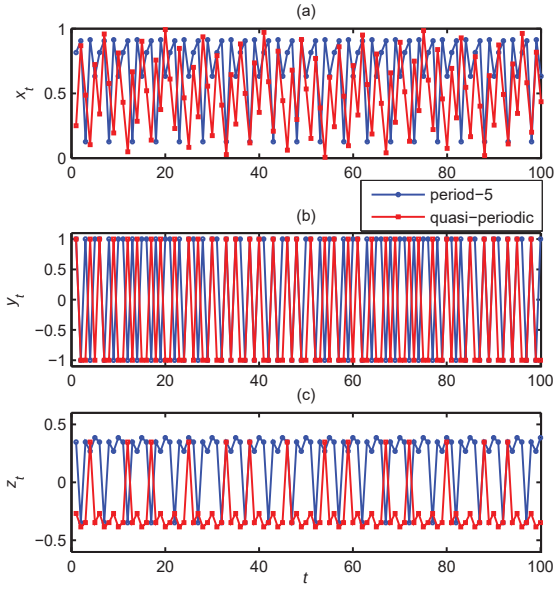

Figure 2.4: Example of ordinal matrix transform: (a) initial time series, (b) series of permutations largest slopes and (c) quantized ordinal matrices time series

the generating binarized series, thus requiring a larger embedding dimension for the PLSE. The embedding dimension n required for the series of QOM to be detected as regular is increased accordingly to the initial phase space period (or complexity) of the corresponding time series. Assuming that quasi-periodic dynamics are less complex than SNA which themselves are less complex than chaotic dynamics, the present ordinal matrix transform is used for detecting SNA.

2.5.3 Efficiency of the ordinal matrix transform

Applying the PLSE to the series of ordinal matrices requires three parameters n, l and m. As the detection result is sensitive to all these parameters, some guidance for their choice is necessary. Indeed, the ordinal matrix transform preserves the time period of periodic dynamics, although the phase space period is modified by the quantization process.

SNA, Quasi-periodic and chaotic dynamics all present large phase space periods. The phase space period is reduced by the ordinal matrix transform, but unlike for the quasi-periodic dynamics, the PLSE outputs a nonzero entropy for both SNA and chaotic dynamics. The nonzero value of the PLSE thus obtained implies that the transform induces no time

period, or the induced time period is too large. Indeed, even when a time period exists, the number of repeated values increases as the difference between l and the initial phase space L becomes larger ($l < L$); and the required embedding dimension for the PLSE to output zero increases with the number of repeated values. Given that chaotic dynamics are assumed to be more complex than SNA, the complexity of the ordinal matrix series obtained from a chaotic dynamics should increase faster than that of the SNA data series. Under this assumption, (for a given dynamical system) a pair (l, m) may exist such that the entropy of the series of ordinal matrices of the SNA is smaller than that of the series of ordinal matrices of the chaotic dynamics, whereas the initial time series of the two dynamics present approximately the same entropy.

Let $h(n)$ be the entropy of the series of ordinal matrices $\{z_t\}$ and $h_0(n)$ the entropy of the initial time series $\{x_t\}$, we thus define an indicator for the calibration of the parameters n, l and m as follows:

$$\lambda_{l,m}(n) = \begin{cases} \ln\left[\frac{h_0(n)-1}{h(n)-1}\right], & \text{if } h > h_0; \\ \\ \ln\left[\frac{h(n)}{h_0(n)+\xi} + \xi\right], & \text{if } h \leq h_0. \end{cases} \tag{2.5.3}$$

with $0 < \xi \ll 1$. In our examples, we set $\xi = 10^{-2}$ for this equation. The algorithm is assumed to be well calibrated if for a given value of n, $h(n) > h_0(n)$ only for chaotic dynamics. This implies that $\lambda_{l,m} \leq 0$ for periodic and quasi-periodic dynamics as well as tori and SNA for well chosen values of k and m. This condition constitutes our criterion for the choice of (l, m) pairs. Given that quasi-periodic dynamics are assumed to present a zero entropy, the corresponding values of $\lambda_{l,m}$ should be less than those of SNA. The above definition of $\lambda_{l,m}$ constitutes the extension of the PLSE algorithm for SNA detection. In order to evaluate the efficiency of the ordinal matrix transform, let us apply the extended PLSE to the forced logistic and cubic maps. The forced logistic map is described by the following equation [54]:

$$x_{t+1} = r\Big[1 + \epsilon' \cos(2\pi y_t)\Big] x_t(1 - x_t) \tag{2.5.4}$$

with y_t behaving as in Eq.(2.5.1), $0 \leq r \leq 4$ and $0 \leq \epsilon' \leq \frac{4}{r-1}$. In order to ensure a bounded motion, the amplitude is rescaled as $\epsilon \to \frac{\epsilon'(r-1)}{4}$, with $0 \leq \epsilon \leq 1$. Similarly, the forced cubic

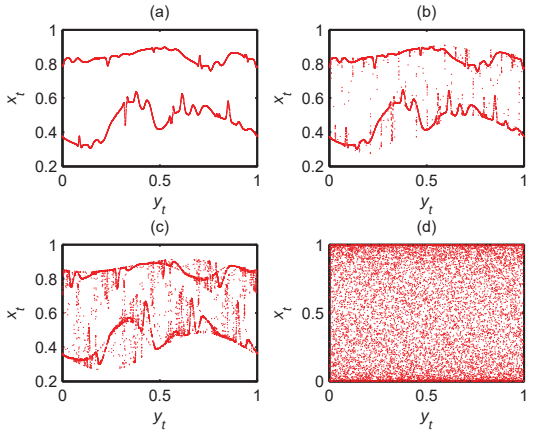

Figure 2.5: Example of phase portraits derived from the quasi-periodically forced logistic map. From left to right and from top to bottom: Torus ($r = 3.484$), SNA ($r = 3.488$), Weak-chaos ($r = 3.513$) and Chaos ($r = 4$). The dynamics are obtained with $\epsilon = 0.3$.

map is described by the following equation of motion [34]:

$$x_{t+1} = A\cos(2\pi y_t) - \beta x_t + x_t^3 \tag{2.5.5}$$

with y_t behaving as in Eq.(2.5.1).

Fig. 2.5 shows some an example of phase portraits for a torus, an SNA and a chaotic dynamics derived from the quasi-periodically forced logistic map. Although, SNA may be found both in $\lambda_{l,m} < 0$ and $\lambda_{l,m} > 0$ regions, the detection of tori-SNA transitions is expected to be improved in the $h(n)$-spectrum, compared to the Lyapunov exponent spectrum as can be seen in Fig. 2.6 where the extended PLSE is applied to the forced logistic map. For this example, the effectiveness of the parameter setting is evaluated by computing the rate σ of false detection of $\lambda_{l,m}$ for a large spectrum of the system under study, taking as reference the Lyapunov exponent λ_{Lyap}. This error is evaluated as

$$\sigma(\%) = \frac{\sum |\text{sign}(\lambda_{Lyap}) - \text{sign}(\lambda_{l,m})|}{2N} \times 100, \tag{2.5.6}$$

where N is the length of the spectrum. σ expresses how effective the parameter setting is. The smaller σ, the better the calibration of the parameters. We set for this experiment $2.4 \leq r \leq 4$ with step size $\Delta r = 10^{-4}$, $\epsilon = 0.3$, $n = 280$, $l = 4$, $m = 3$ and $T = 5 \cdot 10^4$ as data length. The corresponding calibration error is $\sigma = 3.387\%$, which is quite small, as compared to the total number of values analyzed.

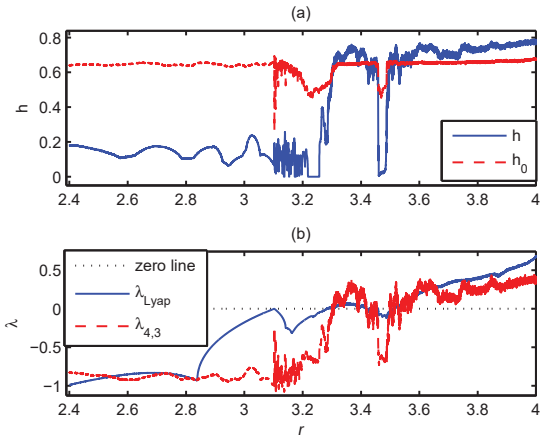

Figure 2.6: Detection spectra of the forced logistic map for $\epsilon = 0.3$, $T = 5 \cdot 10^4$, $n = 280$, $l = 4$ and $m = 3$. (a) comparison of the conventional PLSE and the extended PLSE; (b) comparison of the calibration parameter $\lambda_{l,m}$ and the Lyapunov exponent λ_{Lyap}

Looking at Fig. 2.6, the error occurs in transition zones where the Lyapunov exponent is very close to zero. While comparing the entropy spectra, it is clear that the detection of the transitions between the different types of dynamics is considerably improved by the ordinal matrix transform. Indeed, the entropy of tori is considerably decreased, thus taking much smaller values (close to zero) compared to the other dynamics.

2.5.4 Example of SNA detection in the Heagy-Hammel route

A SNA occurs in the Heagy-Hammel (H-H) route when the period-2^2 torus collides with its unstable parent [41, 54]. Such a phenomenon is observed in the quasi-periodically forced logistic map with $\epsilon = 0.3$. The H-H transition is known to appear at $r_0 \simeq 3.487793$ [60, 34]. We thus examined the behavior of the system in the neighborhood of r_0 and compared the result of the PLSE with the Lyapunov exponent. On the other side of the SNA there is a transition between SNA and chaos at $r_1 = 3.512$ [54]. In Fig. 2.7 we show the detection result. It can be clearly observed in the case of the PLSE there is a large gap between the entropy in tori and SNA, as well as between SNA and chaos regions. We set for this experiment $n = 210$, $l = 4$, $m = 2$. The corresponding calibration error is $\sigma = 5.237\%$. Similarly, we examined the neighborhood of $\beta_0 = 1.88697$ in the case of the cubic map with $A = 0.7$ where the system is known to exhibit a SNA (torus-SNA transition). Initially, it

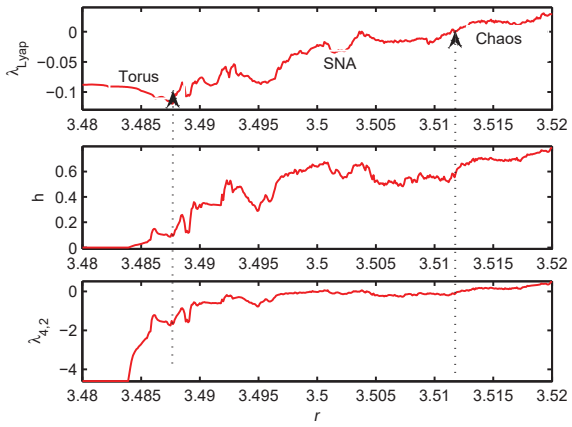

Figure 2.7: Detection of the transition from torus to SNA by the H-H route in the forced logistic map, $\epsilon = 0.3$, $n = 210$, $l = 4$ and $m = 2$. From top to bottom the Lyapunov exponent, the PLSE h and the calibration indicator $\lambda_{4,2}$ are shown.

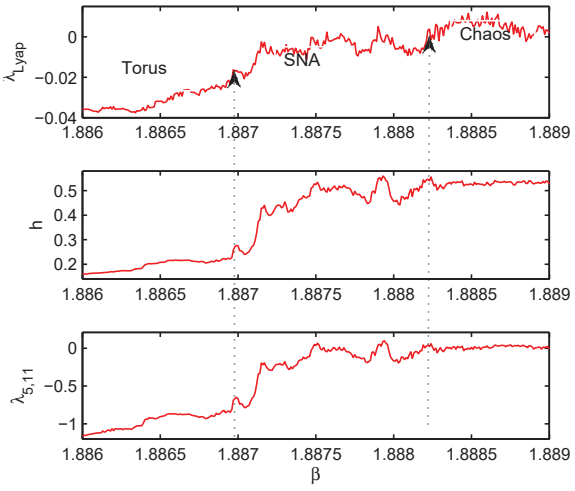

Figure 2.8: Detection of the transition from torus to SNA by the H-H route in the cubic map, $A = 0.7$, $n = 210$, $l = 5$ and $m = 11$. From top to bottom: the Lyapunov exponent, the PLSE h and the calibration indicator $\lambda_{5,11}$.

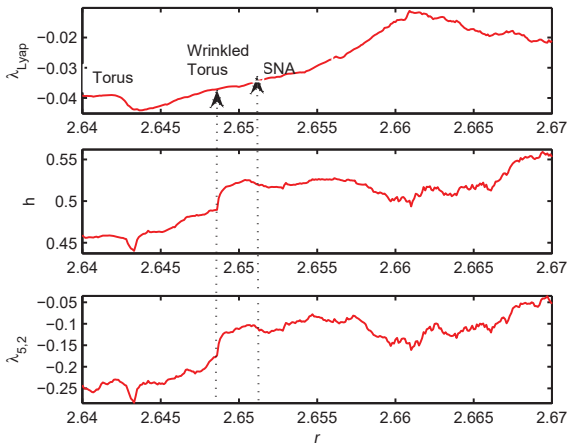

Figure 2.9: Fractalization route to SNA in the forced logistic map, $\epsilon = 1$, $n = 210$, $l = 5$ and $m = 2$. From top to bottom: the Lyapunov exponent, the PLSE h and the calibration indicator $\lambda_{5,2}$.

has for $\beta = 1.8865$ a period-2^i torus, $i \in \mathbb{N}$; this torus begins to wrinkle as β increases to the value 1.8868 where it approaches its unstable parent [34]. After the onset of SNA, the system moves smoothly toward a chaotic dynamics as β approaches 1.8875. For the detection of these changes, we set $n = 210$, $l = 5$ and $m = 11$. The results are compared in Fig. 2.8, for β varying from 1.886 to 1.889, by step size $\Delta\beta = 10^{-5}$. It can be easily observed that the PLSE once more allows to clearly distinguish between the torus and SNA, as well as SNA and chaos.

2.5.5 Example of detection of the fractalization route to SNA

The fractalization route to SNA has been detected in the logistic map for $\epsilon = 1$, between $r = 2.64$ and $r = 2.67$. In that case, a period-L torus attractor gets wrinkled and eventually forms an L-band SNA [34, 60]. Fig. 2.9 compares the results of the PLSE and the 0-1 test. The transition from torus to SNA appears at $r_0 = 2.6526$ [34], We varied r by step size $\Delta r = 10^{-4}$. The PLSE spectrum clearly shows the transition between torus and SNA at r_0. It can be observed that the $\lambda_{l,m}$-spectrum gives negative values, although the h-spectrum outputs entropy values around $h = 0.5$. The negativity of the $\lambda_{l,m}$ spectrum helps quickly making a decision in that case, whereas transitions can be clearly detected in both spectra.

We also analyzed the fractalization route to chaos in the cubic map. Once more, it

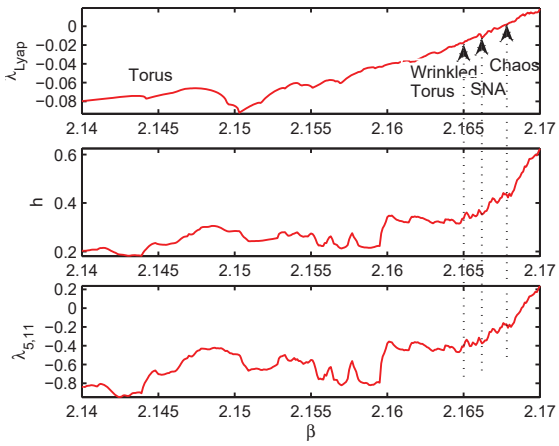

Figure 2.10: Fractalization route to SNA in the forced cubic map, $A = 0.1$, $n = 210$, $l = 5$ and $m = 11$. From top to bottom: the Lyapunov exponent, the PLSE h and the calibration indicator $\lambda_{5,11}$.

can be observed in Fig. 2.10 that the PLSE performs well for the detection of torus-SNA and SNA-chaos transitions. The experiment was conducted with $A = 0.1$, $n = 210$, $l = 5$, $m = 11$ and β varying from 2.14 to 2.17, with a step size $\Delta\beta = 10^{-4}$. The calibration error for this experiment is $\sigma = 4.319\%$. Comparing the PLSE-spectrum with the Lyapunov exponent, it is clear that the PLSE detects transitions occurring in the system behavior, even in the doubled torus region ($\beta = 2.14$ to $\beta = 2.167$). The system starts with a torus-like motion at $\beta = 2.14$, it thereafter exhibits a quasi-periodic oscillation of the double torus for $\beta = 2.16$, then moves to a wrinkled torus for $\beta = 2.165$; the SNA appears for $\beta = 2.167$ and finally, the system becomes chaotic for $\beta = 2.1675$ [34]. All these transitions can be clearly observed on the h and $\lambda_{l,m}$ spectra in Fig. 2.10.

2.6 Conclusion

In this chapter we presented the PLSE as the simplified and improved alternative for the 3ST algorithm. Using a probabilistic analysis of the permutation largest slopes, we compared the PLSE and PE results and showed that the PE is suitable for measuring the complexity of non-regular dynamics, while the PLSE is useful for detecting of regular dynamics. We also showed that the bias between the PE and the largest Lyapunov exponent in the case of regular dynamics is predictable only for $\gcd(L, \tau) = 1$ and $\gcd(L, \tau_0) = 1$.

Otherwise, the PE may take arbitrary values smaller than the predicted entropy of the dynamics under investigation, although it should be zero as referred to the KS entropy. The PLSE allows us to save computational time by choosing $1 < \tau_0 < n$ without affecting the detection capability, nor the estimation of the period of the limit cycles. The results thus presented confirm along the way the reliability of the permutation slopes for chaos detection. By using the QOM transform, we also investigated the applicability of the PLSE to the detection of SNA in quasi-periodically forced chaotic maps. Assuming that the entropy of tori and SNA reduces compared to that of the initial time series, whereas that of chaotic dynamics increases, the detection of transitions between tori and SNA as well as between SNA and chaotic dynamics becomes possible,but was not for other ordinal pattern-based algorithms. However, although the PLSE well performs for the detection of regular and non-regular dynamics, it should be pointed out that it cannot be used as a complexity measure. Moreover, it remains difficult to characterize an isolated time series, unless the spectrum of the whole system is known. Since in most of practical cases the challenge is to classify isolated non-regular dynamics by means of complexity measure, we investigate in chapter 3 the possibility of performing both the detection of regular dynamics and the complexity measure.

Chapter 3

The matching energy: a novel approach for complexity measure

Chapters 1 and 2 have presented the increasing improvements brought to ordinal pattern-based algorithms, but we have not established a complexity measure. In this chapter, we introduce an algorithm based on matching values in time series, namely the matching energy (ME). It consists of simply estimating the complexity by dividing the energy of the time series into the energy of non-matching samples and that of matching samples. The ME of periodic time series is equal to zero while non-regular dynamics present a positive ME. The approach thus defined allows to scale chaos in dynamical systems and presents a high robustness against noise as well as a high speed performance, hence is useful for real-time analysis of real-world data.

This algorithm has been presented in:

[22] J. S. A. Eyebe Fouda, The matching energy: a novel approach for measuring complexity in time series, Nonlinear Dyn. - (2016) DOI: 10.1007/s11071-016-3014-8.

3.1 Introduction

The main properties required for a nonlinear time series analysis method are the robustness against noise, high speed performance, applicability to short data sets, applicability to any type of data, and the classification ability (discerning between regular and non-regular dynamics or measuring the data complexity), and we just showed that the previous algorithms presented can only discern between regular and non-regular dynamics. Other various well

known theoretical approaches such as the Lyapunov exponents, Kolmogorov-Sinai (KS) entropy, correlation dimension and many others are difficult to estimate from a finite data set [1, 15, 19, 20, 31, 38], while empirical measures like the renormalized entropy or the approximate entropy often lack a theoretical foundation or are not easily readable [2, 58, 62]. The Rosenstein algorithm was designed to be robust against noise and can be applied to short length data [63]. It has the advantage of being easily interpretable as it refers to the theoretical Lyapunov exponent which is already known as a powerful tool for nonlinear system analysis. Unfortunately, this algorithm cannot be used for real-time data analysis as it is too time consuming.

In this chapter, we introduce a new algorithm for real-time complexity measurement in real-world time series, namely the matching energy (ME). It needs to fulfill the main properties required for a data analysis method, and needs to be particularly fast as it is designed for real-time analysis. The ME approach consists of simply estimating the complexity by dividing the energy of the time series into the energy of non-matching samples and that of matching samples. For this purpose, the time series is globally sorted into ascending and descending order and locally compared to the initial time series. Indeed, n-length embedding vectors (sequences) derived from the sorted and initial time series are compared. If some coordinates match in the two vectors, then the partial energy of the sequence is set to zero. If there are no matching coordinates, then the partial energy is positive. The ME for the whole time series is then obtained by averaging the partial energies of all the sequences, and will be equal to zero for periodic dynamics and positive for non-regular dynamics.

3.2 The matching energy approach

3.2.1 Definition of the matching energy

Let us consider a time series $\{x_t\}_{t=0,1,2\cdots T-1}$ and its globally sorted versions $\{u_t\}$ and $\{v_t\}$. $\{u_t\}$ is obtained by rearranging the values of $\{x_t\}$ into ascending order, while $\{v_t\}$ is obtained by rearranging $\{x_t\}$ values into descending order. From the time series $\{x_t\}$, $\{u_t\}$ and $\{v_t\}$, we derive n-length embedding vectors $\mathbf{x}_k = (x_{k\tau_0}, x_{k\tau_0+1}, \ldots, x_{k\tau_0+(n-1)})$, $\mathbf{u}_k = (u_{k\tau_0}, u_{k\tau_0+1}, \ldots, u_{k\tau_0+(n-1)})$ and $\mathbf{v}_k = (v_{k\tau_0}, v_{k\tau_0+1}, \ldots, v_{k\tau_0+(n-1)})$ respectively, where $k \in$

$\mathbb{N}$ and $1 \leq \tau_0 \leq n$ is the delay time of the embedding vectors. Since $\mathbf{x}_k$, $\mathbf{u}_k$ and $\mathbf{v}_k$ belong to an n-dimensional vector space $\mathbf{V}$, they can be easily compared.

The matching energy approach consists of projecting $\mathbf{x}_k$, $\mathbf{u}_k$ and $\mathbf{v}_k$ on two subspaces of $\mathbf{V}$: the vector space $\mathbf{V^{(1)}}$ of matching coordinates and the vector space $\mathbf{V^{(2)}}$ of non-matching coordinates of $\mathbf{x}_k$, $\mathbf{u}_k$ and $\mathbf{v}_k$, and to consider the energy of the different projections for evaluating the complexity of the time series. Let $\mathbf{y}_k$ and $\mathbf{z}_k$ be two vectors obtained by sorting $\mathbf{x}_k$ respectively into ascending and descending order (local sorting), n_1 is the number of matching coordinates between $\mathbf{y}_k$ and $\mathbf{u}_k$, and n_1' the number of matching coordinates between $\mathbf{z}_k$ and $\mathbf{v}_k$. Thus, $\mathbf{V^{(1)}}$ and $\mathbf{V^{(2)}}$ are respectively n_1-dimensional and $(n-n_1)$-dimensional vector spaces when considering $\mathbf{u}_k$, while $\mathbf{V'^{(1)}}$ and $\mathbf{V'^{(2)}}$ are respectively n_1'-dimensional and $(n-n_1')$-dimensional vector spaces when considering $\mathbf{v}_k$. Let E_{k+} be the energy of $\mathbf{x}_k$, E_{k+} is such that:

$$E_{k+} = \sqrt{\frac{1}{n}\sum_{i=1}^{n}\left(\mathbf{x}_k(i) - \overline{\mathbf{x}_k}\right)^2}, \tag{3.2.1}$$

where $\overline{\mathbf{x}_t}$ is the mean value of $\mathbf{x}_t$.

Similarly, let us consider the projections $\mathbf{u}_k^{(1)}$ and $\mathbf{v}_k^{(1)}$ of $\mathbf{u}_k$ and $\mathbf{v}_k$ respectively on $\mathbf{V^{(1)}}$ and $\mathbf{V'^{(1)}}$, and $\mathbf{u}_k^{(2)}$ and $\mathbf{v}_k^{(2)}$ the respective projections on $\mathbf{V^{(2)}}$ and $\mathbf{V'^{(2)}}$. The average distance (or mutual energy) between $\mathbf{y}_k$ and $\mathbf{u}_k$, and $\mathbf{z}_k$ and $\mathbf{v}_k$ for the matching coordinates is evaluated as:

$$d_{k-} = \frac{1}{2}\left(d_{k-}^{(u)} + d_{k-}^{(v)}\right), \tag{3.2.2}$$

where

$$d_{k-}^{(u)} = \sqrt{\frac{1}{n_1}\sum_{i=1}^{n_1}\left(\mathbf{y}_k^{(1)}(i) - \mathbf{u}_k^{(1)}(i)\right)^2} \tag{3.2.3}$$

and

$$d_{k-}^{(v)} = \sqrt{\frac{1}{n_1'}\sum_{i=1}^{n_1'}\left(\mathbf{z}_k^{(1)}(i) - \mathbf{v}_k^{(1)}(i)\right)^2}. \tag{3.2.4}$$

For the non-matching coordinates, this distance is evaluated as:

$$d_{k+} = \frac{1}{2}\left(d_{k+}^{(u)} + d_{k+}^{(v)}\right), \tag{3.2.5}$$

where

$$d_{k+}^{(u)} = \sqrt{\frac{1}{n-n_1}\sum_{i=1}^{n-n_1}\left(\mathbf{y}_k^{(2)}(i) - \mathbf{u}_k^{(2)}(i)\right)^2} \tag{3.2.6}$$

and

$$d_{k+}^{(v)} = \sqrt{\frac{1}{n-n_1'} \sum_{i=1}^{n-n_1'} \left(\mathbf{z}_k^{(2)}(i) - \mathbf{v}_k^{(2)}(i)\right)^2}. \tag{3.2.7}$$

It is obvious that $d_{k-} = 0$, $\forall\,(n_1, n_1')$.

The partial energy associated with the k-th embedding vectors $\mathbf{x}_k$, $\mathbf{u}_k$ and $\mathbf{v}_k$ derived respectively from $\{x_t\}$, $\{u_t\}$ and $\{v_t\}$, is defined as follows

$$E_k(n) = \begin{cases} 0, & \text{if } (n_1 + n_1') \neq 0; \\ E_{k+} + d_{k+}, & \text{otherwise.} \end{cases} \tag{3.2.8}$$

Applying this process to the whole time series, the average value of the partial energies E_k is considered as a complexity measure, hence:

$$E(n) = \frac{1}{N} \sum_{k=0}^{N-1} E_k(n), \tag{3.2.9}$$

where $N = 1 + \lfloor \frac{T-n}{\tau_0} \rfloor$ is the number of n-length embedding vectors explored. Embedding vectors with partial energy $E_k = 0$ are assumed to be perfectly predictable. The above Eq. (3.2.9) thus defines the matching energy of a given time series and applies to any type of data set. The ME approach is equivalent to splitting the whole orbit into small sequences and determine its complexity by discarding all the predictable sequences. A time series is less predictable when it contains few embedding vectors with zero partial energy.

3.2.2 Justification of the ME algorithm

The above definition of the complexity measure by the ME approach should allow to distinguish between periodic and non-regular time series. Indeed, let us assume that the time series $\{x_t\}$ is L-periodic, L being its phase space period (number of distinct samples per period) and q its time period. For simplicity, we assume $L = q$. By sorting the values of $\{x_t\}$ into ascending (respectively descending) order, the resulting time series $\{u_t\}$ (respectively $\{v_t\}$) is a stair function with L stairs, and is no longer periodic. Depending on n, L and T, E_k can be greater than zero or equal to zero. Let us assume $T = n_0 \cdot L$, where $n_0 \in \mathbb{N}_{\geqq 1}$ is the number of periods explored. This assumption implies that each stair of $\{u_t\}$ (respectively $\{v_t\}$) contains n_0 identical samples. The following cases can then be distinguished:

1st case: $n \geq L$

In that case, $\mathbf{x}_k$ contains all the L distinct samples of the series $\{x_t\}$. Two subcases can also be distinguished: the case $n \leq n_0$ and the case $n > n_0$.

If $n \leq n_0$, then $\mathbf{u}_k$ (respectively $\mathbf{v}_k$) contains a single value or two distinct values of $\{x_t\}$ if it includes a transition between two stairs of the series $\{u_t\}$ (respectively $\{v_t\}$). As $\mathbf{x}_k$ contains all the L possible values, at least one sample matches in $\mathbf{y}_k$ and $\mathbf{u}_k$ (respectively $\mathbf{z}_k$ and $\mathbf{v}_k$), hence $E_k = 0$. This result can be verified for the whole time series, thus implying that $E = 0$.

If $n > n_0$, $\mathbf{u}_k$ (respectively $\mathbf{v}_k$) contains more than a single value of $\{x_t\}$ and $E_k = 0$ as there is at least one matching sample in $\mathbf{y}_k$ and $\mathbf{u}_k$ (respectively $\mathbf{z}_k$ and $\mathbf{v}_k$), given that $n \geq L$. This result is also valid for the whole time series, hence $E = 0$.

2nd case: $n < L$

In that case $\mathbf{x}_k$ contains only n of the L distinct samples. As in the first case, two possibilities can be considered: $n \leq n_0$ and $n > n_0$. If $n \leq n_0$, then as shown in the first case $\mathbf{u}_k$ (respectively $\mathbf{v}_k$) contains one or two distinct values. However, as $n < L$ these values are not necessarily included in $\mathbf{x}_k$. It turns out that E_k depends on the ranking of the values in $\{x_t\}$. So, $E_k = 0$ is not guaranteed in that case. If $n > n_0$, although $\mathbf{u}_k$ (respectively $\mathbf{v}_k$) contains more than one distinct value, $E_k = 0$ is not guaranteed as $n_0 < L$.

Thus for periodic dynamics, $E(n) = 0$ is guaranteed if $n \geq L$. However, the above observation for $n < L$ is useful for detecting non-regular dynamics. Indeed, the phase space period L of non-regular dynamics tends to infinity and there is no possibility for considering $n > L$. Thus, the energy $E(n)$ is positive as matching samples are rare.

3.2.3 Complexity measure by the ME algorithm

In sufficiently large truly random time series, each value (or symbol) is equiprobable and any significant deviation from equiprobability is considered as evidence for deterministic structure in the data [66]. Given a time series assumed to be deterministic, its complexity increases as the number of distinct samples is large and there is no particular rule for describing their time evolution. For a single value time series for example, the complexity is equal to zero as the ordering of the time series is trivial. The complexity of a T-length

time series with T distinct samples ranged in ascending or descending order also is equal to zero ($E = 0$) due to the trivial ordering of the data. By randomly rearranging these values, the complexity increases as the degree of randomness increases. The complexity of a time series does not depend on the range of the samples, whereas the energy does depend on it. For instance, multiplying a given time series by a factor κ should not modify its complexity, although its energy is multiplied by the same factor. As the ME algorithm is based on energy measurement, it follows from the above observation that it should be applied to normalized time series for it to be considered as a complexity measure.

The ME algorithm is strongly related to the existence of matching samples between embedding vectors $\mathbf{x}_k$, $\mathbf{u}_k$ and $\mathbf{v}_k$. The condition of matching samples between signal sequences is sensitive to the precision of the time series values. Indeed, from the definition of the ME, the complexity of the dynamics is greater when the number of embedding vectors with matching samples (zero partial energy) is smaller. So, considering values with a too large a precision may reduce the number of sequences with matching samples as even close samples may be detected as different, hence increasing the sensitivity of the ME algorithm to small changes (even to the noise effect). Therefore, for an efficient comparison of the samples, we suggest reducing the data precision by using the DDQ presented in chapter 1 [28]. Applying the ME algorithm to the time series with reduced precision improves the complexity measure. However, such an improvement is only possible if the initial precision of the time series is greater than the one imposed by DDQ.

Given that only a maximum number of T values is allowed in the quantized time series of length T, for data with too large precision, we suggest to consider the noise threshold η satisfying

$$\eta \geq \frac{\max(\{x_t\} - \min(\{x_t\}))}{T} \tag{3.2.10}$$

where $\{x_t\}$ is the normalized time series. For a unipolar time series, $\eta \geq 1/T$, while $\eta \geq 2/T$ for a bipolar time series. By normalizing the time series, the range of the values is not exactly known. For a unipolar time series for example, values in the normalized time series may vary between $\xi \geq 0$ and 1; for a bipolar time series, values may lie between $-\xi$ and 1 or between -1 and ξ. For this purpose, we suggest choosing the precision so that $\eta < \zeta/T$, $0.1 \leq \zeta \leq 2$. It should be noticed that whenever the true precision η_0 of the input time series is smaller than η ($\eta_0 > \eta$), the quantization has no effect on the output of the

ME algorithm. For instance, choosing $\eta = 10^{-5}$ for a 10-bits encoded time series has no impact on the ME result. For the ME algorithm to be sensitive to η in that case, it must choose $\eta > 1/1024$.

The whole ME algorithm is thus summarized as follows:

Algorithmic steps:

Step1: Normalize $\{x_t\}$ by dividing all the values x_t by its maximum absolute value x_m;

Step2: Apply the DDQ to the normalized time series $\{x_t\}$;

Step3: Sort the values of $\{x_t\}$ into ascending and descending order to obtain $\{u_t\}$ and $\{v_t\}$, respectively;

Step4: For the k-th embedding vectors $\mathbf{x}_k$, $\mathbf{u}_k$ and $\mathbf{v}_k$, sort the values of $\mathbf{x}_k$ into ascending and descending order and determine the energy $E_k(n)$ using Eq. (3.2.8);

Step5: Compute the ME or complexity $E(n)$ of the whole time series by averaging all the partial energies $E_k(n)$ as indicated in Eq. (3.2.9);

The full MATLAB code of the ME algorithm is available online[1].

3.3 Impact of the parameter setting on the result

In this section we apply the ME algorithm to simulation data generated from the logistic map in order to evaluate the impact of the parameter setting to the algorithm results. For validation purposes, we compare the matching energy spectra with the Lyapunov exponent.

We plotted the energy and the Lyapunov spectra for $3.5 \leq \mu \leq 4$, by step size $\Delta r = 10^{-3}$. In Fig. 3.1 we compare the ME and Lyapunov exponent spectra for $T = 10^5$, $n = 200$, $\tau_0 = n$. Initially, values in $\{x_t\}$ are double precision data and we reduced their precision to $\eta = 10^{-5}$. It is clearly observed from this figure that the spectrum of the ME algorithm tracks the Lyapunov exponent spectrum. Indeed, all the periodic dynamics are well detected with a zero complexity. This interesting result suggests a suitable parameter setting. We thus analyzed the impact of each parameter on the result.

[1] at `http://www.mathematik.uni-kassel.de/~fouda/`

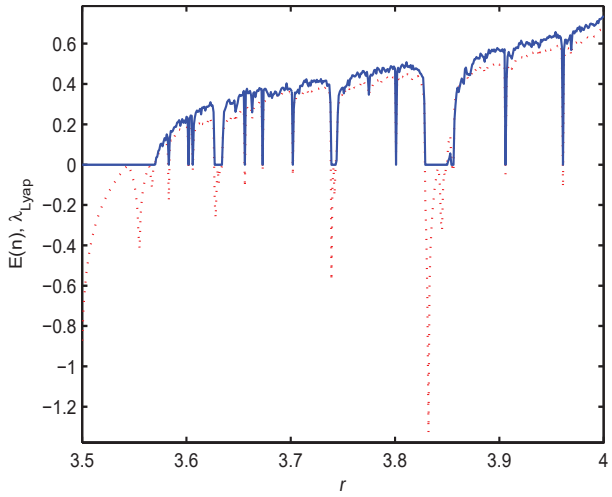

Figure 3.1: Comparison of the ME (solid line) and the Lyapunov exponent (dotted line) spectra of the logistic map for varying control parameter $3.5 \leq r \leq 4$ (step $\Delta r = 10^{-3}$): $T = 10^5$, $n = 200$, $\tau_0 = n$ and $\eta = 10^{-5}$

3.3.1 Impact of the embedding dimension n

We showed that in the case of periodic dynamics with no repeated value in the basic period, the embedding dimension should be chosen such that $n \geq L$. We then evaluated the energy spectrum of the logistic map for various values of n, for $T = 10^4$, $\tau_0 = 10$ and $\eta = 0.5/T$. The corresponding results are shown in Fig. 3.2. It appears that the value of E for the whole spectrum reduces as n increases. This observation may be justified by the reduction of the number of embedding vectors, which is controlled by τ_0. While considering the case of $\mu = 3.602$ corresponding to an 88-periodic dynamics, it is observed that $E > 0$ for $n < 88$. For this dynamics to be detected as regular with $n < 88$, we need to increase the noise tolerance η.

3.3.2 Impact of the delay time τ_0 of embedding vectors

The delay time of embedding vectors τ_0 let us to control the computational time of the ME algorithm. It should be chosen such that $1 \leq \tau_0 \leq n$. The larger τ_0, the smaller the number of embedding vectors to be explored, hence the smaller the computational time. However, we observed that choosing few embedding vectors also alters the quality of the estimate of E. This indicates a compromise between the computational time and the estimate of the

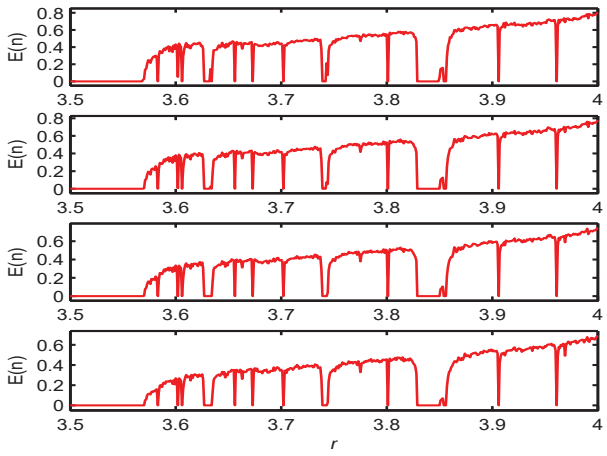

Figure 3.2: Dependence of the ME on the embedding dimension n, $T = 10^4$, $\eta = 0.5/T$, $\tau_0 = 10$. From top to bottom, $n = 30$, 50, 100, and 200.

ME.

In Fig. 3.3 we show some spectra obtained for $\tau_0 \in \{1, 20, 200\}$, with $T = 10^4$, $n = 200$ and $\eta = 0.5/T$. In this figure, the spectrum with $\tau_0 = 1$ is easier to interpret than the one with $\tau_0 = n$. Nevertheless, large values of τ_0 can be considered for large observation times, provided that the number of embedding vectors is statistically significant. Hence, the complexity of a given time series can be well estimated even with short length data, provided that the number of embedding vectors is suitably chosen.

3.3.3 Impact of the noise tolerance η

The noise tolerance η is used for suppressing noise due to rounding errors, sampling errors or external noise. η was defined as the minimum difference between two signal samples to be considered as different. In the ME algorithm, η is used to reduce the matching error which may be induced by the noise effect. The value of η should always be smaller than 1, the amplitude of the normalized signal. In our simulations, we choose $0.1/T \leq \eta \leq 2/T$ for noise free data. In Fig. 3.4 we show some spectra evaluated with different values of η. We used $T = 10^4$, $n = 200$ and $\tau_0 = 10$. It is observed from this figure that the spectra are smooth when η is small, but the estimate of the complexity, as compared to the Lyapunov exponent, is well approximated as η increases.

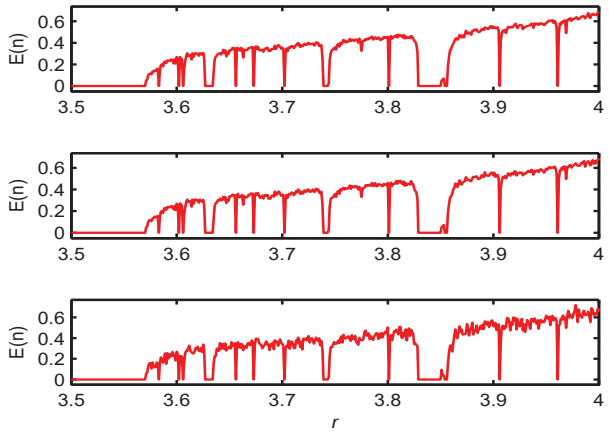

Figure 3.3: Dependence of the ME on the delay time of embedding vectors τ_0, $T = 10^4$, $\eta = 0.5/T$, $n = 200$. From top to bottom, $\tau_0 = 1$, 20 and 200.

3.3.4 Robustness against noise

The DDQ has been shown effective for noise reduction in the case of the PLSE [28]. In this chapter, while combined with the ME approach, the DDQ also improves the complexity measure. In the case of noisy data, the value of η should be chosen according to the degree of disturbance. Indeed, for noise with amplitude σ, the noise tolerance should be chosen as $\eta \geq \sigma$. We thus considered the logistic map perturbed by dynamical and observational noise with uniform distribution, whose standard deviations vary from $\sigma = 0.0005$ to $\sigma = 0.005$. In the case of the dynamical noise, the noisy logistic map is given by:

$$x_{t+1} = rx_t(1 - x_t) + \sigma b_t \tag{3.3.1}$$

where b_t are uniformly (uniform noise) distributed values and σ the standard deviation of the noise. For the observational noise, the noise samples are simply added to the output samples of the logistic map, thus leading to the following equation:

$$x_t^b = x_t + \sigma b_t \tag{3.3.2}$$

where x_t is given by Eq. (1.3.1) and x_t^b is the logistic map contaminated by the observational uniform noise b_t. The noise b_t is characterized by a standard deviation $\sigma_0 = 1$ and a mean value $\overline{b_t} = 0$. The corresponding MATLAB expression is given as $b_t = 4(-0.5 + rand)$.

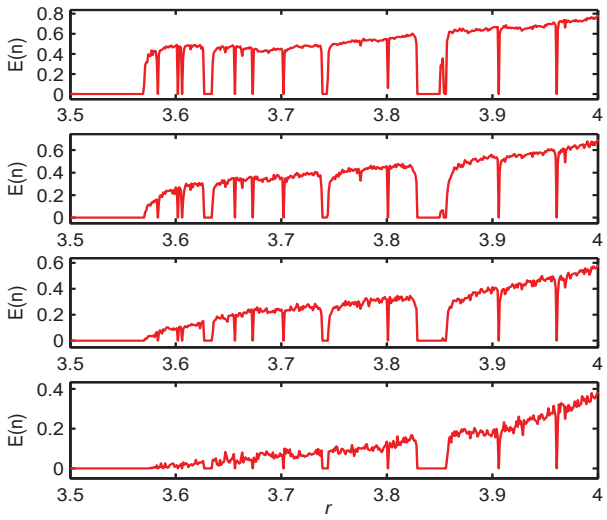

Figure 3.4: Dependence of the ME on the data precision η, $T = 10^4$, $\tau_0 = 10$, $n = 200$. From top to bottom, $\eta = 0.1/T$, $0.5/T$, $1/T$ and $2/T$.

In Fig. 3.5 we give some spectra of the logistic map for various noise amplitudes σ, for both observational and dynamical uniform noise. Looking at this figure, the ME algorithm exhibits a high robustness against observational noise as only small values of η (the same used for noise free data) are required for suppressing the noise effect. In the case of dynamical noise, using the same values of η as for noise free data, the behavior of the ME spectrum for noisy data looks similar to that of noise free data, except for regular dynamics as the internal behavior of the system is affected by the noise. We also tested the algorithm with the Gaussian noise and obtained approximately the same results. From these results, we can conclude that the ME algorithm performs well in the presence of noise, hence it can be applied to real-world data.

3.3.5 Speed performance of the ME algorithm

The real-time application of the ME algorithm to time series analysis also requires that the algorithm is computationally low cost. We compared in this section the speed performance of the ME algorithm to that of the fast CPE whose MATLAB code is available online[2]. The computational complexities of the algorithms are compared based on the approach we

[2] at `www.mathworks.com/matlabcentral/fileexchange/48684-fast-conditional-entropy-of-ordinal-patterns`

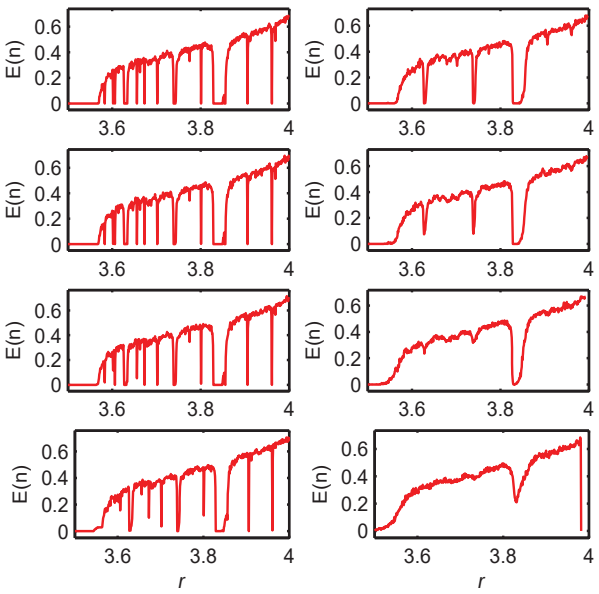

Figure 3.5: Robustness against noise of the ME algorithm, $T = 10^4$, $\tau_0 = 10$, $n = 200$. From top to bottom, $\sigma = 5 \cdot 10^{-4}, \eta = 0.5/T$; $\sigma = 10^{-3}, \eta = 0.5/T$; $\sigma = 2 \cdot 10^{-3}, \eta = 0.5/T$; and $\sigma = 5 \cdot 10^{-3}, \eta = 0.55/T$. The left side shows results for the observational noise, while the right side shows results for the dynamical noise.

used in [26]. The test code below was run for 100 iterations to get the average running time D_0. The average running time of the fast CPE and the ME algorithm are respectively D_1 and D_2, obtained by evaluating each algorithm for 100 iterations. The complexity K of the algorithm is theorized by:

$$K_i = \frac{D_i}{D_0} \tag{3.3.3}$$

where $i = 1$ for the fast CPE and $i = 2$ for the ME algorithm. The test code is given as:

a=1:20000
for k=1:20000
b(k)=1/sqrt(a(k))
*c(k)=a(k)*b(k)*
$d(k) = \sqrt[3]{c(k)}$
end

Using this definition, the complexities of the fast CPE and ME algorithms are respectively $K_1 = 9.3737$ (corresponding to $D_1 = 0.0950s$ average running time on our computer) and $K_2 = 0.4469$ (corresponding to $D_2 = 0.0045s$ average running time on our computer). The comparison of these values confirms that the ME algorithm is computationally low cost by a wide margin (more than ten times faster) compared to the fast CPE, although the algorithm has not yet been optimized. The speed performance of the ME algorithm can be controlled by τ_0, which is not possible for the CPE algorithm. Indeed, we showed in [28] that the permutation entropy strongly depends on τ_0, and that satisfactory results are obtained only for $\tau_0 = 1$. We used an input sequence of length $T = 10^4$ samples for both algorithms, as well $\tau_0 = 200$, $\eta = 1/T$ for the ME algorithm and $n = 7$ for the fast CPE algorithm. The average running time of the test code is about $D_0 = 0.0101s$

3.4 Example of application

3.4.1 Application to the Duffing oscillator

The Duffing oscillator is used in this section as an example of a continuous time system, for verifying the efficiency of the ME algorithm for the analysis of this type of systems. The analysis of continuous time series is quite difficult as the errors due to the sampling process and the precision of the integrator should be taken into account. The time series should then be considered as noise contaminated. The Duffing system is described by the system of ordinary differential equations defined in Eq. (1.6.2) with $a = 0.3$. We used the fourth order Runge-Kutta algorithm to solve Eq. (1.6.2) with sampling step $T_s = 4\pi/1000$. The parameters of the MATLAB integrator was set as RelTol $= 10^{-5}$ for the relative error tolerance and AbsTol $= 10^{-5}$ for the absolute error tolerance of the x_t and y_t variables. The solutions x_t and y_t are analyzed and the corresponding energies are compared. We used as noise tolerance $\eta = 3.75 \cdot 10^{-6}$, and the data length is $T = 400001$.

We applied the ME algorithm to both the continuous time series and the series of the local maxima. For the continuous time series, we set $n = 2 \cdot 10^4$ and $\tau_0 = 1.8 \cdot 10^4$; while for the series of local maxima, we set $n = 180$ and $\tau_0 = 1$. The corresponding results are depicted in Fig. 3.6. Compared to the Lyapunov exponent, it appears that the ME algorithm performs well for the detection of chaos in continuous time systems. Using the

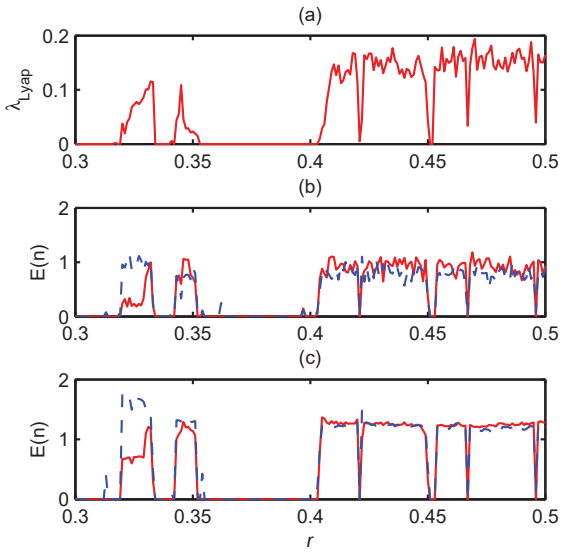

Figure 3.6: ME spectrum of the Duffing oscillator. In (b) and (c) the results for x_t variable (continuous line) and y_t variable (dashed line) are plotted. (b) is the result obtained with the whole time series with $n = 20000$, $\tau_0 = 18000$ and $\eta = 3.75 \cdot 10^{-6}$, while (c) is obtained using exclusively the series of local maxima with $n = 180$, $\tau_0 = 1$ and $\eta = 3.75 \cdot 10^{-6}$

series of local maxima allows to speed up the detection process, hence to make possible the real-time analysis of large amount of data from continuous time real-world systems. It is also observed that the spectra of both the x and y variables behave quite similarly, which confirms that only a single time series is required for the ME algorithm to characterize the complexity of a given system. This result is important as in practice only a single record is available for many experiments.

3.4.2 Application to real-world data

We applied the ME algorithm to data generated from the electronic circuit exhibiting the Duffing attractor [24]. The electrical model of the corresponding system is shown in Fig. 3.7. Resistors values are chosen as $R_0 = 2.2k\Omega$, $R_1 = 5.1k\Omega$, $R_2 = R_3 = 1k\Omega$. Capacitors values are $C_1 = 10nF$ and $C_2 = 2.2nF$. The nonlinear element (NLE) implements the cubic function $i(x) = ax + bx^3$ where a and b can be experimentally evaluated, $i(x)$ indicates the current through the NLE and x is the voltage across it. Fig. 3.8 presents its schematic where exclusively resistors and diodes are used. Resistances values are: $R_4 = 8.2k\Omega$ and

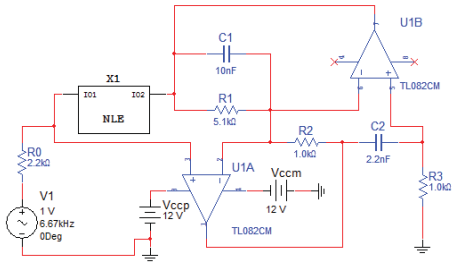

Figure 3.7: Schematic of the forced Duffing oscillator

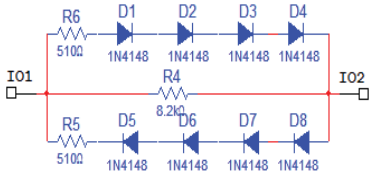

Figure 3.8: Schematic of the nonlinear element (NLE)

$R_5 = R_6 = 510\Omega$. The diodes are 1N4148 type and the TL082 integrated circuit (IC) is used as operational amplifier (OA). This circuit has been implemented and the data recorded for 300 forcing amplitudes as well as corresponding analogue phase portraits are available online[3]. We used the RIGOL 1052DSE digital oscilloscope with sampling frequency $F_s = 1\,\text{MHz}$, as shown in Fig. 3.9. The forcing amplitude and frequency (generated by the sine wave function generator) were set as $0.2\text{V} \leq V_m \leq 6.18\text{V}$ and $f = 6.67\,\text{kHz}$, respectively. Data were recorded in the comma separated values (CSV) format, which is easily readable in the Matlab environment. Given the practical limitation of the digital oscilloscope, each record had only 8192 samples per channel. There are two channels representing voltages x_1 and x_2 across C_1 and C_2, respectively. Acquired data are 8-bit encoded, which implies that the noise tolerance should be chosen such that $\eta > 2^{-8}$ for the algorithm to be sensitive to it.

The first 192 samples of variables x_1 and x_2 were discarded for transient die out, and

[3]at `http://www.mathematik.uni-kassel.de/~fouda/`

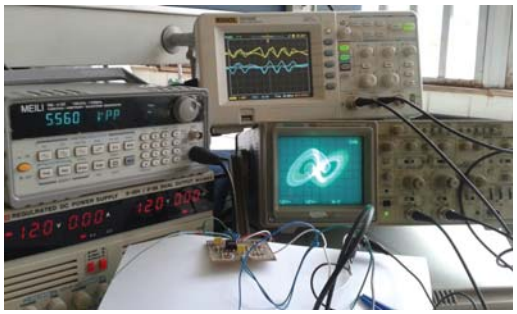

Figure 3.9: Data acquisition experiment

the algorithm was applied separately to the series of local extrema of each variable with $n = 15$ and $n = 30$. Due to the presence of noise, the spectra of the two variables are not behaving similarly. For tackle this, we considered the geometric mean $E(n) = \sqrt{E_{x_1} \cdot E_{x_2}}$ for the decision making. Using the Rosenstein algorithm [63], we also computed the maximal Lyapunov exponent (MLE) for the two variables and considered the geometric mean $MLE = \sqrt{MLE_{x_1} \cdot MLE_{x_2}}$. The corresponding results are depicted on Fig. 3.10. We respectively analyzed the case of noisy data ($\eta = 0$), and the case of noise reduced data ($\eta > 0$) by means of the DDQ. We set for this last case $\eta_{x_1} = 1.9570\%$ and $\eta_{x_2} = 1.9922\%$ in Fig. 3.10(b), and $\eta_{x_1} = \eta_{x_2} = 1.9531\%$ for both variables x_1 and x_2 in Fig. 3.10(c). As observed on Fig. 3.10(b) where $n = 15$, the algorithm presents a high natural robustness against noise and successfully detects changes in the system dynamics. By using the noise reduction, the inherent robustness of the method against noise is reinforced and the periodic dynamics are thus detected with a zero energy, while that of chaotic dynamics remains unchanged. By setting $n = 30$, the detection is improved and even dynamics with large phase space periods ($V_m > 3.30$) as shown on Fig. 3.10(c) can be detected with a zero complexity. The system has been already calibrated in our previous work [24] and is known to exhibit chaotic dynamics approximately for $2.4 \leq V_m \leq 2.85$ and $3.16 \leq V_m \leq 3.30$. For $V_m < 2.4$ the system exhibits periodic dynamics with weak phase space periods, while for $V_m > 3.30$, the phase space periods of the system are large. Compared to the MLE, the results of the ME algorithm are confirmed if the three peaks Pk1, Pk2 and Pk3 appearing on the MLE spectrum are interpreted as chaotic regions. The results obtained are also consistent with those already presented in [24] for the PLSE algorithm. From the above results, it can be

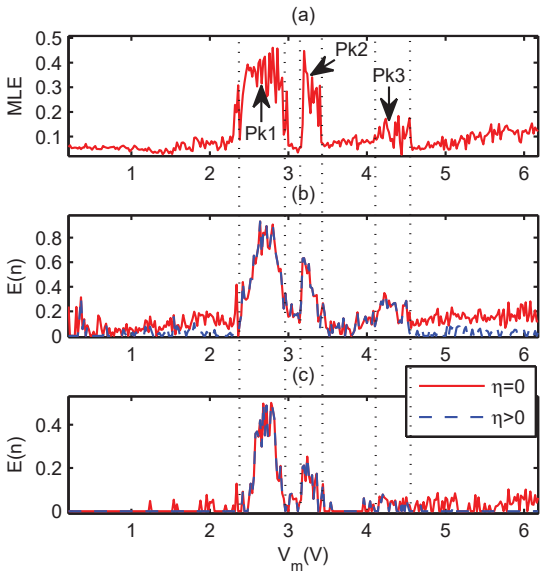

Figure 3.10: Experimental ME spectrum of the Duffing oscillator: (a) MLE spectrum; (b) ME spectra for $n = 15$, $\eta = 0$ (solid line) and $\eta_{x_1} = 1.9570\%$, $\eta_{x_2} = 1.9922\%$ (dashed line); and (c) ME spectra for $n = 30$, $\eta = 0$ (solid line) and $\eta_{x_1} = \eta_{x_2} = 1.9531\%$ (dashed line)

concluded that the ME performs well with experimental data. Furthermore, given the large value of the precision of the data analyzed (2^{-8}), the algorithm can clearly detect chaotic dynamics without need for noise reduction, while using the set of local extrema. This result confirms its high robustness against noise and the assumption made for its sensitivity to the data precision.

For the Rosenstein algorithm [63], we set the embedding dimension to $m = 18$, the sampling frequency to $F_s = 100\,\text{Hz}$ instead of 1 MHz to avoid large values of MLE, and the number of iterations as n_{it}=100. Given the difficulty of determining the optimal values of time lag τ and mean period T_0, we set $\tau = 6$ and $T_0 = 100$, respectively, for the complete data set.

3.4.3 Application to the detection of quasi-periodic dynamics

In this section we apply the ME algorithm to the sine-circle whose equation is given in Eq. (1.2.2), and which is known to exhibit quasi-periodic dynamics as the control parameter r varies from 0 to 1. We used as parameter setting for the ME algorithm $n = 200$, $\tau_0 = 50$ and $\eta = 10^{-5}$. The result presented in Fig. 3.11 is obtained for $T = 2 \times 10^4$ and shows that

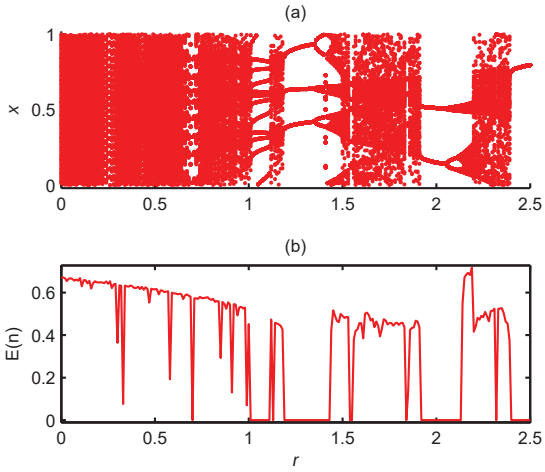

Figure 3.11: ME spectrum for the sine-circle map: (a) bifurcation diagram (b) ME spectrum for $n = 200$, $\tau_0 = 50$, $\eta = 10^{-5}$ and $T = 2 \times 10^4$

the ME successfully detect periodic and chaotic dynamics, but fails to detect quasi-periodic dynamics with a zero complexity. This result implies that the ME algorithm is not useful for the analysis of quasi-periodically forced systems.

In summary, the ME algorithm can be efficiently applied to both discrete and continuous time systems. For an efficient determination of matching samples, the precision of the data under consideration needs to be limited to a finite value, depending on the data length. The embedding dimension n also should be chosen such that $L < n$, where L is the phase space period of the dynamics to be analyzed. In general, the embedding dimension should be greater than the time period of the dynamics. However, the observation time should increase as the embedding dimension increases to avoid false detection of periodic dynamics. Indeed, in the case when the embedding dimension is equal to the data length, then the dynamics is detected as periodic, according to the definition of the ME. So, the complexity is close to zero as the ratio between the embedding dimension and the data length is small, thus leading to a compromise between the choice of the embedding dimension in terms of the data length and the phase space period of the dynamics. We observed from the simulation results that the ME spectrum tracks the largest Lyapunov exponent λ_{Lyap} with a quite uniform bias which depends on the ratio between the data length and the embedding dimension, and also on the limiting precision η of the data. Choosing embedding dimensions

smaller than the phase space period can help to detect changes in the system dynamics. However, it should be noticed that the ME fails to detect quasi-periodic dynamics as regular.

3.5 Conclusion

In this chapter we introduced the ME approach in which the energy of globally and locally sorted sequences with matching samples is set to zero. The approach let us efficiently detect periodic dynamics with a zero complexity while chaotic dynamics are characterized by a nonzero complexity. Compared to existing detection algorithms, the ME algorithm is computationally low cost and is well suited for real-time data analysis. The method integrates the DDQ process for limiting the precision of the data to be analyzed to a finite value, which contributes to increasing its robustness against noise, thus making it useful for the analysis of real-world data. Considering the examples chosen for simulation, the ME algorithm tracks the Lyapunov exponent with a uniform bias which depends on the setting of the parameters n, η, τ_0 and T. Based on this observation, the ME algorithm appears to be suitable for real-time analysis of real-world data, more so than the Rosenstein algorithm which is computationally costly. The dependence of the algorithm on the parameter setting can be freely fixed according to the system under investigation and the range of complexity required by the user. We intend to apply the ME algorithm to electroencephalography for detecting the epileptic seizures. However, although we can now determine a complexity measure from real-world data, it should be be nevertheless pointed out that the ME fails to detect quasi-periodic dynamics. In the next chapter, we intend to characterize data generated from quasi-periodically driven systems.

Chapter 4

Ordinal-array-based indicators and SNA detection

The ordinal matrix transform introduced in Chapter 2 is extended to multidimensional arrays of permutations. The corresponding multidimensional ordinal array complexity (OAC) is presented as a generalized approximation to the ordinal Komogorov-Sinai entropy. We theoretically establish that the OAC provides a better estimate of the complexity measure for short length time series. However, given that it does not indicate a zero complexity for periodic dynamics with large period and other regular dynamics like SNA and tori, we consider the behavior of the number of OA in terms of the corresponding embedding dimension to define three new indicators, namely the periodicity, the quasi-periodicity and the non-regularity index. Combining these indicators provides complementary information and much richer possibilities for classifying regular and non-regular dynamics, than using only entropy-based algorithms.

This chapter presents an extension of our investigation into complexity measures and has not yet been published.

4.1 Introduction

To the best of our knowledge, research results on the application of ordinal pattern-based algorithms to quasi-periodically forced systems have never been reported before our work in [23]. The main reason for this research is probably due to the difficulty in distinguishing between quasi-periodic and chaotic dynamics using ordinal patterns related complexity

measure. Indeed, the PE, the CPE and other versions of ordinal pattern-based algorithms are not able to output a zero complexity or entropy when applied to quasi-periodic dynamics. We showed using the permutation largest slopes that periodic dynamics and some less complex quasi-periodic dynamics can be detected with a zero entropy [28]. However, when the number of incommensurable frequencies composing the quasi-periodic dynamics increases, even the PLSE is no longer able to output a zero entropy. We also showed in chapter three that even the ME fails to detect quasi-periodic dynamics. Considering that quasi-periodically forced systems exhibit dynamics which are more complex than the driving quasi-periodic signal, the analysis of the time series they are generating still remains a challenging task.

To address this concern, we suggest applying the OPA to the values of the series of ordinal patterns derived from the time series for measuring its complexity. Moreover, by analyzing the increasing law of the number of symbols in terms of the embedding dimension, we introduce three OA asymptotic growth indices as complementary chaos indicators. As the effective number of symbols can be evaluated for ordinal patterns of order n, the entropy of the new source of symbols can be well estimated. This approach let us increase the number of patterns which has been reduced by the conversion into ordinal patterns, and thus better approximate the entropy of the time series. For instance, for a given real-world time series with Λ distinct symbols or values, the number of distinct ordinal patterns of order n is $n!$, while the number of distinct embedding vectors of the same order derived from the time series values is Λ^n. Now considering the series of ordinal patterns of order n, the number of possible distinct embedding vectors of order n which can be derived from the time series values increases as $(n!)^n \gg n!$. The OA-based indices should thus allow us to efficiently distinguish between the different types of regular and non-regular dynamics, hence to achieve the detection of SNA.

4.2 Ordinal array entropy

4.2.1 Construction of M-dimensional ordinal arrays

Measuring the Shannon entropy of an information source requires that the number of symbols is known and that the set of symbols (often called the alphabet $\mathcal{A}$) is of finite size;

otherwise, the Shannon entropy is infinite. It is common to define the information entropy in bits. In the case of continuous random variables such as the speech signal for example, a uniform quantizer can be used to convert the corresponding continuous alphabet into a discrete one. Symbols of the discrete alphabet thus obtained are encoded with a finite number of bits. Similarly, the ordinal pattern analysis approach which considers the order relations between values of the time series instead of the values themselves can be seen as a quantizer. It then converts the continuous alphabet of the source into an ordinal pattern alphabet. Each ordinal pattern is encoded using positive integers. The set of ordinal patterns can then be considered as a pseudo-source of information. If n is the length of ordinal patterns, then the cardinality of the ordinal pattern alphabet is $n!$, while defining patterns of the same length using the values of the time series would have led to an Λ^n-length alphabet, Λ being the number of distinct values of the time series. It appears that considering the order relation between values instead of the values themselves reduces the number of distinguishable patterns. This reduction of the number of accessible patterns also leads to a reduction of the diversity of the original time series, hence the reduction of its complexity. This observation may justify why the PE of finite order n does not well approximate the KS entropy.

Although the PE converges to the KS entropy as n tends to infinity for some maps, the PE of finite order can be either much greater or much smaller than the KS entropy [67]. In order to reduce the difference between the PE and the KS entropy, the CPE was defined as the average diversity of ordinal patterns succeeding a given one [67]. The CPE characterizes the diversity of the successors of the given ordinal patterns, whereas the PE characterizes the diversity of the ordinal patterns themselves. In our approach, we propose to convert the pseudo-source of ordinal patterns into a set of M-dimensional arrays of ordinal patterns or simply M-dimensional ordinal arrays (OA) and to measure their diversity. Indeed, given the set $\{P_k\}$ of ordinal patterns, we define another set $\{\mathbf{S}_{t_1}^{(1)}\}$ of OA such that $\mathbf{S}_{t_1}^{(1)} = \left(P_{t_1}^T, P_{t_1+\tau}^T, \cdots, P_{t_1+(d_1-1)\tau}^T\right)$, where $P_{t_1}^T$ is a column vector (the transpose of P_{t_1}). P_{t_1} is an n-length vector of positive integers in $\{1, 2, 3, \cdots, n\}$, while $\mathbf{S}_{t_1}^{(1)}$ is an $n \times d_1$ matrix of the same integer set, and d_1 the number of permutations considered to form $\mathbf{S}_{t_1}^{(1)}$.

Let us clarify this presentation by considering for example a period-5 cycle orbit obtained

by generating 5 distinct random numbers $(0.8147, 0.9058, 0.1270, 0.9134, 0.6324)$ and repeating this basic sequence K-times ($K > 2$). The five distinct 5-order permutations obtained by sorting the values of vectors $\mathbf{x}_k$, k=0 to 4, are the following: $P_0 = \left(\frac{1,2,3,4,5}{3,5,1,2,4}\right)$; $P_1 = \left(\frac{1,2,3,4,5}{2,4,5,1,3}\right)$; $P_2 = \left(\frac{1,2,3,4,5}{1,3,4,5,2}\right)$, $P_3 = \left(\frac{1,2,3,4,5}{5,2,3,4,1}\right)$ and $P_4 = \left(\frac{1,2,3,4,5}{4,1,2,3,5}\right)$. The corresponding set of ordinal patterns for the whole time series is $\{P_{t_1}\} = \{P_0, P_1, P_2, P_3, P_4, P_0, P_1, P_2, P_3, P_4, P_0, P_1, P_2, \ldots\}$. From $\{P_{t_1}\}$, one can deduce for example $\{\mathbf{S}^{(1)}_{t_1}\} = \{\mathbf{S}^{(1)}_0, \mathbf{S}^{(1)}_1, \mathbf{S}^{(1)}_2, \mathbf{S}^{(1)}_3, \mathbf{S}^{(1)}_4, \mathbf{S}^{(1)}_0, \cdots\}$ as the set of 5×3 OA, where $\mathbf{S}^{(1)}_0 = \begin{pmatrix} 3 & 2 & 1 \\ 5 & 4 & 3 \\ 1 & 5 & 4 \\ 2 & 1 & 5 \\ 4 & 3 & 2 \end{pmatrix}$, $\mathbf{S}^{(1)}_1 = \begin{pmatrix} 2 & 1 & 5 \\ 4 & 3 & 2 \\ 5 & 4 & 3 \\ 1 & 5 & 4 \\ 3 & 2 & 1 \end{pmatrix}$, $\mathbf{S}^{(1)}_2 = \begin{pmatrix} 1 & 5 & 4 \\ 3 & 2 & 1 \\ 4 & 3 & 2 \\ 5 & 4 & 3 \\ 2 & 1 & 5 \end{pmatrix}$, $\mathbf{S}^{(1)}_3 = \begin{pmatrix} 5 & 4 & 3 \\ 2 & 1 & 5 \\ 3 & 2 & 1 \\ 4 & 3 & 2 \\ 1 & 5 & 4 \end{pmatrix}$, and $\mathbf{S}^{(1)}_4 = \begin{pmatrix} 4 & 3 & 2 \\ 1 & 5 & 4 \\ 2 & 1 & 5 \\ 3 & 2 & 1 \\ 5 & 4 & 3 \end{pmatrix}$. Therefore, $n = 5$ and $d_1 = 3$, $\{\mathbf{S}^{(1)}_{t_1}\}$ is a set of 2-dimensional OA (matrices) and is also 5-periodic as the generating time series $\{x_t\}$. Choosing any other value of $d_1 \geq 1$ will output a period-5 series of OA.

Considering the previous series $\{\mathbf{S}^{(1)}_{t_1}\}$ of matrices, a series $\{\mathbf{S}^{(2)}_{t_2}\}$ of 3-dimensional OA, with $\mathbf{S}^{(2)}_{t_2} = \left(\mathbf{S}^{(1)}_{t_2}, \mathbf{S}^{(1)}_{t_2+\tau}, \cdots, \mathbf{S}^{(1)}_{t_2+(d_2-1)\tau}\right)$ can be constructed. From $\{\mathbf{S}^{(2)}_{t_2}\}$ can be constructed a series $\{\mathbf{S}^{(3)}_{t_3}\}$ of 4-dimensional OA with $\mathbf{S}^{(3)}_{t_3} = \left(\mathbf{S}^{(2)}_{t_3}, \mathbf{S}^{(2)}_{t_3+\tau}, \cdots, \mathbf{S}^{(2)}_{t_3+(d_3-1)\tau}\right)$. The process can be continued until the desired series $\{\mathbf{S}^{(M-1)}_{t_{(M-1)}}\}$ of M-dimensional OA is obtained. $\mathbf{S}^{(M-1)}_{t_{(M-1)}}$ is a $d_0 \times d_1 \times d_2 \times \cdots \times d_j \times \cdots \times d_{M-1}$ structure, with $0 \leq j \leq M-1$ and $d_0 = n$. We set $\tau = 1$ for the rest of the chapter.

In the previous example, only 5 permutations were obtained, because of the periodic nature of the time series. In the general case, the maximum number of permutations which can be derived from a given times series is $n!$. Considering this possible maximum number of permutations, the possible (maximum) number of ordinal matrices that can be derived from the series of ordinal patterns is $(n!)^{d_1}$. In the case of 2-dimensional series, each ordinal matrix is encoded using d_1 permutations similarly. In general, for a given time series of length T, the length of the resulting $A = n \times d_1 \times d_2 \times \cdots \times d_{M-1}$ series of OA, is

$N = T - (n + \phi - 1)$, where

$$\phi = \sum_{j=1}^{M-1} (d_j - 1),\ d_j > 0. \tag{4.2.1}$$

For a time series of length T, the length of the derived 1-D OA series constructed with an embedding dimension n is $N = T - n + 1$. Extending this calculation to multi-dimensional OA (M-D OA), the equivalent embedding dimension corresponding a M-D OA series can be given by

$$\rho = n + \phi. \tag{4.2.2}$$

In the ordinal pattern analysis approach, symbols are permutations (vectors) and are encoded using natural numbers while in the OA based analysis we are defining, symbols are arrays of permutations encoded using the same natural numbers. So, the entropy by the proposed approach can be seen as the Shannon entropy of M-D OA derived from the permutation series. The method combines both the ordering relations between values and the values themselves. The idea is to consider the diversity of the OA as well as their ranking in the time series. The ordering relation is used for determining the permutation series while the values of OA themselves are used for determining the entropy of M-D OA.

4.2.2 Quantization of ordinal arrays

The ordinal patterns (permutations) are defined as in the PE from a given time series $\{x_t\}$. In order to avoid misinterpretations, the delay times of samples and embedding vectors should be set as $\tau = 1$ and $\tau_0 = 1$, respectively [28]. Storing permutations is memory and computational time costly. To overcome such limitations, permutations are quantized and stored as real numbers. Indeed, each permutation P_k of length n is converted into a real number $z_k^{(0)}$ such that

$$z_k^{(0)} = \sum_{i=1}^{n} a^{-\frac{i}{i+1}} P_k(i), \tag{4.2.3}$$

where $1 < a \leq 2$ is chosen to avoid infinite values of $z_k^{(0)}$ for large n. If $\{P_k\}$ is an L-periodic time series, then $\{z_k^{(0)}\}$ is also a time series with the same period. This approach gives the possibility of considering large permutation orders. For a given value of a, the maximum value of n depends on the precision of the computer. In our algorithm, we fixed $a = 2$.

By replacing the permutations by real numbers, the ordinal matrix $\mathbf{S}_{t_1}^{(1)}$ becomes a vector $\mathbf{z}_{t_1}^{(1)}$ of real numbers. Although the order relations in the time series $\{x_t\}$ may differ from that in $\{\mathbf{S}_{t_1}^{(1)}\}$, the diversity of $\{P_k\}$ is preserved by the transform. Similarly to what we did for the series of permutations, each ordinal matrix $\mathbf{S}_{t_1}^{(1)}$ is replaced by a real number $z_{t_1}^{(1)}$ such that

$$z_{t_1}^{(1)} = \frac{1}{\sum_{i=1}^{d_1} a^{-\frac{i}{i+1}}} \cdot \sum_{i=1}^{d_1} a^{-\frac{i}{i+1}} \mathbf{z}_{t_1}^{(1)}(i), \tag{4.2.4}$$

where $\mathbf{z}_{t_1}^{(1)} = \left(z_{t_1}^{(0)}, z_{t_1+1}^{(0)}, \ldots, z_{t_1+(d_1-1)}^{(0)}\right)$. Applying once more the same process to $\{z_{t_1}^{(1)}\}$, the third dimension is reduced and $\{z_{t_2}^{(2)}\}$ is obtained. The process is to be continued until $\{z_{t_{(M-1)}}^{(M-1)}\}$, so that the whole M-D OA is converted into a scalar. The general term can then be given as:

$$z_{t_j}^{(j)} = \frac{1}{\sum_{i=1}^{d_j} a^{-\frac{i}{i+1}}} \cdot \sum_{i=1}^{d_j} a^{-\frac{i}{i+1}} \mathbf{z}_{t_j}^{(j)}(i),\ j \geq 1, \tag{4.2.5}$$

where $\mathbf{z}_{t_j}^{(j)} = \left(z_{t_j}^{(j-1)}, z_{t_j+1}^{(j-1)}, \ldots, z_{t_j+(d_j-1)}^{(j-1)}\right)$, t_j is a positive integer such that $0 \leq t_j \leq T-\rho$. Repeating the procedure for the whole series of M-D OA allows to obtain a 1-D time series.

4.2.3 Ordinal array entropy

Definition 4.2.1. The ordinal array entropy (OAE) is defined as the Shannon entropy of an information source whose alphabet elements are permutation-encoded OA. Let us assume $m = d_{M-1}$, $z_t = z_{t_{(M-1)}}^{(M-1)}$ and the equivalent embedding dimension s of the basic (M-1)-dimensional OA such that

$$s = n + \sum_{j=1}^{M-2} (d_j - 1). \tag{4.2.6}$$

The OAE of M-D OA is defined as

$$H_m(s) = -\sum p(z) \cdot \ln\left(p(z)\right), \tag{4.2.7}$$

where

$$p(z) = \frac{\#\{t \mid t \leq T - s - m + 1, z_t = z\}}{T - s - m + 2}. \tag{4.2.8}$$

In the particular case of 1-D OA series, the 1-D OA can be considered as an $n \times m$ OA with $m = 1$. The OAE is thus reduced to the PE, by the similarity between Eq. (2.2.2) and Eq. (4.2.8). The OA series is different from a 1-D series iff $n > 1$ and $m > 1$. In the case of a 2-D OA series, setting $z_t = z_{t_1}^{(1)}$, and $m = d_1$, the OAE is defined as:

$$H_m(n) = -\sum p(z) \cdot \ln\left(p(z)\right), \tag{4.2.9}$$

where

$$p(z) = \frac{\#\{t \mid t \leq T - n - m + 1, z_t = z\}}{T - n - m + 2}. \tag{4.2.10}$$

The z values are numeric conversions of permutation-encoded words, in a similar way to the way bit-encoded symbols are usually converted into decimal or real number values. The size of the OA alphabet being $(n!)^m$, the maximum value of $H_m(n)$ is equal to $m \ln(n!)$. Computing the Shannon entropy of OA allows us to better exploit the information provided by the ordinal patterns, hence to better approximate the complexity of the original time series as the number of OA increases as a power of m.

$H_m(s)$ is the OAE obtained by considering m-length vectors derived from an initial series of quantized $(M - 1)$-dimensional OA, whose equivalent embedding dimension is equal to s.

Theorem 4.2.1. *Let $\{x_t\}$ be real-valued period-L cycle time series of length T. If $L = q$, i.e no repeated value occurs in the basic period of $\{x_t\}$, and the delay time of the embedding vectors $\tau_0 = 1$, then the OAE does not depend on the embedding dimension m of the OA.*

Proof. In the case of 1-D OA, $\{x_t\}$ can be considered as a series of $n \times m$ OA with $m = 1$ ($s = n$). For $n = 1$, the patterns are reduced to the time series values. $\{x_t\}$ being L-periodic, there are L distinct patterns, also equal to the number of source symbols, each of them appearing with the same probability $p(\theta_i) = \frac{1}{L}$, $i = 1, 2, \ldots, L$, if the number of patterns explored is a whole multiple of L. The OAE in that case is equal to $H_m(s) = \ln(L)$.

For $n > 1$, we also showed in [28] that the set $\{\mathbf{x}_k\}$ of embedding vectors is L-periodic if the delay time of the embedding vectors is $\tau_0 = 1$. Indeed, as all the values in the basic period are assumed to be distinct, each embedding vector (pattern) is repeated after L steps: $\mathbf{x}_k = \mathbf{x}_{k+L}$. As the new patterns are embedding vectors $\mathbf{x}_k$, it follows that the number of distinct patterns is once more equal to the number of source symbols and all of them are equiprobable, depending on the observation length, hence $H_m(s) = \ln(L)$.

In the case of M-dimensional arrays ($M \geq 2$), it can also be shown that the period of the original time series is preserved in the series of ordinal arrays. Indeed, in that case the time series is assumed to be a series of vectors or arrays $\{\mathbf{x}_k\}$. Let us assume that $\{\mathbf{x}_k\}$ is a L-periodic series of n-length vectors ($n > 1$). The first quantized ordinal arrays series $\{z_{t_1}^{(1)}\}$ is derived from $\{\mathbf{x}_k\}$ by considering d_1-length ($d_1 > 1$) embedding vectors $\mathbf{z}_{t_1}^{(1)} = \left(\mathbf{x}_{t_1}, \mathbf{x}_{t_1+1}, \ldots, \mathbf{x}_{t_1+(d_1-1)}\right)$ of n-length vectors ($s = n$, $m = d_1$). We have already shown at the beginning of the proof that for any value of $n \in \mathbb{N}_{\geqq 1}$, $\{\mathbf{x}_k\}$ and $\{x_t\}$ have the same period. By the same principle, $\{\mathbf{z}_{t_1}^{(1)}\}$, hence $\{z_{t_1}^{(1)}\}$ and $\{\mathbf{x}_k\}$ also have the same period L. $z_{t_1}^{(1)}$ is the quantized value of the vector of scalars derived from $\{\mathbf{x}_k\}$ or simply a quantized ordinal matrix (2-D arrays). The number of distinct symbols in the basic period of $\{z_{t_1}^{(1)}\}$ being equal to L, its entropy is $H_m(s) = \ln(L)$.

Now let us consider the ordinal arrays series $\{\mathbf{z}_{t_2}^{(2)}\}$ derived from $\{\mathbf{z}_{t_1}^{(1)}\}$ and the corresponding quantized series $\{z_{t_2}^{(2)}\}$. $z_{t_2}^{(2)}$ is the quantized value of a vector of ordinal matrices (3-D arrays). The series $\{z_{t_2}^{(2)}\}$ is obtained by quantizing vectors of quantized ordinal matrices $\mathbf{z}_{t_2}^{(2)} = \left(z_{t_2}^{(1)}, z_{t_2+1}^{(1)}, \ldots, z_{t_2+(d_2-1)}^{(1)}\right)$. As the series of ordinal matrices is L-periodic without repeated values, there are only L distinct possible embedding vectors of ordinal matrices which repeats each one after L steps if $\tau_0 = 1$, hence $\{z_{t_2}^{(2)}\}$ is L-periodic and its entropy is $H_m(s) = \ln(L)$, with $s = n + d_1 - 1$ and $m = d_2$. By continuing the process, the same result is obtained for $\{z_{t_3}^{(3)}\}$ derived from $\{z_{t_2}^{(2)}\}$ and from step to step, the period of the series $\{z_{t_{(M-1)}}^{(M-1)}\}$ derived from $\{z_{t_{(M-2)}}^{(M-2)}\}$ is also equal to L. The M-D array transform is achieved after M successive transforms with embedding dimensions d_j, where $0 \leq j \leq M-1$ refers to the step index, with $d_0 = n$. As each transform step preserves the period of the corresponding input time series, from step to step the initial period is preserved in the whole M-D transform. Given that there is no repeated value in the basic period of the time series and the delay time of the embedding vectors is $\tau_0 = 1$, the entropy of the arrays series is also equal to $H_m(s) = \ln(L)$. It can then be concluded that the OAE of a L-periodic time series without repeated values in the basic period is equal to $H_m(s) = \ln(L)$, independently of the value of m, which finishes the proof. □

Remark 4.2.1. From the above proof, it appears that $H_n(1) = H_1(n)$. $H_n(1)$ is the OAE computed from the series of scalars by considering n-length embedding vectors, while $H_1(n)$ corresponds to the OAE computed from the series of n-length vectors by considering each

individual basic element (each n-length vector) as embedding vector. $H_m(s)$ is the Shannon entropy obtained by m-length embedding vectors from the initial $(M-1)$-dimensional OA series whose equivalent embedding dimension is s. If $m = 1$, the $(M-1)$-dimensional basic series remains unchanged, its dimension too. As a consequence, each Q-dimensional OA A can be considered as M-dimensional ($M > Q$), such that $A = d_1 \times d_2 \times \cdots \times d_Q \times d_{Q+1} \cdots \times d_M$, where $d_j > 1$, $\forall\, 1 \leq j \leq Q$ and $d_j = 1$, $\forall\, j > Q$.

4.3 Ordinal array complexity

4.3.1 Usefulness of M-dimensional ordinal arrays

When repeated values occur in the basic period ($L < q$), the OAE depends on their number as well as their ordering. We showed in [28] that to avoid such dependence, embedding vectors should include all the repeated values and at least one non-repeated value. It then follows in the case of 1-D time series that the embedding dimension $d_0 = n$ of the scalars should be chosen such that all the patterns are equiprobable. The equiprobability property can be observed for $n > R$ where R is the number of repeated values. In that case, the OAE is equal to $H_1(n) = \ln(q)$. Let us consider the following 3-periodic time series $\{x_t\} = \{a_0, a_1, a_0, a_1, a_2, a_0, a_1, a_0, a_1, a_2,\ a_0, a_1, a_0, a_1, a_2, \cdots\}$ for example. $\{x_t\}$ presents a time period $q = 5$ and is obtained by repeating its basic period $\mathrm{x}^0 = \{\mathrm{a}_0, \mathrm{a}_1, \mathrm{a}_0, \mathrm{a}_1, \mathrm{a}_2\}$. This basic period has $R = 2$ repeated values (namely a_0 and a_1). If $n = 2$, equiprobability cannot be obtained as the probability distribution is: $p_{(a_0,a_1)} = \frac{2}{5}$; $p_{(a_1,a_0)} = \frac{1}{5}$; $p_{(a_1,a_2)} = \frac{1}{5}$ and $p_{(a_2,a_0)} = \frac{1}{5}$. In this case, the OAE depends on m. For $n = 3$, the following equiprobability distribution is observed: $p_{(a_0,a_1,a_0)} = \frac{1}{5}$; $p_{(a_1,a_0,a_1)} = \frac{1}{5}$; $p_{(a_0,a_1,a_2)} = \frac{1}{5}$; $p_{(a_1,a_2,a_0)} = \frac{1}{5}$ and $p_{(a_2,a_0,a_1)} = \frac{1}{5}$. It can be easily verified that the same equiprobability property is obtained for all $n > 3$. This example thus confirms that choosing $n > R$ leads to an equiprobability distribution and that the OAE equals $H_1(n) = \ln(5)$. In the case where repeats are not reduced, the OAE may take different values, depending to the embedding dimension, although the time series is periodic.

Indeed, for some periodic time series, the number R of repetitions may be very large. Therefore, 2-D symbols can be considered for reducing their effect. Thus, there are two trivial solutions with two combined embedding dimensions n and $d_1 = m$ ($n > 1$ and $m > 1$):

the first one is to consider $n > R$ and any small value of m; and the second one is to consider large values of $m > R$ and a small value of n. Due to practical limitations, considering large values of embedding dimensions ($n = 20$ for example) is not interesting. It then follows that even considering 2-D symbols is not enough as we may require large values for the first and second dimensions n and m. Another simple possibility is to increase the dimension of the ordinal pattern so that the repetition is eliminated in the final series of ordinal patterns from which the entropy is evaluated. Let us for example consider an L-periodic time series with 16 consecutive identical values per period. The corresponding series of 9-order permutations ($n = 9$) is also L-periodic with 8 consecutive identity permutations per period. For such a repetition to be eliminated, we need to choose at least $n = 16$ or to convert the series of permutations into a 2-D time series with at least $d_1 = 8$. Let us consider $d_1 = 3$, then the resulting 2-D time series is periodic with 6 consecutive identical matrices per period. As the repetition persists, a third dimension is required. Let us consider $d_2 = 4$ for the third dimension. Then the series of ordinal arrays obtained is periodic with 3 consecutive identical values per period. The process then needs to be continued until the repetition is eliminated. A last dimension can then be considered with $d_3 = 3$. Finally, the series with no repeated value is a set of $\Theta = n \times D$ arrays, with $n = d_0$ and $D = d_1 \times d_2 \times d_3$ array. The possible number of distinct OA is then equal to $(n!)^{d_1 \cdot d_2 \cdot d_3}$. Replacing each permutation by a real number reduces the dimension of the $n \times D$ OA by one. So, each M-D OA can be reduced into a one dimensional vector by the successive quantization as described above, see Eqs. (4.2.3) and (4.2.5).

Considering M-D OA is equivalent to decomposing a ρ-length embedding vector into an $n \times D \times m$ embedding array, where $\rho = s + m - 1$ according to Eqs. (4.2.1) and (4.2.6), and $D = d_1 \times d_2 \times \cdots \times d_{M-2}$. Thus, this approach contributes to improving the statistical analysis of the time series by creating new criteria for discerning between patterns which initially look similar. As we showed previously in [67, 28], even when repetitions occur in the basic period of the time series ($L < q$), considering embedding dimensions $n > q$ is enough to get a q-periodic time series of the embedding vectors, hence an OAE which does not depend on m for regular dynamics.

Remark 4.3.1. According to theorem 4.2.1, the OAE of periodic dynamics does not depend

on the embedding dimension, if the latter is chosen such that all the patterns are equiprobable. Thus, we suggest using the difference between two OAE computed with two suitably chosen embedding dimensions as a complexity measure. With this approach, periodic dynamics are detected with a zero complexity, provided that equivalent embedding dimensions are chosen such to avoid any repetition in the resulting series of OA.

4.3.2 Ordinal array complexity

Definition 4.3.1. We define the ordinal array complexity (OAC) as:

$$h_{m_1,m_2}(s) = \frac{H_{m_2}(s) - H_{m_1}(s)}{m_2 - m_1}, \tag{4.3.1}$$

where m_1 and m_2 are two embedding dimensions applied to the series of $\Theta = n \times D$ OA, with $1 \leq m_1 < m_2$. The Shannon entropy $H_m(s)$ of the OA of size $\Theta \times m$ is computed from the series of OA of size Θ. The corresponding embedding dimension for the whole process is $\rho = s + m - 1$. The OAC is simply the differential of the OAE and measures the diversity of OA as the embedding dimension m of $(M-1)$-dimensional OA increases.

The OAC is zero for periodic dynamics if $s > q$. In the case of non-regular dynamics, considering two different embedding dimensions leads to two different distributions of probability, hence to $h_{m_1,m_2}(s) > 0$. The number of possible distinct $\Theta = n \times d_1 \times \cdots \times d_{M-2}$ OA which can be derived from a basic time series containing no repeated value is equal to $(n!)^{\Gamma}$, where Γ is such that

$$\Gamma = \prod_{j=1}^{M-2} d_j. \tag{4.3.2}$$

$D = d_1 \times d_2 \times \cdots \times d_{M-2}$ is the array of permutations. For a given time series converted into a series of size Θ OA, the possible number of $\Theta \times m$ OA is equal to $(n!)^{\Gamma \cdot m}$. It then follows that $0 \leq H_m(s) \leq \Gamma \cdot m \ln(n!)$, which also implies that $H_{m_1}(s) < H_{m_2}(s)$ for $m_1 < m_2$, hence $0 \leq h_{m_1,m_2}(s) \leq \Gamma \cdot \ln(n!)$. This number expresses the large diversity of OA which can be derived from the time series, whereas only $n! \ll (n!)^{\Gamma \cdot m}$ ordinal patterns can be described by the PE.

Remark 4.3.2. Considering the equivalent embedding dimension $\rho = s + m - 1$, the time series length should be such that $T \gg \rho!$. Similarly, considering the number of possible OA suggests that $T \gg (n!)^{\Gamma \cdot m}$. For $\Gamma > 1$ and $m > 1$, it is obvious that $\rho! \ll (n!)^{\Gamma \cdot m}$.

Taking into account the gap between the smallest value of the required time series length $(n!)^{\Gamma \cdot m}$ and the smallest time series length $\rho!$ due to the equivalent embedding dimension ρ, it turns out that the OAC may give satisfactory results even for data lengths smaller than the required one. Indeed, although the number of possible patterns is increased as a power of the basic number of ordinal patterns, the corresponding embedding dimension just slightly increases. For a given time series of length T, the length of the resulting $\Theta = n \times D$ ($D = d_1 \times d_2 \times \cdots \times d_{M-2}$) series of OA is equal to $N = T-(s-1)$. Let us consider $T = 100$, $n = 4$, and $D = 3 \times 3 \times 5$, the equivalent embedding dimension is $\rho = 12$ while the length of the OA time series is $N = 89$. The possible number of distinct OA is $(24)^{45} \cong 1.2868 \cdot 10^{62}$, which is too large as compared to $\rho! = 479001600$. It follows from this observation that by the OA approach, given a time series with fixed length, the number of patterns can be significantly increased, therefore improving the statistical analysis. Large embedding dimensions are necessary for detecting regular dynamics with large periods, but conversely require infinite data length for estimating the complexity of non-regular dynamics. So there is a compromise between the choice of the embedding dimension and the time series length, which appears to be well balanced by the OAC algorithm. The above OAC in definition 4.3.1 thus appears as an improvement of the ordinal KS algorithm [67].

4.3.3 Relationship between the OAC and the Kolmogorov-Sinai entropy

Let us define the parametric function $f_m : [0, \Gamma \ln(n!)]$ by:

$$f_m(s) = h_{m,m+1}(s), m \in \mathbb{N}_{\geqq 1}. \tag{4.3.3}$$

Considering the definition of the ordinal representation of the KS entropy given in [67], the relationship between the KS entropy and the OAC can be established as:

$$h_{KS} = \lim_{s \to \infty} \lim_{m \to \infty} f_m(s). \tag{4.3.4}$$

Eq. (4.3.4) can be seen as the generalized approximation of the ordinal representation of the KS entropy. For 2-D arrays ($\phi = 0$ and $s = n$), it is equivalent to:

$$h_{KS} = \lim_{n \to \infty} \lim_{m \to \infty} f_m(n) \tag{4.3.5}$$

which is the relation defined in [67].

The CPE $h_c(n)$ of order n was defined as the first element of the sequence $f_m(n)$, hence $h_c(n) = f_1(n) = h_{1,2}(n)$. Similarly, $f_1(s)$ can be seen as the conditional entropy of OA of size $\Theta = n \times D$. The CPE characterizes the diversity of successors of the given permutations ($\rho = n$) while the conditional entropy of OA characterizes the diversity of successors of a given OA ($\rho > n$).

Let us define the function family g_ρ of OAC of order ρ such that

$$g_\rho = \{f_m(s) | \rho = m + s - 1,\ 2 \leq s \leq \rho\}. \tag{4.3.6}$$

g_ρ is the set of parametric functions having the same embedding dimension ρ and whose elements are $g_\rho(s)$. $g_\rho(\rho)$ is the last element of the family g_ρ and is equivalent to $f_1(\rho)$, and thus corresponds to the CPE of order ρ. We call g_ρ the OAC of order ρ and its number of elements depends on the dimension of the OA.

4.4 Influence of the parameter setting

In Fig. 4.1 we show an example of OAC spectrum for the logistic map. The logistic map is commonly used as for almost all $r \in [0, 4]$ the KS entropy either coincides with the Lyapunov exponent if it is positive or is zero otherwise [51, 71]. Moreover, the Lyapunov exponent for the logistic map can be estimated rather accurately [65]. From Fig. 4.1, applying the OAC algorithm to the logistic map gives satisfactory results, compared to the CPE and the Lyapunov exponent (λ_{Lyap}).

We computed $f_7(9)$ for the OAC and $f_1(9)$ for the CPE, with $T = 4 \cdot 10^6$ as time series length. We observed that for the whole spectrum, $f_7(9)$ values are close to the Lyapunov exponent, taking zero values for all the regular dynamics corresponding to negative values of λ_{Lyap}. The fact that the Lyapunov exponent remains slightly greater than $f_7(9)$ confirms that the OAC uniformly tends to the KS limit as T tends to infinity. In contrast, the CPE is greater than the Lyapunov exponent for some values of r. It can also be observed that $f_1(9) = 0.063$ for $r = 3.602$, while it should be zero as the corresponding dynamics is regular, as indicated by the Lyapunov exponent value $\lambda_{Lyap} = -0.0085$. Given this observation let us investigate the impact of the OAC parameters.

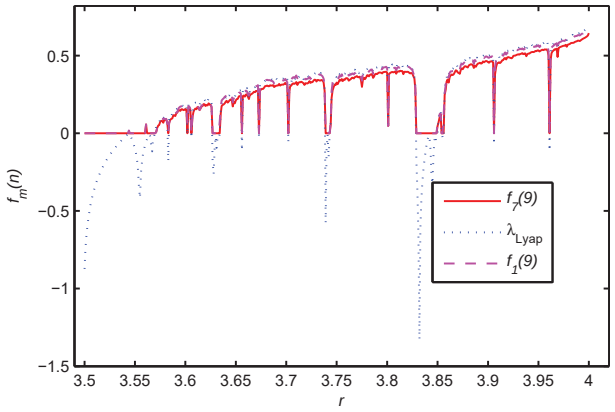

Figure 4.1: Comparison of the OAC with the CPE and the Lyapunov exponent, in the case of the logistic map.

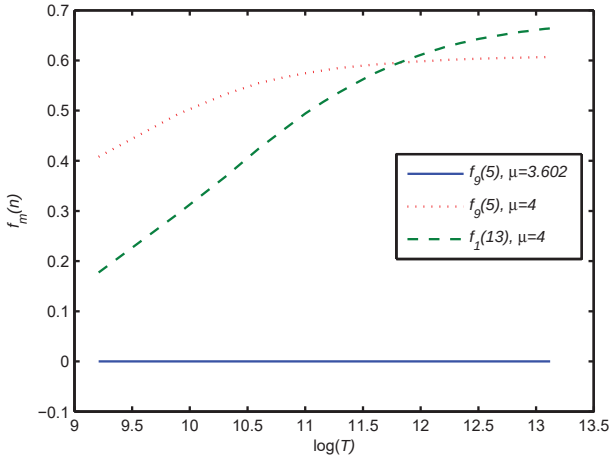

Figure 4.2: Dependence of the OAC and CPE results on the data length.

4.4.1 Dependence of the CPE and the OAC on T and n

We theoretically established that the OAC algorithm depends less on the observation time than the CPE. In Fig. 4.2 the behaviors of the OAC and the CPE for various values of T are plotted. The CPE values are computed from $f_1(13)$, while those of the OAC are obtained from $f_9(5)$. The time series length is incremented from $T = 10^4$ to $T = 5 \times 10^5$, by step size of $\Delta T = 10^4$. As can be observed from this figure, the result of the OAC does not depend on the time series length in the case of regular dynamics. We observed the same result for the CPE. However, for $r = 4$ corresponding to chaotic motion, the OAC is uniformly increasing

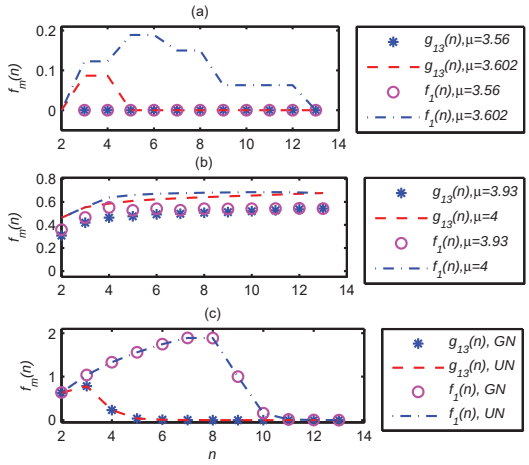

Figure 4.3: Relationship between the embedding dimension and the data length in the case of (a) regular dynamics, (b) non-regular dynamics and (c) noise.

from 0.4080 up to 0.6068, corresponding to $\Delta f_9(5) = 0.1988$; while the CPE is uniformly increasing from 0.1772 up to 0.6642, corresponding to $\Delta f_1(13) = 0.4869$. Therefore, for the same embedding dimension $\rho = n + m - 1 = 13$, the OAC remains closer to its limit value, even for $T \ll (5!)^9$, than the CPE which strongly requires that the condition $T \gg 13!$ is satisfied. Using OA as patterns thus helps to increase the number of distinct futures to be analyzed, hence to improve the statistical analysis. This observation is important as it confirms that the OAC algorithm may be suitable for the analysis of short length time series. Conversely, the CPE converges faster to the KS entropy than the OAC. This result may be due to the fact that the CPE combines two OAE computed from two time series with different dimensions: $H_1(\rho)$ computed from a 1-D time series and $H_2(\rho)$ computed from a 2-D time series.

We further investigated the impact of the embedding dimension on the complexity measure, but for $T = 10^6$. We have chosen three types of dynamics: regular dynamics ($r = 3.56$ and $r = 3.602$); chaotic dynamics ($r = 3.93$ and $r = 4$) and stochastic dynamics with uniform (UN) and Gaussian (GN) distributions, both obtained from MATLAB. The CPE was evaluated as $f_1(n)$ and the OAC as $f_m(n)$, where $m = 14 - n$ and $2 \leq n \leq 13$. The corresponding results are shown in Fig. 4.3. This figure shows that for regular dynamics, the CPE requires large embedding dimensions, independently of the data length; while the

OAC rapidly converges to zero, thus allowing the detection of regular dynamics with better accuracy than the CPE.

Considering chaotic dynamics, $f_1(n)$ for the CPE increases with the embedding dimension. Similarly, $g_{13}(n)$ for the OAC uniformly increases with the permutation order n. In that case, although the embedding dimension $\rho = 13$ remains constant, for $n > 2$ the required data length $(n!)^m$ becomes too large compared to T. Observing an increment of the complexity for the OAC just confirms that the pattern distribution strongly depends on m so that $f_m(n)$ is different from zero even when the time series length is too short compared to the required data length.

In the case of noise, it is observed that $f_1(n)$ is the same for both the uniform noise (UN) and the Gaussian noise (GN). Similarly, $f_m(n)$ is the same for the two distributions. However, the CPE increases with n for T such that $T \gg n!$, and decreases to zero when this condition is no longer satisfied. The same observation can be made for the OAC which increases as $T \gg (n!)^m$ and decreases to zero otherwise. These two results imply that the number of patterns rapidly increases in the case of noise and does not change anymore when the data length is smaller than the required value, thus leading to zero values for the complexity.

4.4.2 Impact of the equivalent embedding dimension ρ

For some values of the equivalent embedding dimension ρ, the detection result for regular dynamics may be wrong. An example is given for the logistic map with $r = 3.602$. For this dynamics, both the CPE and the OAC are giving a nonzero complexity for $\rho < 13$, independently of the time series length. Conversely, increasing the embedding dimension will require us to increase also the time series length T, otherwise the complexity will reduce. In practice, the data length sometimes cannot be extended and an appropriate compromise between the data length and the embedding dimension is required to avoid any confusion between regular and non-regular dynamics. While considering the requirement $T \gg \rho!$, one may set n and ϕ such that $(n!)^\phi < \rho!$. This particular possibility allows us to optimize the exploitation of the data length and justify the weak dependency of the OAC algorithm on the data length. Some example of combinations are given in Table 4.1.

In Fig. 4.4 the performances of the CPE and OAC algorithms are compared for a given

Table 4.1: Possible combinations (n, ϕ) for $\rho = n + \phi$ constant

$\rho = n + \phi$	2	3	4	5	6	7	8	9	10
$\phi \setminus n$	2	3	4	5	6	7	8	9	10
0	2!	3!	4!	5!	6!	7!	8!	9!	10!
1	-	$(2!)^2$	$(3!)^2$	$(4!)^2$	$(5!)^2$	$(6!)^2$	$(7!)^2$	$(8!)^2$	$(9!)^2$
2	-	-	$(2!)^3$	$(3!)^3$	$(4!)^3$	$(5!)^3$	$(6!)^3$	$(7!)^3$	$(8!)^3$
3	-	-	-	$(2!)^4$	$(3!)^4$	$(4!)^4$	$(5!)^4$	$(6!)^4$	$(7!)^4$
4	-	-	-	-	$(2!)^5$	$(3!)^5$	$(4!)^5$	$(5!)^5$	$(6!)^5$
5	-	-	-	-	-	$(2!)^6$	$(3!)^6$	$(4!)^6$	$(5!)^6$
6	-	-	-	-	-	-	$(2!)^7$	$(3!)^7$	$(4!)^7$
7	-	-	-	-	-	-	-	$(2!)^8$	$(3!)^8$
8	-	-	-	-	-	-	-	-	$(2!)^9$

data length ($T = 10^4$ samples), with varying equivalent embedding dimension ($7 \leq \rho \leq 13$). We fixed the permutation order at $n = 5$ for the OAC algorithm. The dynamics to be analyzed were generated from the logistic map with $r = 3.602$ corresponding to regular dynamics, and $r = 4$ corresponding to chaotic dynamics. From the results obtained, it appears that the OAC well balances the compromise between the embedding dimension and the data length. Indeed, the data length should be chosen such that $T \gg \rho!$. This requirement is not respected for both the OAC and the CPE. However, one observes in the case of the chaotic dynamics that the value of the complexity by the CPE (i.e $g_\rho(\rho)$) drastically reduces from $g_7(7) = 0.6643$ to $g_{13}(13) = 0.1788$ when $T < \rho!$; while the OAC result ($g_\rho(5)$) slightly decreases from $g_7(5) = 0.6114$ to $g_{13}(5) = 0.4091$. In the case of regular dynamics, the two algorithms behave similarly, although it should be pointed out that there is a smallest value of n ($n = 5$ for the dynamics corresponding to $r = 3.602$ as shown in Fig. 4.3(a)) under which the complexity of the regular dynamics is no longer zero, even for large values of ρ. It can then be concluded that the required data length for the OAC algorithm depends more strongly on the permutation order n than the equivalent embedding dimension. Hence, choosing $T \gg n!$ is enough for the OAC algorithm, while the CPE algorithm requires $T \gg \rho!$. Moreover, the permutation order required for detecting regular dynamics with a zero complexity is significantly reduced in the OAC algorithm, as compared to the CPE algorithm. Although the required embedding dimension ρ is the same for both the CPE and the OAC, it appears that its decomposition by the OA approach contributes to reducing the permutation order required by the CPE for efficient complexity

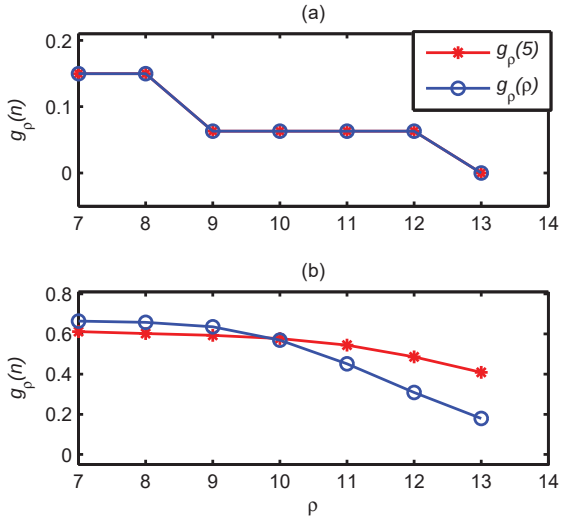

Figure 4.4: Impact of the embedding dimension on the OAC and the CPE algorithms: (a) regular dynamics and (b) non-regular dynamics.

measure, hence to reducing the required data length. These observations thus confirm that the OAC algorithm is more suitable than the CPE algorithm for discerning between regular and non-regular dynamics from a small data set.

Now let us evaluate the impact of the permutation order for fixed values of ρ. For this purpose, let us apply the OAC algorithm to the sine-circle map defined in Eq. (1.2.2). This system can exhibit both periodic dynamics with large periods and quasi-periodic dynamics, depending on the parameter setting. Indeed, we have already discussed the case of periodic dynamics with a small period, and have verified that there is a lower limit for the permutation order n under which the dynamics cannot be detected as regular. In practice, the period is not known a priori and the embedding dimension ρ or the permutation order n in some cases may be badly chosen. Due to the limited data length, it is also common to choose small embedding dimensions. It is well known that the KS entropy of a periodic dynamics is equal to zero. However, the CPE as well as the OAC in that case may output nonzero values, depending on the period of the underlying dynamics. Such a result is illustrated in Fig. 4.5. We considered for this example the sine-circle map with $x_0 = 0.4$ and $r = 0$. When Ω is a rational number, the map provides a periodic behavior [67]. We used $T = 10000$ as data length and Ω varying from 0 to 0.5, by step size $\Delta\Omega = 10^{-3}$. As shown

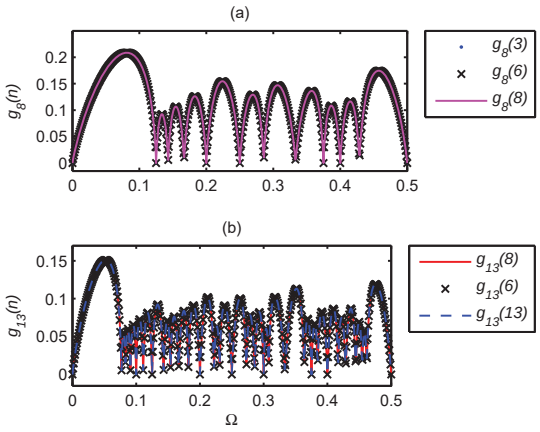

Figure 4.5: $g_\rho(n)$-spectrum of the sine-circle map (with $r = 0$), $T = 10^4$. The embedding dimensions are respectively (a) $\rho = 8$ and (b) $\rho = 13$.

in Fig. 4.5, all the three functions of the families g_8 and g_{13} behave similarly. We verified that g_8 and g_{13} go to 0 at rational numbers whose denominators are smaller than or equal to 8 and 13 respectively. For the set of Ω values considered in Fig. 4.5, g_8 goes to zero for $\Omega \in \{0, \frac{1}{8}, \frac{1}{5}, \frac{1}{4}, \frac{3}{8}, \frac{2}{5}, \frac{1}{2}\}$, while g_{13} goes to zero for $\Omega \in \{0, \frac{1}{10}, \frac{1}{8}, \frac{1}{5}, \frac{1}{4}, \frac{3}{10}, \frac{3}{8}, \frac{2}{5}, \frac{1}{2}\}$.

We also observed that $g_{13} < g_8$, which confirms that the complexity converges to zero as the embedding dimension tends to infinity. The result might become zero by increasing the permutation order n and the embedding dimension ρ. Unfortunately, a significant increment of these two parameters is not possible due to the limited data length. Another important observation can be made: for periodic dynamical systems g_ρ depends only on the embedding dimension ρ for $n \ll L$, and therefore slowly converges to zero. We verified this observation for all the elements of the families g_8 and g_{13}. Taking into account this observation, it can be conjectured that the difference of two parametric functions $f_m(s)$ belonging to the same family g_ρ is equal to zero; which allows to easily detect regular dynamics with large periods.

In order to confirm the non-dependence of the behavior of g_ρ on the permutation order n in the case of regular dynamics, let us apply the OAC algorithm to the sine-circle map, but with $\Omega = \frac{-1+\sqrt{5}}{2}$ and $x_0 = 0.5$. For this value of Ω, the system is known to exhibit quasi-periodic dynamics for $0 \leq r \leq 1$ [2, 27]. We also considered sequences of length $T = 10^4$ samples and the control parameter $0 \leq r \leq 2.5$ varying by step size $\Delta r = 0.01$. The corresponding result is shown in Fig. 4.6 from where it is confirmed that g_ρ does not

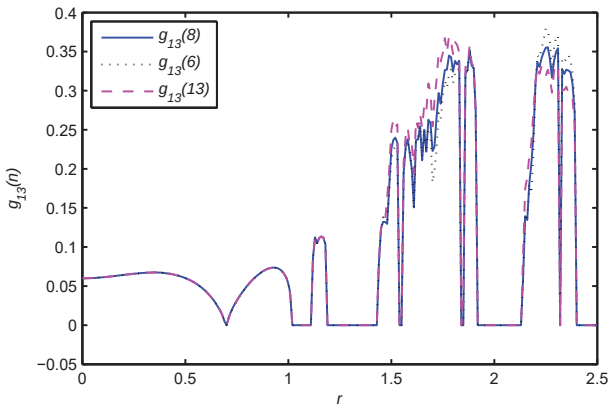

Figure 4.6: $g_\rho(n)$-spectrum of the sine-circle map with $\Omega = \frac{-1+\sqrt{5}}{2}$. The embedding dimensions is $\rho = 13$ and $T = 10^4$.

depend on n in the case of regular (periodic and quasi-periodic) dynamics.

4.4.3 Useful array dimension

The above simulation results confirm that large embedding dimensions are still required. Only dynamics whose periods are less than the equivalent embedding dimension ρ are surely detected with a zero complexity. Although increasing the embedding dimension also requires an increase of the data length, technically there is no limiting value for n while using the OA approach unlike for the CPE algorithm described in [67]. Let us consider that ordinal arrays are made of two main parts: the radial part described by the permutation length n and the angular part described by the array $\Phi = D \times m$ whose embedding dimension is equal to ϕ. According to the definition of the OAC, two distinct angular arrays $D = d_1 \times d_2 \times \ldots \times d_M$ and $D' = d'_1 \times d'_2 \times \ldots \times d'_{M'}$ with $d_i \neq d'_i$, $M' \geq M$ and $\sum_i^M d_i = \sum_j^{M'} d'_j$ provide the same OAC for a given time series. This property of the OAC implies that there is no need to consider more than three-dimensional arrays.

We showed in chapter 2 how to deal with the ordinal matrix transform where embedding vectors where replaced by the largest slope of the corresponding permutations. The extension made in this chapter transforms the permutation into a scalar value, instead of the largest slope. While considering $n = 2$, we can easily verify that the two approaches are equivalent. This observation implies that the OAC can be equally applied to the detection of SNA and quasi-periodic dynamics. However, as we showed in chapter 2, this detection

requires some prior knowledge of the system under investigation. So, the use of the OAC also will not provide complete information on the nature of the underlying data series. Indeed, the entropy measure gives us the information related to the distribution of the distinct ordinal arrays (symbols) for a given embedding dimension ρ, but not on their evolution in terms of ρ. The OAC results presented thus behave like the number Λ of distinct symbols is known a priori for a given ρ. As it is not the case, we suggest to investigate the behavior of Λ in terms of ϕ to get complementary information on the nature of the time series.

4.5 Asymptotic behavior of Λ in terms of the embedding dimension

Theoretically, the largest number of distinct arrays which can be obtained for a given embedding dimension $\rho = n + \phi$ is $\Lambda_0 = (n!)^{\Gamma m}$. However, depending on the nature of the data series and the observation length T, the effective number Λ of symbols obtained is such that $\Lambda \leq \Lambda_0$. For an L-periodic ($L = q$) dynamics for example, we showed (see theorem 4.2.1) that Λ is bounded by an upper limit which is equal to L. In that case, Λ does not depend on T as long as $T > L$. This requirement is not always known a priori and the behavior of Λ in terms of ρ for fixed values of T therefore can provide some information on the nature of the time series.

4.5.1 Behavior of Λ in terms of the angular embedding dimension ϕ

By extending the dimension of the angular arrays while maintaining its embedding dimension ϕ unchanged, Γ increases and Λ also should increase. Consequently, the OAC should vary as well. However, we verified that Λ and the OAC vary only when ϕ and n are modified. This observation implies that the OAC as described is not sensitive to the size of the angular arrays, but only to their equivalent embedding dimension ϕ. As a consequence, the upper limit of Λ is reduced to $\Lambda_0 = (n)^{\phi+1}$, which is far less than the theoretical value $(n!)^{\Gamma m}$. Therefore, the useful data length required for an efficient evaluation of the complexity of the time series is also reduced to $T > (n!)^{\phi+1}$. Fig. 4.7 shows some example of behaviors of Λ for the particular cases corresponding to periodic, quasi-periodic, chaotic and stochastic data. The periodic and chaotic dynamics were generated using the logistic equation with

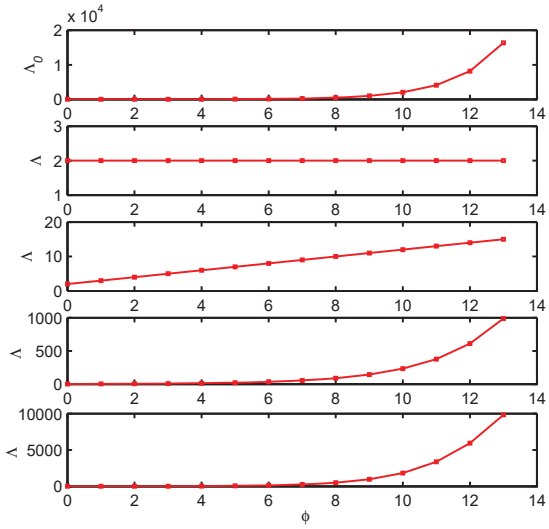

Figure 4.7: Particular behavior of Λ in terms of ϕ. From top to bottom are shown the behavior of Λ for Λ_0, periodic, quasi-periodic, chaotic and stochastic data. We set $T = 5 \times 10^4$, $n = 2$ and $0 \leq \phi \leq 13$

Table 4.2: Behavior of Λ in terms of ϕ for particular dynamics, $n = 2$: Λ_{1-4} for respectively the periodic, quasi-periodic, chaotic and stochastic data series

ϕ	0	1	2	3	4	5	6	7	8	9	10	11	12	13
Λ_0	2	4	8	16	32	64	128	256	512	1024	2048	4096	8192	16384
Λ_1	2	2	2	2	2	2	2	2	2	2	2	2	2	2
Λ_2	2	3	4	5	6	7	8	9	10	11	12	13	14	15
Λ_3	2	3	5	8	13	21	34	55	89	144	233	377	610	987
Λ_4	2	4	8	12	32	64	128	254	500	964	1827	3377	5945	9824

$r = 3.56$ and $r = 4$ respectively, and $x_0 = 0.4$. The quasi-periodic dynamics was generated from the sine-circle map with $r = 0$, $\Omega = \frac{-1+\sqrt{5}}{2}$ and $x_0 = 0.5$; while the stochastic sequence corresponds to white noise with a Gaussian distribution. From this figure, it is evident that Λ is bounded by $\Lambda_0 = (n)!^{\phi+1}$ for all the four dynamics. The corresponding values are tabulated in Table 4.2. In the particular case of the chaotic dynamics, Λ corresponds to the sequence of the Fibonacci numbers. One can also observe that in the case of the stochastic data series, Λ is close to Λ_0.

4.5.2 Modeling of the behavior of Λ as a function of ρ

While looking at Fig. 4.7, one can observe three types of behaviors for Λ: constant, linear and exponential behavior. All these behaviors of Λ as shown in Fig. 4.7 are bounded by Λ_0 and depend on the dynamics under investigation. It then follows from this observation that each type of dynamics can be characterized by the evolution rule of Λ compared to Λ_0. For this purpose, we suggest modeling the behavior of Λ in terms of ϕ so that all the above three behaviors are taken into account. For periodic dynamics, $\Lambda(\phi) = a_0$ where $n \leq a_0 \leq L$ is related to the period of the underlying dynamics. In the case of quasi-periodic dynamics, $\Lambda(\phi) = n + \phi$. By combining the periodic and the quasi-periodic dynamics, the modeling function can be expressed as $\Lambda(\rho) = \mu \cdot \rho^{\alpha}$, given that $\rho = n + \phi$. For this modeling function, $\mu = a_0$ and $\alpha = 0$ for periodic dynamics; for quasi-periodic dynamics, $\mu = \alpha = 1$. The exponential behavior can also be modeled as an attenuated value of Λ_0, i.e $\Lambda(\phi) = \mu \cdot (n!)^{\lambda \cdot (\phi+1)}$, where $\lambda \leq 1$. This function can also be written in terms of ρ, which affects only the scaling of μ. The reduction of the value of the scaling factor λ thus introduced by the use of ρ can be balanced by changing the basis of the exponential function: instead of $n!$, one may use 2 for example. By combining the linear and exponential models, the modeling function of Λ becomes

$$\Lambda(\rho) = \mu \cdot \rho^{\alpha} \cdot b^{\lambda \cdot \rho}, \tag{4.5.1}$$

where $\mu \in \mathbb{R}_{>0}$ is the periodicity index, $\alpha \in \mathbb{R}$ is the quasi-periodicity index, $\lambda \in \mathbb{R}$ the index of non-regularity and $b \in \mathbb{R}_{\geq 2}$ the exponential basis.

By considering the behavior of $\Lambda = \Lambda_0$, which corresponds to a purely random source, one can easily determine the limits of μ, α and λ by solving the equation

$$\mu \cdot \rho^{\alpha} \cdot b^{\lambda \cdot \rho} = \Lambda_0. \tag{4.5.2}$$

We solved this equation and found

$$\begin{cases} \mu = (n!)^{1-n} \\ \alpha = 0 \\ \lambda = \frac{\ln(n!)}{\ln(b)}. \end{cases} \tag{4.5.3}$$

In a purely random source, $\lim_{n\to\infty} \mu = 0$, $\alpha = 0$ and $\lambda = \frac{\ln(n!)}{\ln(b)}$. Solving the same equation

in the case of quasi-periodic dynamics with $\Lambda(\rho) = \rho$, we found

$$\begin{cases} \mu = 1 \\ \alpha = 1 \\ \lambda = 0. \end{cases} \tag{4.5.4}$$

For periodic dynamics, the solution is trivial

$$\begin{cases} \mu = a_0 \\ \alpha = 0 \\ \lambda = 0, \end{cases} \tag{4.5.5}$$

with $n \leq a_0 \leq L$. Between the solutions presented above, there are many intermediate combinations of μ, α and λ which depend on the nature of the underlying dynamics. The appropriate solution $\psi = (\mu, \alpha, \lambda)$ of Eq. (4.5.1) in that case can be determined using least mean square interpolation, with $f_1(\rho) = 1$, $f_2(\rho) = \ln(\rho)$ and $f_3(\rho) = \rho$ as the three basis functions. The values obtained are accurate as $T \to +\infty$, hence the usefulness of the asymptotic behavior. In the case for example of the particular dynamics in Fig. 4.7, we found respectively $\psi_1 = (2, 0, 0)$, $\psi_2 = (1, 1, 0)$, $\psi_3 = (0.7647, -0.057, 0.7035)$, and $\psi_4 = (0.4126, 0.4386, 0.8693)$ for the periodic, quasi-periodic, chaotic and stochastic sequence. λ is close to its upper limit $\lambda_0 = \frac{\ln(n!)}{\ln(b)}$ as the dynamics is complex. The largest complexity value which can be estimated by this model is given in Eq. (4.5.3). Similarly to the Lyapunov exponent, we expect that regular dynamics are characterized by $\lambda \leq 0$. In this way, periodic dynamics with large periods as well as SNA may be easily detected as regular. It should be pointed out that λ is bounded by 1 if the exponent basis is set as $b = n!$. For any other basis less than $n!$, the upper limit of λ is greater than 1.

4.5.3 Example of detection and classification of complex regular dynamics

We call complex regular dynamics those for which the period is too large compared to practical embedding dimension, such as SNA and quasi-periodic dynamics. Let us consider two well known examples for which most of the time series analysis algorithms, especially ordinal pattern-based algorithms, fail to detect the exhibited dynamics as regular: the circle map whose detection results by the OAC algorithm are presented in Fig. 4.5 and the forced GOPY map whose equation is

$$x_{t+1} = 2r \tanh(x_t) \cos(2\pi y_t) + \epsilon \cos(2\pi (y_t + \varphi)), \tag{4.5.6}$$

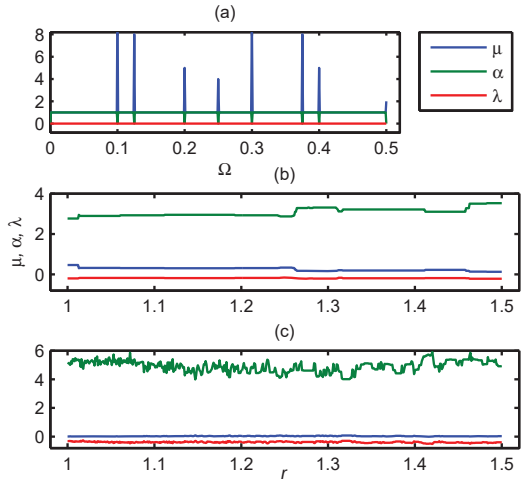

Figure 4.8: Detection of SNA and quasi-periodic dynamics: (a) sine-circle map with $r = 0$, $x_0 = 0.4$, $0 \leq \Omega \leq 0.5$, $n = 2$ and $8 \leq \phi \leq 18$; (b) forced GOPY map with $\varphi = 1/8$, $x_0 = 0.1$, $\epsilon = 0$, $1 \leq r \leq 1.5$, $n = 2$ and $4 \leq \phi \leq 14$; (c) forced GOPY map as in (b), except for $\epsilon = 0.02$. We set $T = 2 \times 10^4$ for all the dynamics.

with y_t behaving as in Eq. (2.5.1). It was shown that the GOPY map exhibits SNA for $r > 1$ and $\epsilon = 0$, and quasi-periodic behaviors for $r > 1$ and $\epsilon > 0$ [33, 39, 56]. The results in Fig. 4.8 confirm that, using a small amount of data and relatively small embedding dimensions, the index of non-regularity λ efficiently detect SNA, quasi-periodic and other dynamics with large periods as regular. In the case of the circle map, this result contrasts with the one obtained with the OAC for which only dynamics whose the period was less than ρ were detected with a zero complexity. There now remains the problem related to the classification of regular dynamics into periodic, quasi-periodic and SNA. This problem may be solved by analyzing the behavior of μ and α for $\lambda \leq 0$. In the case of the GOPY map, both cases known as SNA and quasi-periodic are well detected as regular. In order to make clear distinction between SNA and quasi-periodic dynamics, the behavior of μ and α in Fig. 4.8(b-c) need to be analyzed in detail.

$\psi_0 = (\mu = 1, \alpha = 1, \lambda = 0)$ can be seen as the transition point between periodic, quasi-periodic and SNA. In SNA and quasi-periodic dynamics, there is no period, therefore μ is no longer an integer value greater than 1. Moreover, the behavior of Λ can be more complex than linear, depending to the number of incommensurable frequencies combined, but it does not behave exponentially. This smooth nonlinear increase of Λ implies $\alpha > 0$ and $\lambda \leq 0$ for

SNA and quasi-periodic dynamics. One can then conjecture on the signature of SNA and quasi-periodic dynamics as $\psi_R = (\mu \notin \mathbb{N}, \alpha > 0, \lambda \leq 0)$. The dynamics is quasi-periodic when α is large. In the case of periodic dynamics, a period greater than or equal to 1 exists. Furthermore, the behavior of Λ for such a dynamics is constant (depending to the embedding dimension), which implies $\alpha = 0$. As some errors may occur due to the choice of ρ compared to the period of the underlying dynamics, one may observe some behaviors looking like quasi-periodic dynamics and SNA. Thus, the periodic behavior is characterized by $\psi_P = (\mu \geq 1, \alpha = 0, \lambda = 0)$. The complexity of a regular dynamics increases as $\mu \to 0$, $\alpha \to +\infty$ and $\lambda \to -\infty$. A dynamics is as stochastic when $\mu \to (n!)^{1-n}$, $\alpha \to 0$ and $\lambda \to \frac{\ln(n!)}{\ln(b)}$.

The above classification will be verified on other well known systems in the next section. Nonetheless, it should be noticed that this approach performs well with dynamics with large periods and strongly chaotic data, and should be used as a complementary tool for the OAC whose efficiency for complexity measure has been shown in this chapter. In the case of low dimensional systems, weakly chaotic dynamics are detected as regular and requires large values of n to be detected as chaotic. This low sensitivity of the algorithm to weakly chaotic data proves its high robustness against noise. In practice, most of the systems are high-dimensional and real-world data are noise contaminated, the robustness of the algorithm against noise constitutes an advantage for its applicability to experimental data. Thus, the system is as complex (high dimensional) as for a given T, the admissible value of n is small. For stochastic data for example, as the number of OA is close to $(n!)^{\phi_{max}+1}$, it is difficult to consider $n > 2$ for $\phi_{max} \geq 10$, thus attesting their high dimensionality.

4.6 Application of OA-based algorithms to the detection of SNA

In this section, we combine, whenever it is necessary, all the algorithms previously described for the characterization of quasi-periodically forced systems. We intend to clearly identify SNA, quasi-periodic dynamics and tori. For this purpose, we used well known systems which have been already described.

4.6.1 Detection of route to SNA in the forced GOPY map

The GOPY map whose equation is described in Eq. (4.5.6) constitutes a good candidate for the validation of our algorithms as it exclusively exhibit complex regular dynamics. The GOPY map is known to exhibit SNA for $r > 1$ and $\epsilon = 0$, and quasi-periodic behaviors for $r > 1$ and $\epsilon > 0$ [33, 56]. In this section, we compute the OAC, the ME as well as the indices of regularity (μ and α) and non-regularity (λ). These indicators are compared to the Lyapunov exponent for efficient decision making. From this comparison also are deduced indications on the parameter setting of each of the underlying algorithms. In Fig. 4.9 are depicted the Lyapunov spectrum and the spectra of OA growth indices μ, α and λ and the ME. These spectra are obtained for $T = 2 \times 10^4$ and $n = 3$, $4 \leq \phi \leq 13$ for the OA approach and $n = 200$, $\tau_0 = 10$ for the ME algorithm.

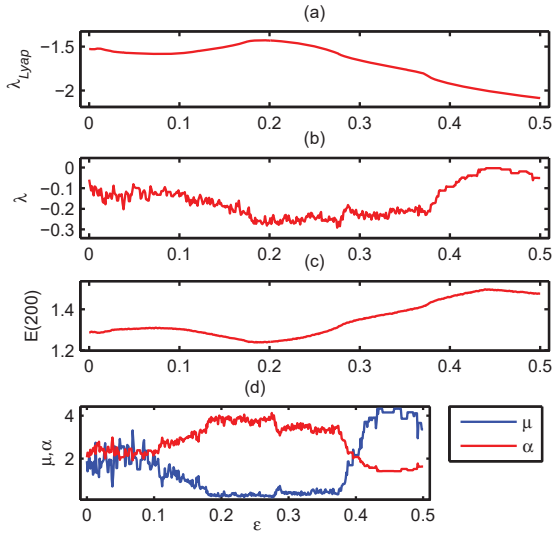

Figure 4.9: SNA detection spectra for the GOPY map with $r = 1.5$ and $0 \leq \epsilon \leq 0.5$: (a) Lyapunov exponent (λ_{Lyap}), (b) index of non-regularity (λ), (c) matching energy (ME) and (d) periodicity index (μ) and quasi-periodicity index (α). We set $T = 2 \times 10^4$, $\tau_0 = 10$ and $n = 200$ for the matching energy; $n = 3$ and $4 \leq \phi \leq 13$ for the OA growth indices.

The reference for the validation of our algorithms is the Lyapunov exponent. While comparing it with λ, it comes that both spectra behave similar in terms of the detection result: $\lambda_{Lyap} \to -\infty$ as the dynamics is regular whereas $\lambda \to 0$ as the dynamics is regular. So, an increase of λ_{Lyap} corresponds to a decrease of λ. For $0 \leq \epsilon \leq 0.5$ and $r = 1.5$, the

system is progressively moving from SNA ($\epsilon = 0$) to a smooth torus ($\epsilon \geq 0.4$). Between these two extreme behaviors, the system exhibits a quasi-periodic dynamics (wrinkle torus) and the transition between these three regions are quite difficult to establish while looking at the Lyapunov spectrum. Both λ and λ_{Lyap} indicate around $\epsilon = 0.37$ an edge which can be interpreted as the beginning of the smooth torus, while the transition between SNA and wrinkle torus may occur around $\epsilon = 0.1$. However, a contradiction is observed on the ME spectrum. Indeed, the ME indicates a complex dynamics as the ME is large. While comparing its spectrum with λ_{Lyap}, this interpretation should be reconsidered as the largest ME corresponds to the smallest λ_{Lyap}. We then conclude that the ME algorithm is not suitable for the analysis of quasi-periodically forced systems. Nonetheless, by reversing the ME spectrum, it is observed that it perfectly matches the behavior of the spectrum of the Lyapunov exponent, and thus confirms the above transition between SNA and quasi-periodic dynamics.

Now considering the μ and α spectra, it appears that the transition between SNA and quasi-periodic dynamics once more occurs around $\epsilon = 0.1$ as previously observed. In addition to the transition detection, combining μ and α allow to qualitatively characterize SNA, wrinkled tori (quasi-periodic) and smooth tori. However, it still remains difficult to clearly state which combination (μ, α) corresponds to SNA or quasi-periodic dynamics. Nevertheless, the combination of μ and α improves the detection of transitions in the system behavior. For this example, the couple (μ, α) shows that the transition between wrinkled tori and smooth tori approximately occurs at $\epsilon = 0.4$ where $\mu > \alpha$, and that $\epsilon = 0.37$ is still a wrinkled torus where the transition process begins.

Form the above results, it appears that the Lyapunov exponent, the matching energy and the index of non-regularity only allow to detect transitions (need for spectrum or varying control parameter) in the dynamics of a given system, while the regularity indices give the possibility to get more details on the nature of a single time series: the dynamics can be dominated by the periodic behavior ($\mu > \alpha$) or the quasi-periodic behavior ($\mu < \alpha$). Applying the OAC algorithm for determining the complexity of the system also allows only to detect structural changes in the whole dynamics of the underlying system as shown in Fig. 4.10. One can observe that the behavior of the spectrum of the OAC approximates that of the Lyapunov exponent as ϕ increases. Such a result is justified by the fact that the diversity of the set of OA increases as ϕ is large. For small values of ϕ, all the dynamics

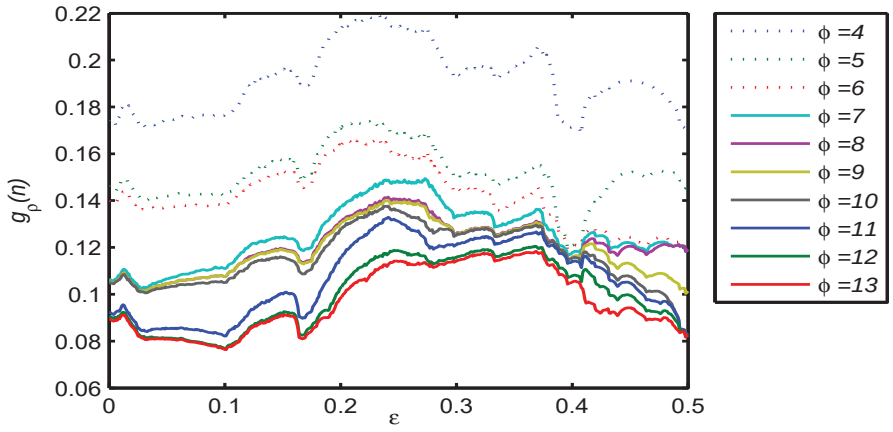

Figure 4.10: OAC for SNA detection spectra in the GOPY map with $r = 1.5$ and $0 \leq \epsilon \leq 0.5$. We set $T = 2 \times 10^4$, $n = 3$ and $4 \leq \phi \leq 13$ ($7 \leq \rho \leq 17$).

output almost the same number of ordinal patterns and no difference can be established between them as their distribution of OA are looking similar. As a consequence, transitions between closely behaving dynamics cannot be well appreciated. This may be the case for the CPE for which $\phi = 0$. Therefore, satisfactory result cannot be obtained by the CPE unless n is increased, as it is not possible to increase ϕ. Similarly, PE requires large values of n for it to detected regular dynamics. We verified that for the OAC and OA growth indices to be well evaluated, n and ϕ should be chosen such that $\Lambda_{max} < \frac{T}{20}$, where Λ_{max} corresponds to the largest value ϕ_{max} of ϕ. Furthermore, the value of n should be large as possible, in order to increase the diversity of the set of Λ.

We now turn to the case $\epsilon = 0$ for which the system exhibit SNA for all $r > 1$, the corresponding OA growth indices are depicted in Fig. 4.11. The couple (μ, α) clearly describes the bifurcation in the route to SNA whereas the Lyapunov exponent only shows a decreasing line with a constant slope. Indeed, (μ, α) shows that the system is progressively moving from SNA to quasi-periodic motions (at $r = 1.5$ and $\epsilon > 0$ starts the transition to quasi-periodic dynamics). In Fig. 4.12 are shown the corresponding OAC. Once more, the OAC spectra show that there are some variations in the system dynamics while moving from SNA to quasi-periodic dynamics, but not as much detailed as in the (μ, α) diagram.

The behavior of (μ, α) depends on the parameter setting. Choosing large values of n requires a large observation time; while choosing too small values of n for example, even if

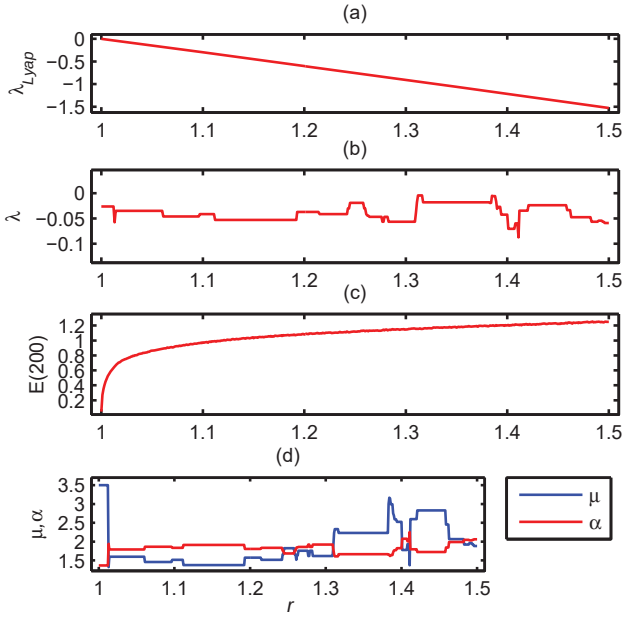

Figure 4.11: OA growth indices spectra for SNA detection in the GOPY with $\epsilon = 0$ and $1 \leq r \leq 1.5$. We set $T = 2 \times 10^4$, $n = 3$ and $4 \leq \phi \leq 13$ ($7 \leq \rho \leq 17$).

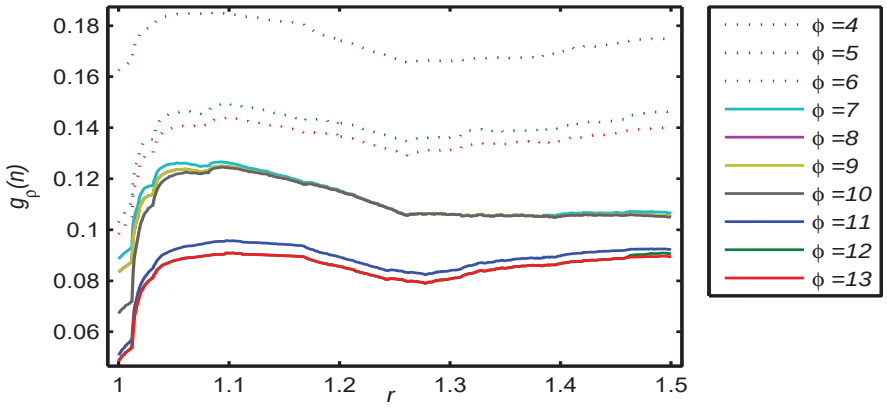

Figure 4.12: OAC for SNA detection spectra in the GOPY map with $\epsilon = 0$ and $1 \leq r \leq 1.5$. We set $T = 2 \times 10^4$, $n = 3$ and $4 \leq \phi \leq 13$ ($7 \leq \rho \leq 17$).

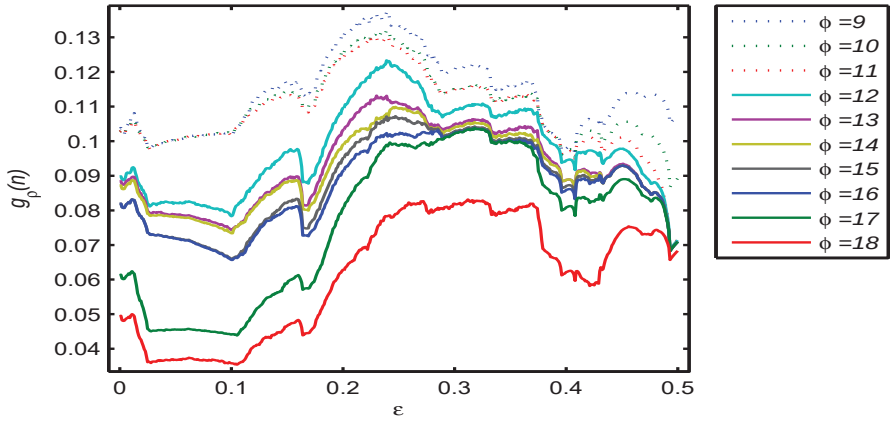

Figure 4.13: OAC for SNA detection spectra in the GOPY map with $r = 1.5$ and $0 \leq \epsilon \leq 0.5$. We set $T = 2 \times 10^4$, $n = 2$ and $9 \leq \phi \leq 18$ ($11 \leq \rho \leq 20$).

ϕ is large, may lead to some misinterpretations as it can be observed on Fig. 4.13 where the OAC spectrum increases whereas the Lyapunov exponent decreases for $\epsilon > 0.4$. This false parameter setting also reduces the ability of (μ, α) to detect changes in the system behavior, as shown on Fig. 4.14.

However, the above results may be improved by increasing the observation time. Indeed, one should consider the asymptotic behavior of the OA growth indices for an efficient characterization of the dynamics analyzed. By considering for example the dynamics in the GOPY map characterized by $r = 1.5$ and $\epsilon = 0.42$, and setting $n = 2$, $11 \leq \phi \leq 19$ and $T = 10^6$, the values of the OA growth indices are $\mu = 0.1957$, $\alpha = 3.3923$ and $\lambda = -0.2750$ indicating that the dynamics is regular; while the same dynamics outputs $\mu = 5.5421$, $\alpha = 1.0916$ and $\lambda = 0.0064$ for $T = 2 \times 10^4$, thus indicating that the dynamics is chaotic.

4.6.2 Impact of T: Discerning between SNA and tori

The number Λ of symbols strongly depends on T in the case of random sources and does not in the case of periodic dynamics, provided that $T > q$. In the case of quasi-periodic dynamics, it may or not strongly depend on. The main question is to know which one of the two types of dynamics, SNA and tori, depends more on T. Such an investigation may help for discerning between SNA and quasi-periodic dynamics. We then considered the GOPY map for $r = 1.5$ and $\epsilon = 0$ and $\epsilon = 0.4$. For these two values of ϵ, the system exhibits

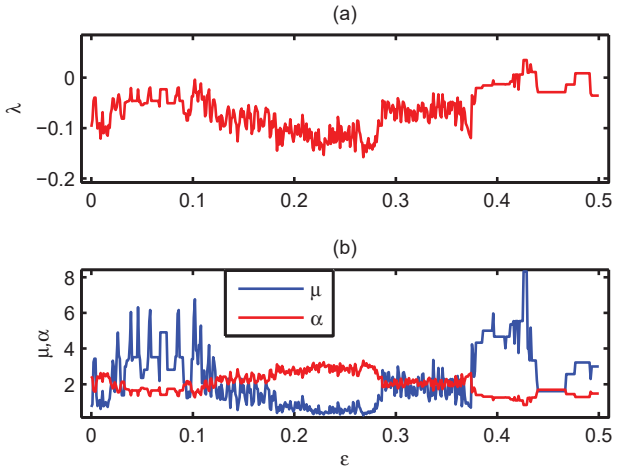

Figure 4.14: OA growth indices spectra for SNA detection in the GOPY with $r = 1.5$ and $0 \leq \epsilon \leq 0.5$. We set $T = 2 \times 10^4$, $n = 2$ and $9 \leq \phi \leq 18$ ($11 \leq \rho \leq 20$).

respectively an SNA and a quasi-periodic dynamics. We consider $10^4 \leq T \leq 10^5$ with step size $\Delta T = 10^4$, $n = 2$ and $4 \leq \phi \leq 13$. Fig. 4.15 shows the corresponding results for the two dynamics. It clearly appears that SNA depend more on the time series length than quasi-periodic dynamics.

Now computing $\Delta\mu = |\mu_1 - \mu_2|$, $\Delta\alpha = |\alpha_1 - \alpha_2|$ and $\Delta\lambda = |\lambda_1 - \lambda_2|$ for two distinct time series lengths $T_1 = 2 \times 10^4$ and $T_2 = 10^5$, let us determine the nature of the dynamics exhibited by the GOPY map for the two previous parameter settings: $r = 1.5$ and $0 \leq \epsilon \leq 0.5$, and $1 \leq r \leq 1.5$ and $\epsilon = 0$. In the first case, the system is continuously moving from SNA to quasi-periodic dynamics, as $\Delta\mu$, $\Delta\alpha$ and $\Delta\lambda$ are continuously moving from a positive value to zero. This result is consistent with the one presented in [39]. In the second case, the system exhibits SNA as $\Delta\mu$, $\Delta\alpha$ and $\Delta\lambda$ are positive, also confirming the result predicted in the literature [39]. According to Fig. 4.15, one may conclude that for given values of n and ϕ, OA growth indices μ, α and λ asymptotically converge to their respective limit values μ_0, α_0 and λ_0 faster for quasi-periodic dynamics than SNA. In practice, we suggest to choose n and ϕ such that $\Lambda_m = \Lambda(\phi_{max}) \ll T$, where ϕ_{max} is the largest value of ϕ.

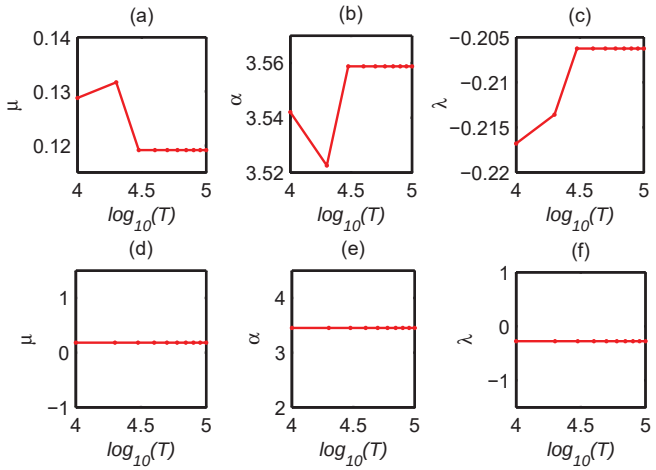

Figure 4.15: Dependance on T of SNA ($r = 1.5$ and $\epsilon = 0$) and quasi-periodic dynamics ($r = 1.5$ and $\epsilon = 0.4$) OA growth indices. We considered $10^4 \leq T \leq 10^5$ by step size $\Delta T = 10^4$, $n = 2$ and $4 \leq \phi \leq 13$.

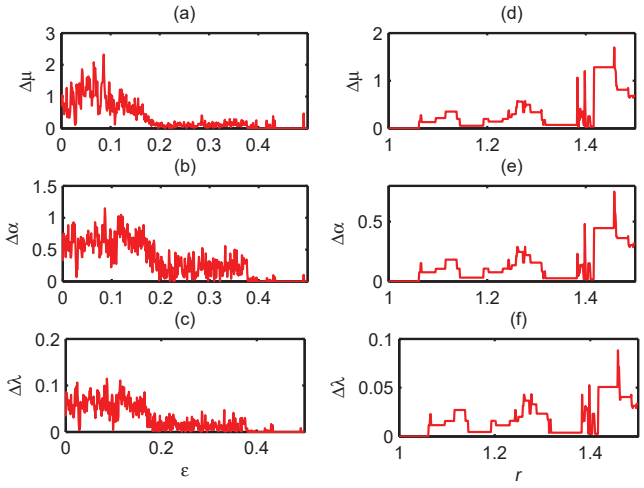

Figure 4.16: Detection of SNA using the sensitivity of OA growth indices on T. (a)-(c) case of $0 \leq \epsilon \leq 0.5$ with $r = 1.5$; and (d)-(f) case of $1 \leq r \leq 1.5$ with $\epsilon = 0$. We considered two observation times: $T_1 = 2 \times 10^4$ and $T_2 = 10^5$, and we set $n = 3$ and $4 \leq \phi \leq 13$.

4.6.3 Detection of the Heagy-Hammel route in the forced logistic map

We have already described the Heagy-Hammel (H-H) route in chapter 2 in the case of the extended PLSE. In this section, we further investigate in the case of the OA growth indices and OAC. In the forced logistic map, a SNA occurs in the H-H route when the period-2^2 torus collides with its unstable parent [41, 54]. This phenomenon is observed for $\epsilon = 0.3$ and the H-H transition appears at $r_0 \simeq 3.487793$ [34, 60]. We thus examined the behavior of the system in the neighborhood of r_0 and compared the result of the OA growth indices and OAC with the Lyapunov exponent. In the other side of the SNA appears the transition between SNA and chaos at $r_1 = 3.512$ [54]. By setting $n = 2$ and $4 \leq \phi \leq 13$, the results obtained are presented in Fig. 4.17 and Fig. 4.18. While interpreting the results in Fig. 4.17, a periodic dynamics is detected for $3.48 \leq r \leq 3.488$. Normally, this dynamics corresponds to a torus, but which is not too complex than in the case of the GOPY map. By increasing n, it is no longer be detected as periodic as shown in Fig. 4.19. We can also observe that the transition SNA-chaos is early detected by λ, whereas λ_{Lyap} still indicates and SNA. In Fig. 4.18, the OAC does no longer significantly depend on ϕ as the time series length is sufficiently large, $T = 10^6$. The OAC spectrum is clearly showing all the transitions tori-SNA and SNA-chaos. However, it still remains difficult to define a threshold indicating the maximum value of OAC that can be affected to SNA or the minimum value of OAC for chaotic dynamics. Therefore, the detection of the transition SNA-chaos can only be assured by the sign of λ. We also observed as in the case of the GOPY map that the matching energy still behaves similarly as the Lyapunov exponent, but in the reverse way. So, definitely it can efficiently help to detect transitions, but not to quantify the complexity of the dynamics, as compared to the Lyapunov exponent. Such a result attests that the ME algorithm performs well for systems which do not exhibit quasi-periodic dynamics.

Now setting $n = 3$, we observed that the detection of the transition SNA-chaos is improved (see Fig. 4.19) and that in the OAC spectrum also a threshold can be defined (see Fig. 4.20) for $\phi \geq 8$. However, the detection of chaotic motions is now delayed and we may require to increase ϕ. Indeed, the diversity of the OA in that case is not well exploited for small values of ϕ, although the time series length is sufficiently large. Nevertheless, it can be observed in Fig. 4.20 that the sensitivity of the OAC to the variation of ϕ significantly increased for $n = 3$ as compared to Fig. 4.18 where $n = 2$. We also observed that the OAC

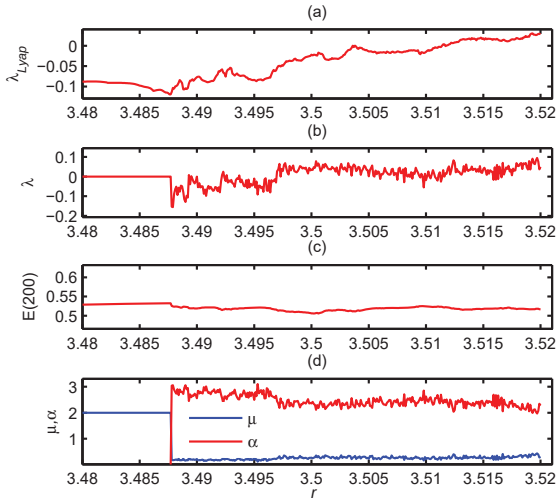

Figure 4.17: Detection of the transition from torus to SNA by the H-H route in the forced logistic map, $\epsilon = 0.3$, $n = 2$, $4 \leq \phi \leq 13$, $T = 10^6$. From top to bottom the Lyapunov exponent, the non-regularity index λ, the matching energy $E(200)$ and the regularity indices μ and α.

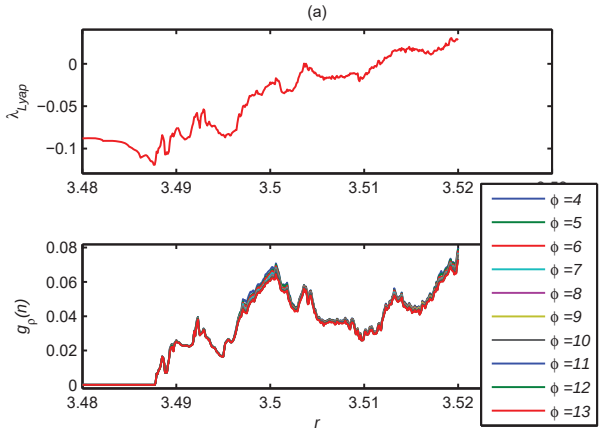

Figure 4.18: Detection of the transition from torus to SNA by the H-H route in the forced logistic map, $\epsilon = 0.3$, $n = 2$, $4 \leq \phi \leq 13$, $T = 10^6$. (a) the Lyapunov exponent spectrum and (b) the OAC spectrum.

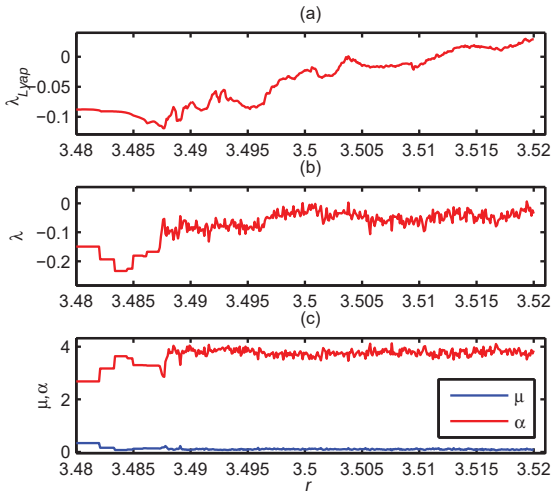

Figure 4.19: Detection of the transition from torus to SNA by the H-H route in the forced logistic map, $\epsilon = 0.3$, $n = 3$, $4 \leq \phi \leq 13$, $T = 10^6$. From top to bottom the Lyapunov exponent, the non-regularity index λ and the regularity indices μ and α.

increases with n. Finally, we can conclude that the detection results are better as n and ϕ are large and $T \gg \Lambda_{max}$. In this example, $T = 10^6$ while $\Lambda_{max} < 10^4$, even for $n = 3$. While dealing with more complex dynamics, increasing n may require too large values of T as $\Lambda_{max} \simeq (n!)^{\phi_{max}}$.

4.6.4 Detection of the Heagy-Hammel route in the forced cubic map

The forced cubic map is known to exhibit a SNA (torus-SNA transition) in the neighborhood of $\beta_0 = 1.88697$ for $A = 0.7$. Initially, it has for $\beta = 1.8865$ a period-2^i torus, $i \in \mathbb{N}$ that begins to wrinkle as β increases to the value 1.8868 until it approaches its unstable parent [34]. After the appearance of SNA, the system moves smoothly toward a chaotic dynamics as β approaches 1.8875. We applied the OA-based algorithm with $n = 3$ and $T = 10^6$. The corresponding results are shown in Fig. 4.21 for the OA growth indices spectra and in Fig. 4.22 for the OAC spectra. The spectra were obtained for β varying from 1.886 to 1.889, by step size $\Delta\beta = 10^{-5}$. According to these figures, the above transitions are well detected in both spectra. Once more, we observed that the behavior of the OAC spectrum approximates that of the Lyapunov exponent as ϕ increases.

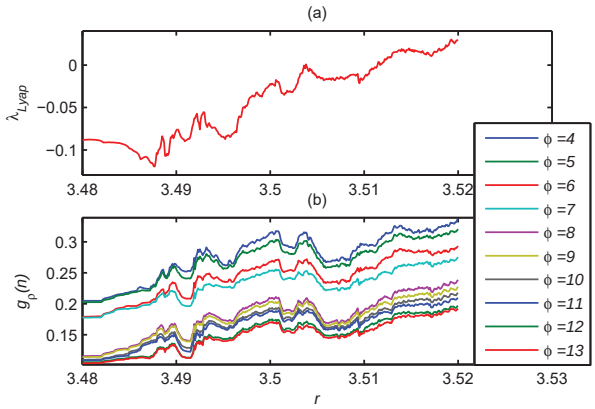

Figure 4.20: Detection of the transition from torus to SNA by the H-H route in the forced logistic map, $\epsilon = 0.3$, $n = 3$, $4 \leq \phi \leq 13$, $T = 10^6$. (a) the Lyapunov exponent spectrum and (b) the OAC spectrum.

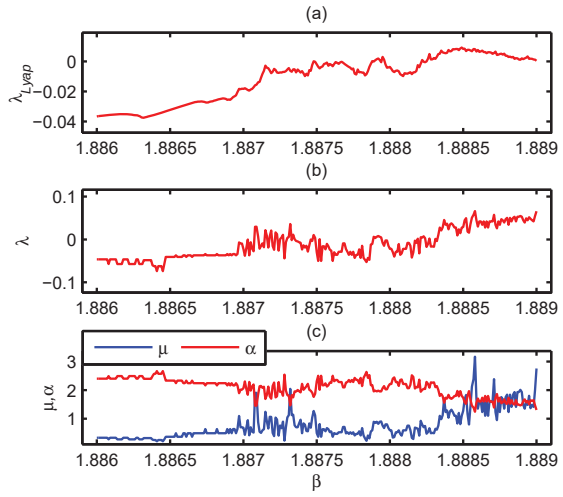

Figure 4.21: Detection of the transition from torus to SNA by the H-H route in the forced cubic map, $A = 0.7$, $n = 4$, $8 \leq \phi \leq 17$, $T = 10^6$. From top to bottom the Lyapunov exponent, the non-regularity index λ and the regularity indices μ and α.

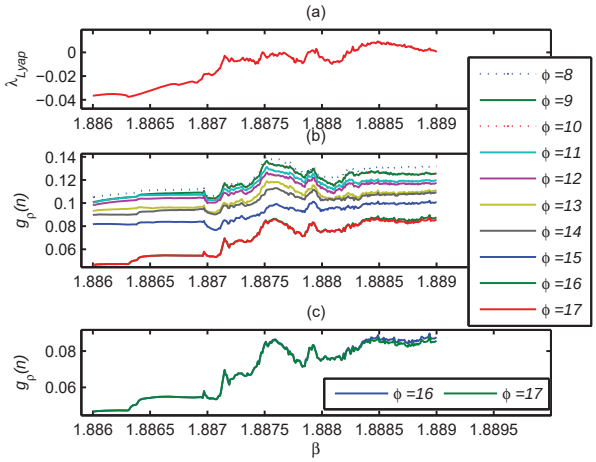

Figure 4.22: Detection of the transition from torus to SNA by the H-H route in the forced cubic map, $A = 0.7$, $n = 4$ and $T = 10^6$. (a) the Lyapunov exponent spectrum and (b) the OAC spectrum for $8 \leq \phi \leq 17$.

4.6.5 Fractalization route in the forced logistic map

The fractalization route to SNA in the logistic map has also been presented in chapter 2. It is obtained for $\epsilon = 1$ and $2.64 \leq r \leq 2.67$. In that case, a period-L torus attractor gets wrinkled and eventually forms an L-band SNA [34, 60]. Fig. 4.23 shows the OA growth indices spectra. The transition from torus to SNA is assumed to appear at $r = 2.6587$ according to this figure, instead of $r_0 = 2.6526$ as predicted in [34]. Nevertheless, Fig. 4.24 gives more details on the different transitions that occur in the system behavior.

4.6.6 Fractalization route in the forced cubic map

The fractalization route to chaos in the cubic map is obtained for $A = 0.1$ and $2.14 \leq \beta \leq 2.17$, with $\Delta\beta = 10^{-4}$. While comparing the OA growth indices and the Lyapunov spectra, it clearly appears that the OA indices efficiently detect transitions occurring in the system behavior, even in the doubled torus region ($\beta = 2.14$ to $\beta = 2.167$) as it is observed in Fig. 4.25. The system is assumed to start with a torus like motion at $\beta = 2.14$, thereafter to exhibit a quasi-periodic oscillation of the double torus for $\beta = 2.16$, then to move to a wrinkled torus for $\beta = 2.165$; the SNA appears for $\beta = 2.167$ and finally, the system becomes chaotic for $\beta = 2.1675$ [34]. All these transitions can be also clearly observed on the OAC spectrum in Fig. 4.26.

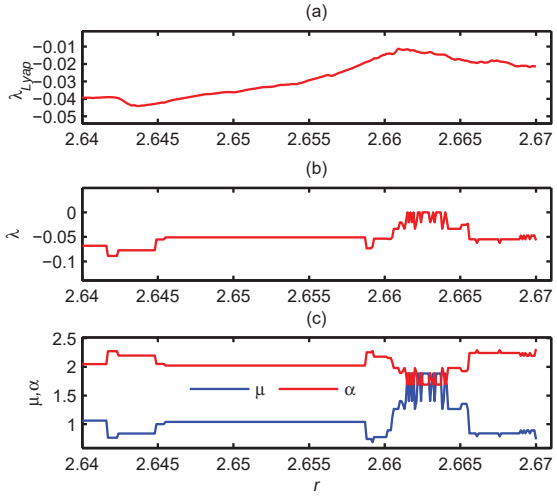

Figure 4.23: Fractalization route to SNA in the forced logistic map, $\epsilon = 1$, $n = 3$, $4 \leq \phi \leq 13$, $T = 10^6$. (a) the Lyapunov exponent spectrum, (b) the non-regularity index λ and (c) the regularity indices μ and α.

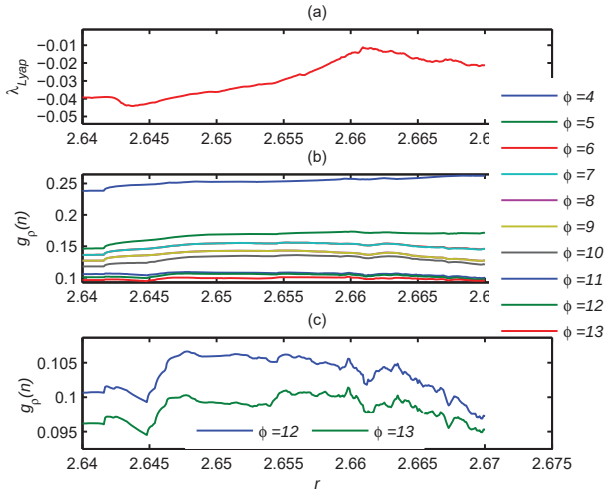

Figure 4.24: Fractalization route to SNA in the forced logistic map, $\epsilon = 1$, $n = 3$ and $T = 10^6$. (a) the Lyapunov exponent spectrum, (b) the OAC spectrum for $4 \leq \phi \leq 13$, and (c) OAC spectrum for $\phi = 12$ and $\phi = 13$.

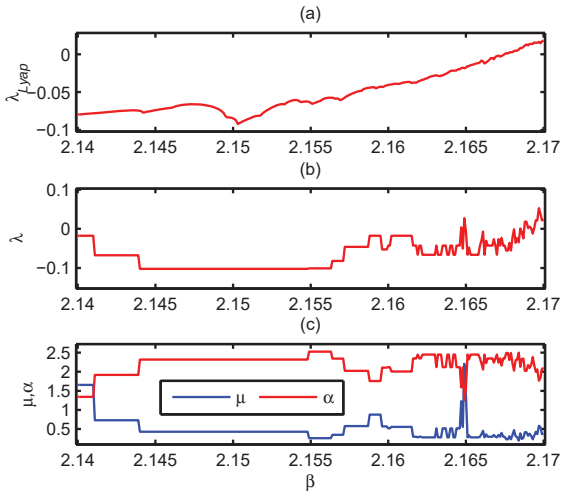

Figure 4.25: Fractalization route to SNA in the forced cubic map, $A = 0.1$, $n = 3$, $8 \leq \phi \leq 17$, $T = 10^6$. (a) the Lyapunov exponent spectrum, (b) the non-regularity index λ and (c) the regularity indices μ and α.

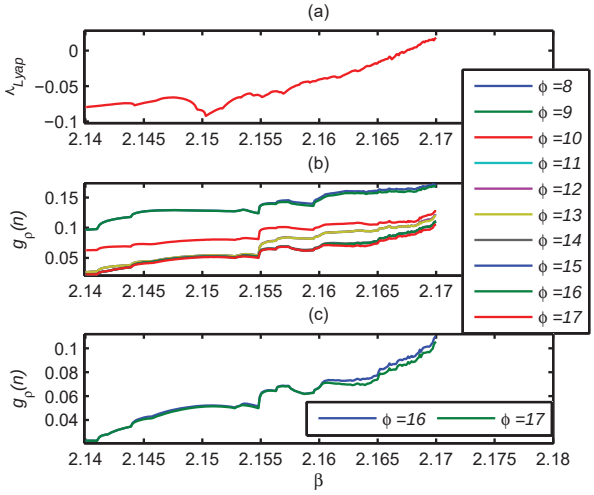

Figure 4.26: Fractalization route to SNA in the forced cubic map, $A = 0.1$, $n = 3$ and $T = 10^6$. (a) the Lyapunov exponent spectrum, (b) the OAC spectra for $8 \leq \phi \leq 17$, and (c) OAC spectrum for $\phi = 16$ and $\phi = 17$.

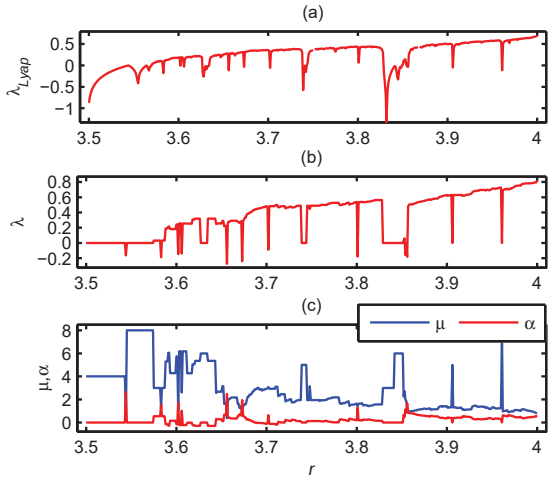

Figure 4.27: Chaos detection in the logistic map: (a) spectrum of the Lyapunov exponent, (b) the non-regularity index λ and (c) the regularity indices μ and α. We set $n = 5$, $0 \leq \phi \leq 9$ and $T = 10^6$

4.7 Classifying data into deterministic or stochastic

We established in section 4.5 the behavior of Λ for a purely random source. As it is well known that such sources are purely stochastic, we may extend the usefulness of the OA asymptotic growth indices and the OAC to the classification of data as deterministic or stochastic. Indeed, regular dynamics are undoubtedly deterministic and are now well characterized by the OA-based algorithms. The main problem rely on non-regular dynamics as it is not easy to determine whether a dynamics is chaotic (deterministic) or stochastic, based on the complexity measure. Theoretically, the complexity of stochastic data should normally be greater than that of deterministic data. However, while using ordinal pattern-based algorithms as well as other common well scaled complexity measures, it arises that the complexity of stochastic and chaotic data are approximately the same, thus making difficult to define a threshold for distinguishing between the two types of data. An example of controversial topic about the classification of the ECG data. Some researchers think that the ECG is chaotic, so could be processed by nonlinear methods [14, 70, 53]; whereas the others think that it is stochastic and should therefore be processed by statistical methods [18]. Nonetheless, classifying data as deterministic or stochastic is important as it help to determine the appropriate method to be used for an efficient data analysis.

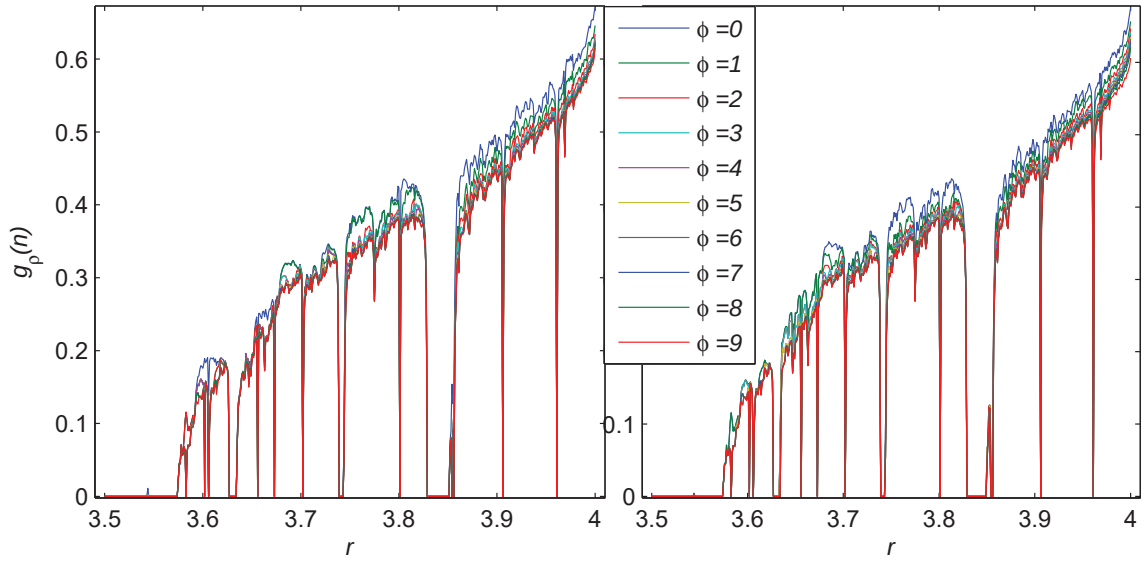

Figure 4.28: OAC spectra of the logistic map for $0 \leq \phi \leq 9$ and $T = 10^6$. The parameter embedding dimension is set as $n = 6$ (left side spectra) and $n = 7$ (right side spectra).

Coming back to the OA-based approach, we established that periodic dynamics are characterized by $\psi_P = (\mu \in \mathbb{N}_{\geq 1}, 0, 0)$ and a zero OAC if the embedding dimension is suitably chosen, while quasi-periodic and SNA are characterized by $\psi_{QP} = (\mu \in \mathbb{R}_+ \setminus \mathbb{N}, \alpha \in \mathbb{R}_+ \setminus \mathbb{N}, \lambda \leq 0)$ and an OAC which asymptotically tends to zero as the embedding dimension ρ increases. Chaotic data are intermediate between regular and purely random data, which are characterized by $\psi_R = \left((n!)^{1-n}, 0, \frac{\ln(n!)}{\ln(b)}\right)$. It is also well known that in a purely random source, all the symbols are equiprobable. Taking into account this property in the definition of the OAC in Eq. (4.3.1), it comes that the OAC of such sources is equal to $\ln(n)$, which is the upper limit of $g_\rho(n)$ in the assumption that the number of distinct symbols is upper bounded by $\Lambda_0 = (n!)^{\phi+1}$. Based on the definition of the purely random source (stochastic) and the regular dynamics (deterministic), one can establish that a non-regular dynamics is stochastic as $\mu \to (n!)^{1-n}$, $|\alpha| \to 0$, $\lambda \to \frac{\ln(n!)}{\ln(b)}$ and $g_\rho(n) \to \ln(n!)$. For the other values smaller than these established limits, the dynamics can be said chaotic, hence deterministic. Indeed, we observed that $\mu \leq (n!)^{1-n}$ for stochastic data and $\mu > (n!)^{1-n}$ for chaotic data. An example of chaos detection is given in Fig. 4.27 and Fig. 4.28 in the case of the logistic map. It can be observed on these figures that the combination of the OAC and the OA

growth indices allows to efficiently characterize all the dynamics of the logistic map.

4.8 Conclusion

In this chapter, we established the applicability of OA-based algorithms to the classification of regular dynamics into periodic, quasi-periodic and SNA; as well as the classification of non-regular dynamics into chaotic and stochastic. We applied the OA growth indices to quasi-periodically forced maps and verified that periodic dynamics are characterized by a positive integer value of the periodicity index and zero values of quasi-periodicity and non-regularity indices; SNA and quasi-periodic dynamics are characterized by a non-integer value of the periodicity index, a positive quasi-periodicity index and a negative non-regularity index. All these regular dynamics are characterized by a small value of OAC, which decreases as the angular embedding dimension ϕ increases. Non-regular dynamics are characterized by a positive non-regularity index. A time series is stochastic as its periodicity index is smaller than $\mu_0 = (n!)^{1-n}$, its quasi-periodicity index tends to zero, its non-regularity index tends to $\lambda_0 = \frac{\ln(n!)}{\ln(b)}$ and its OAC tends to $\ln(n)$. Chaotic data belong to other intermediate combinations of the OA growth indices between regular and stochastic data. They are particularly characterized by $\mu > (n!)^{1-n}$. In addition to the detection of the structural changes occurring in the dynamics of the underlying system well performed by the Lyapunov exponent, the ME, the PE and the CPE, the OA growth indices give the possibility to determine the nature of a single time series. These properties thus established may be helpful in many research domains wherever the real-time classification of large amount of data is required, taking into account the high speed performance of the OA-based algorithms and their applicability to any type of time series.

Conclusion

This work has presented ordinal pattern-based algorithms for complexity measure, as well as their improvement for the detection of SNA and quasi-periodic dynamics. The main objective was to investigate the application of this type of algorithms to quasi-periodically forced systems, as this appears not to have been studied.

Thus, we first presented the 3ST algorithm whose objective was to discern between periodic, quasi-periodic and chaotic dynamics. We showed that although the test can detect periodic and chaotic dynamics, its fails to distinguish between quasi-periodic and periodic dynamics with large periods, or between weakly chaotic and quasi-periodic dynamics. Furthermore, the algorithm itself was not easy to implement, although the mathematical foundation was clearly established. We then upgrade the 3ST algorithm by using the entropy approach in the PLSE algorithm.

The PLSE was defined as an entropy measure related to the permutation largest slopes. We showed that both the PLSE and the sensitivity to the initial phase defined in the 3ST algorithms output a zero value for periodic and quasi-periodic dynamics. However, like the 3ST algorithm, the PLSE was not able to clearly distinguish between periodic and quasi-periodic dynamics, despite its good performance for chaos detection. Then, we proposed an extension of the PLSE for the detection of SNA and quasi-periodic dynamics. The results obtained were quite satisfactory, but we could not clearly determine the difference between SNA and weakly chaotic dynamics as the right parameter setting was not easy to determine. Furthermore, PLSE algorithm was not able to scale chaos as it was initially developed for detection purposes. By comparing the PLSE to the permutation entropy (PE), we showed that PLSE is suitable for chaos detection, while PE is suitable for complexity measure.

Detection algorithms allow us to determine the nature of a given time series while

complexity measures allow us to quantify its complexity. In order to define a complexity measure, we introduced the ME, a recently developed algorithm for complexity measure in real-world data. It has the ability to detect regular dynamics and to measure chaos even in a noisy environment, but unfortunately it did not succeed in the case of quasi-periodic dynamics. Both detection and complexity measure aspects were already combined in the CPE, which has been shown to be an improvement of the PE algorithm. However, this approach also failed to detect quasi-periodic and periodic dynamics with large periods. In order to address this concern, we proposed in chapter 4 to consider ordinal arrays instead of the permutations (ordinal patterns). This new approach gave us the possibility of defining the OAC as a generalized approximation of the ordinal KS entropy, thus including the CPE algorithm; and defining OA asymptotic growth indices allowing us to discern among the different types of regular and non-regular dynamics. By combining the OAC and the OA growth indices, we achieved the classification of regular dynamics into periodic, quasi-periodic and SNA, which was not possible by the previous ordinal pattern algorithms. Moreover, we showed that the above combination of the OAC and OA growth indices also allows to classify non-regular dynamics into chaotic and stochastic, thus giving us the possibility to classify time series into deterministic or stochastic. We showed that both the OAC and the non-regularity index easily allow to measure chaos as they present an upper limit which clearly depends on the embedding dimension. The above properties thus established for the OA-based indicators may be helpful in many research domains wherever the real-time classification of large amount of data is required, taking into account the high speed performance and the robustness against noise of the OA-based algorithms and their applicability to any type of time series. By further investigating the parameter setting, the properties and the frontiers between the different types of data series, OA-based algorithms may constitute a complete tool for the real-time analysis of real-world data.

Bibliography

[1] H. D. I. Abarbanel, *Analysis of observed chaotic data*, Springer, New York, 1996.

[2] O. Afsar, G. B. Bagei, and U. Tirnakli, *Renormalized entropy for one dimensional discrete map: Periodic and quasi-periodic route to chaos and their robustness*, Eur. Phys. J. B **86** (2013), 307–320.

[3] J. M. Amigó, *Permutation complexity in dynamical systems*, Springer, 2010.

[4] C. Bandt and B. Pompe, *Permutation entropy: A natural complexity measure for time series*, Physical review letters **88** (2002), 174102.

[5] W.A. Barnett and A. Serletis, *Martingales, nonlinearity and chaos, journal of economic*, Dynamics and Control **24** (2000), 703–724.

[6] C. Bian, C. Qin, Q. D. Y. Ma, and Q. Shen, *Modified permutation-entropy analysis of heartbeat dynamics*, Phys. Rev. E **85** (2012), 021906.

[7] E. Bradley and H. Kantz, *Nonlinear time-series revisited*, Chaos **25** (2015), 097610.

[8] A. A. Brudno, *Entropy and complexity of the trajectories of a dynamical system*, Trans. Moscow Math. Soc. **2** (1983), 127–151.

[9] A. Bruzzo, B. Gesierich, M. Santi, C. Tassinari, N. Bir-baumer, and G. Rubboli, *Permutation entropy to detect vigilance changes and preictal states from scalp eeg in epileptic patients: a preliminary study*, Neurol. Sci. **29** (2008), 3–9.

[10] Y. Cao, W. Tung, J. Gao, V. Protopopescu, and L. Hively, *Detecting dynamical changes in time series using the permutation entropy*, Phys. Rev. E **70** (2004), 046217.

[11] F. Cecconi, M. Cencini, M. Falcioni, and A. Vulpiani, *Brownian motion and diffusion: from stochastic processes to deterministic chaos*, CHAOS **15** (2005), 026102.

[12] S. Chaudhury, A. Smith, B.E. Anderson, S. Ghose, and P.S. Jessen, *Deterministic nonperiodic flow*, J. Atmos. Sci. **20** (1963), 130141.

[13] ———, *Quantum signatures of chaos in a kicked top*, Nature **461** (2009), 768–771.

[14] M. Chena, Y. Fanga, and X. Zhengc, *Phase space reconstruction for improving theclassification of single trial eeg*, Biomed. Signal Process. Control **11** (2014), 10–16.

[15] G.H. Choe, *Computational ergodic theory*, Springer, Berlin, 2005.

[16] P. T. Clemson and A. Stefanovska, *Discerning non-autonomous dynamics*, Physics Reports **20** (2014), 297–368.

[17] P. Collet and J.-P. Eckmann, *Iterated maps on the interval as dynamical systems*, Birkhaeuser, Basel, 1980.

[18] E. David and M.D. Albert, *Chaos and the ecg: Fact and fiction*, Journal of Electrocardiology **24** (1991), 102–106.

[19] M. Ding, C. Grebogi, E. Ott, T. Sauer, and J. A. Yorke, *Estimating correlation dimension from a chaotic time series: when does it ocur?*, Phys. Rev. Lett. **70** (1993), 3872.

[20] J.-P. Eckmann and D. Ruelle, *Ergodic theory of chaos*, Rev. Mod. Phys. **57** (1985), 617.

[21] B. Fadlallah, J. Príncipe, B. Chen, and A. Keil, *Weighted-permutation entropy: An improved complexity measure for time series*, Phys. Rev. E **87** (2013), 022911.

[22] J. S. A. Eyebe Fouda, *The matching energy: a novel approach for measuring complexity in time series*, Nonlinear Dyn. (2016), DOI: 10.1007/s11071–016–3014–8.

[23] _____, *Applicability of the permutation largest slope to strange nonchaotic attractors*, Nonlinear Dyn. (Submitted).

[24] J. S. A. Eyebe Fouda, B. Bodo, G. M. D. Djeufa, and S. L. Sabat, *Experimental chaos detection in the duffing oscillator*, Commun Nonlinear Sci. Numer. Simulat. **33** (2016), 259–269.

[25] J. S. A. Eyebe Fouda, B. Bodo, S. L. Sabat, and J. Y. Effa, *A modified 0-1 test for chaos detection in oversampled time series observations*, IJBC **24** (2014), 1450063.

[26] J. S. A. Eyebe Fouda, J. Y. Effa, M. Kom, and M. Ali, *The three-state test for chaos detection in discrete maps*, Applied Soft Computing **13** (2013), 4731–4737.

[27] J. S. A. Eyebe Fouda and W. Koepf, *Efficient detection of the quasi-periodic route to chaos by the three-state test*, Nonlinear Dyn. **78** (2014), 1477–1487.

[28] _____, *Detecting regular dynamics from time series using permutations slopes*, Commun. Nonlinear Sci. Numer. Simulat. **27** (2015), 216–227.

[29] J. S. A. Eyebe Fouda and S. L. Sabat, *A multiplierless hyperchaotic system using coupled duffing oscillators*, Commun Nonlinear Sci. Numer. Simulat. **20** (2015), 24–31.

[30] S. Galatolo, *Orbit complexity and data compression*, Discr. Cont. Dyn. Systems **7** (2001), 477–486.

[31] J. B. Gao, J. Hu, W. W. Tung, and Y. H. Cao, *Distinguishing chaos from noise by scale-dependent lyapunov exponent*, Phys. Rev. E. **74** (2006), 066204.

[32] L. Glas, *Introduction to controversial topics in nonlinear science: Is the normal heart rate chaotic?*, Chaos **19** (2009), 0285014.

[33] P.A. Glendinning, *Non-smooth pitchfork bifurcations*, Discrete Contin. Dyn. Syst. Ser. B **4** (2004), 457–464.

[34] R. Gopal, A. Venkatesan, and M. Lakshmanan, *Applicability of 0-1 test for strange nonchaotic attractors.*, Chaos **23** (2013), 023123.

[35] G. A. Gottwald and I. Melbourne, *A new test for chaos in deterministic systems*, Proc. Roy. Soc. London. Ser. **A 460** (2004), 603–611.

[36] _____, *On the implementation of the 0-1 test for chaos*, SIAM J. Appl. Dyn. Syst. **8** (2009), 129–145.

[37] _____, *On the validity of the 0-1 test for chaos*, Nonlinearity **22** (2009), 1367.

[38] P. Grassberger and I. Procaccia, *Estimation of the kolmogorov entropy from a chaotic signal*, Phys. Rev. A **28** (1983), 2591–2593.

[39] C. Grebogi, E. Ott, S. Pelikan, and J. A. Yorke, *Strange attractors that are not chaotic*, Physica D **13** (1984), 261–268.

[40] B.-L Hao, *Symbolic dynamics and characterization of complexity*, Physica D **51** (1991), 161–176.

[41] J. F. Heagy and H. Hammel, *The birth of strange nonchaotic attractors*, Physica D **70** (1994), 140–153.

[42] R. Houben, N. de Groot, and M. Allessie, *Analysis of fractionated atrial fibrillationelectrograms by wavelet decomposition*, IEEE Trans. Biomed. Eng. **57** (2010), 13881398.

[43] J. Hu, J. B. Gao, and W. W. Tung, *The analysis of observed chaotic data in physical systems*, Chaos **19** (2009), 028506.

[44] H. Kantz and T. Schreiber, *Nonlinear time series analysis*, Cambridge University Press, 2004.

[45] X. Li, S. Cui, and L. Voss, *Using permutation entropy to measure the electroencephalographic effects of sevoflurane*, Anesthesiology **109** (2008), 448–456.

[46] X. Li, G. Ouyang, and D. Richards, *Predictability analysis of absence seizures with permutation entropy*, Epilepsy Res. **77** (2007), 70–74.

[47] Y. Li, B. J. Yang, J. Badal, X. P. Zhao, H. B. Lin, and R. L. Li, *Chaotic system detection of weak seismic signals*, Geophys. J. Int. **178** (2009), 1493–1522.

[48] Z. Li, G. Ouyang, D. Li, and X. Li, *Characterization of the causality between spike trains with permutation conditional mutual information*, Phys. Rev. E **84** (2011), 021929.

[49] J. F. Lindner, V. Kohar, B. Kia, M. Hippke, J. G. Learned, and W. L. Ditto, *Strange nonchaotic stars*, Physical Review Letters **114** (2015), 054101.

[50] G. Litak and M. Borowiec, *On simulation of a bistable system with fractional damping in the presence of stochastic coherence resonance*, Nonlinear Dyn. **77** (2014), 681–686.

[51] M. Martens and T. Nowicki, *Invariant measures for typical quadratic maps*, Astérisque, Paris, 2000.

[52] S. Narayan, M. Wright, N. Derval, A. Jadidi, A. Forclaz, I. Nault, S. Miyazaki, F.Sacher, P. Bordachar, J. Clmenty, and et al., *Classifying fractionated electrograms in human atrial fibrillation using monophasic action potentials and activation mapping: evidence for localized drivers, rate acceleration, and nonlocal signaletiologies*, Heart Rhythm **8** (2011), 244–253.

[53] I. Neacsu, D. E. Creanga, and Fl. M. Tufescu, *Complexity analysis of electrocardiographic signals*, Gen. Physiol. Biophys. **25** (2006), 161–176.

[54] S. S. Negi, A. Prasad, and R. Ramaswamy, *Bifurcations and transitions in the quasiperiodically driven logistic map*, Physica D **145** (2000), 1–12.

[55] Ya. B. Pesin, *Dimension theory in dynamical systems*, Ph.D. thesis, University of Chicago Press, Chicago, 1998.

[56] A.S. Pikovsky and U. Feudel, *Characterizing strange nonchaotic attractors*, Chaos **5** (1995), 253–260.

[57] S. M. Pincus, *The analysis of observed chaotic data in physical systems*, Proc. Natl. Acad. Sci. **88** (1991), 2297.

[58] _____, *Approximate entropy as a measure of system complexity*, Proc. Natl. Acad. Sci. **88** (1991), 2297–2301.

[59] S. M. Pincus and A. L. Goldberger, *Physiological time series analysis -what does regularity quantify*, Am. J. Physiol. Heart Circ. Physiol. **266** (1994), 1643–1656.

[60] A. Prassad, V. Mehra, and R. Ramaswamy, *Intermittency route to strange nonchaotic attractors*, Physical Review Letter **79** (1997), 4127–4130.

[61] O. Regev, *Chaos and complexity in astrophysics*, Cambridge University Press, New York, 2006.

[62] J.S. Richman and J.R. Moorman, *Physiological time-series analysis using approximate entropy and sample entropy*, Am. J. Physiol-Heart C. **278** (2000), H2039–H2049.

[63] Michael T. Rosenstein, James J. Collins, and Carlo J. De Luca, *A practical method for calculating largest* L*yapunov exponents from small data sets*, Physica D **65** (1993), 117–134.

[64] O. A. Rosso, H. A. Larrondo, M. T. Martin, A. Plastino, and M. A. Fuentes, *Distinguishing noise from chaos*, Phys. Rev. Lett. **99** (2007), 154102.

[65] J.C. Sprott, *Chaos and time-series analysis*, Oxford University Press, Oxford, 2003.

[66] Nicholas Tufillaro, *Symbolic dynamics in mathematics, physics, and engineering*, Tech. report, Integrated Solutions Laboratory, HP Laboratories Palo Alto, 1999.

[67] V. A. Unakafov and K. Keller, *Conditional entropy of ordinal patterns*, Physica D **269** (2014), 94–102.

[68] V. A. Unakafova and K. Keller, *Efficiently measuring complexity on the basis of real-world data*, Entropy **15** (2013), 4392–4415.

[69] M. Wood, P. Moskovljevic, B. Stambler, and K. Ellenbogen, *Comparison of bipo-lar atrial electrogram amplitude in sinus rhythm, atrial fibrillation, and atrialflutter*, Pacing Clin. Electrophysiol. **19** (1996), 150–156.

[70] B. Xu, S. Jacquir, G. Laurant, J.-M. Bilbault, and S. Binczak, *Analysis of an experimental model of in vitro cardiac tissue using phase space reconstruction*, Biomed. Signal Process. Control **13** (2014), 313–326.

[71] L.-S. Young, *Entropy in dynamical systems*, Princeton University Press, Princeton, 2003.